

CENTRO BRASILEIRO DE PESQUISAS EM FÍSICA

DEPARTAMENTO DE FÍSICA

**FORMATION OF SPIN-POLARIZED
MAJORANA FERMIONS IN NANORIBBONS**

RENAN BENTO RIBEIRO CAMPOS

ORIENTADOR: PROF. DR. MUCIO AMADO CONTINENTINO
CO-ORIENTADOR: PROF. DR. MARCOS SEGIO FIGUEIRA DA SILVA

Niterói

23 de março de 2024

CENTRO BRASILEIRO DE PESQUISAS EM FÍSICA

DEPARTAMENTO DE FÍSICA

**FORMATION OF SPIN-POLARIZED
MAJORANA FERMIONS IN NANORIBBONS**

RENAN BENTO RIBEIRO CAMPOS

Dissertação apresentada ao Programa de Pós
Graduação do Centro Brasileiro de Pesquisas em
Física, como parte dos requisitos para a obtenção do
título de Mestre em Ciências

Orientador: Prof. Dr. Mucio Amado Continentino

Niterói

23 de março de 2024


"FORMATION OF SPIN-POLARIZED MAJORANA FERMIONS IN
NANORIBBONS"

RENAN BENTO RIBEIRO CAMPOS


Tese de Doutorado em Física apresentada no
Centro Brasileiro de Pesquisas Físicas do
Ministério da Ciência Tecnologia e Inovação.
Fazendo parte da banca examinadora os seguintes
professores:



Mucio Amado Continentino - Orientador/CBPF

Documento assinado digitalmente
 **MARCOS SERGIO FIGUEIRA DA SILVA**
Data: 01/03/2024 15:12:37-0300
Verifique em <https://validar.iti.gov.br>

Marcos Sergio Figueira da Silva - Coorientador/CBPF

Documento assinado digitalmente
 **GEORGE BALSTER MARTINS**
Data: 04/03/2024 14:42:31-0300
Verifique em <https://validar.iti.gov.br>

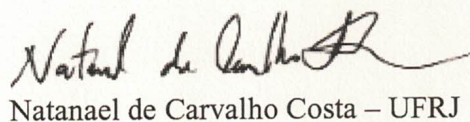
George Balster Martins – UFU



Edson Vernek – UFU



Yutao Xing – UFF



Natanael de Carvalho Costa – UFRJ

Rio de Janeiro, 20 de dezembro de 2023.

Este trabalho é dedicado à minha avó Ligya(in memorian) e meu pai Arthemio (in memorian).

AGRADECIMENTOS

A minha noiva Marcela e aos meus amigos do metrasdo, Luiz e Hugo por terem me dado a força e o companheirismo nos momentos mais difíceis. A minha família e a família da Marcela a por ter me dado todo o suporte e amor durante minha vida. Principalmente à minha mãe e meus avós pela minha criação.

A todos os meus amigos que me proporcionaram diversão e amizade durante vários momentos da minha vida, em especial ao Matheus e Eduardo que são meus amigos desde a infância

Aos meus professores Mucio Amado Continentino e Marcos Sergio Figueira da Silva, pela orientação durante o doutorado, por nunca desistir de mim, sempre me apoiar quando eu mesmo não tinha mais forças para continuar e é claro pela confecção deste trabalho. Também gostaria de agradecer ao Dr. Jorge Huamani pelas proveitosas discussões durante o desenvolvimento do código numérico.

A todos os outros professores do CBPF e de outras instituições principalmente à CAPES, CNPq e FAPERJ pelo apoio deste trabalho., pela minha formação acadêmica.

"There is a theory which states that if ever anyone discovers exactly what the Universe is for and why it is here, it will instantly disappear and be replaced by something even more bizarre and inexplicable. There is another theory which states that this has already happened

Douglas Adams

RESUMO

Esta tese tem como principal objetivo estudar modelos de materiais quase-bidimensionais do tipo nanofitas que são infinitas (ou de comprimento muito grande na direção x e são pequenas na direção y), particularmente feitas de carbono e silício, do ponto de vista teórico. O foco principal está na aplicação de conceitos topológicos a esses materiais, levando à investigação de suas propriedades eletrônicas e ao surgimento de modos zero de Majorana (MZMs) em diversos sistemas.

Os capítulos iniciais da tese apresentam o modelo Su-Schrieffer-Heeger (SSH), uma estrutura fundamental para a compreensão de materiais topológicos. O modelo SSH é usado para analisar estruturas de bandas eletrônicas, espectros de energia de sistemas finitos e funções de onda, esclarecendo sua natureza topológica. Generalizações do modelo SSH, como o modelo Rice-Mele, são exploradas, levando à compreensão sobre seu comportamento e a presença de estados localizados de energia zero.

A tese também aborda o impacto de campos magnéticos externos (efeito Zeeman) sobre estes modelos, levantando a degenerescência do spin e influenciando os níveis de energia. A análise leva em conta aspectos topológicos e eletrônicos, revelando seus efeitos nas estruturas eletrônicas.

Uma parte significativa da tese é dedicada à cadeia Kitaev, que desempenha um papel central. As propriedades de acoplamento supercondutor da cadeia Kitaev são examinadas e os férmions de Majorana tornam-se um ponto focal de investigação. Esforços experimentais relacionados aos férmions de Majorana são discutidos, destacando sua presença em diversos sistemas que serão tratados nos capítulos 3 e 4 da tese onde vamos usar a cadeia de Kitaev como fundamento para a elaboração de um modelo para nanofitas.

Os ingredientes apresentados levam ao desenvolvimento de um modelo para nanofitas hexagonais e pentagonais com bordas spin polarizadas, que podem potencialmente hospedar férmions de Majorana. O modelo considera parâmetros como hopping do vizinho mais próximo, interação spin-órbita de Rashba, acoplamento de supercondutores do tipo tripleto e um campo de efeito Zeeman externo. Várias transições de fase topológicas são observadas, ligadas a férmions de Majorana polarizados por spin, demonstrando a conexão entre transições topológicas e a presença de férmions de Majorana que é apresentado no terceiro capítulo.

Além disso, o estudo enfatiza o potencial dos MZMs para distinguir estados de spin em nanofitas em forma de honeycomb em zigue-zague, oferecendo novas perspectivas para a

identificação de MZMs polarizados por spin em vários materiais. Nanofitas baseadas em siliceno em supercondutores com acoplamento spin-órbita Rashba e campos magnéticos externos são exploradas por seu potencial em computação quântica.

Em resumo, esta tese apresenta uma exploração abrangente de materiais quase-bidimensionais, propriedades topológicas e o surgimento de férmions de Majorana. fornecendo uma base sobre as possibilidades interessantes desses materiais na computação quântica.

Palavras-chave: nanofita, ligações fortes, Majorana férmions, transições de fase topológicas

ABSTRACT

This thesis has as its main objective models of quasi-two-dimensional nanoribbon-type materials that are infinite (or very long in the x direction and small in the y direction), particularly made of carbon and silicon, from a theoretical point of view. The main focus is on the application of topological concepts to these materials, leading to the investigation of their electronic properties and the emergence of zero Majorana modes (MZMs) in several systems.

The initial chapters of the thesis present the Su-Schrieffer-Heeger (SSH) model, a fundamental framework for understanding topological materials. The SSH model is used to analyze electronic band structures, energy spectra of finite systems and wave functions, clarifying their topological nature. Generalizations of the SSH model, such as the Rice-Mele model, are explored, leading to understanding of its behavior and the presence of localized zero-energy states.

The thesis also addresses the effect of external magnetic fields (Zeeman effect) on these models, increasing spin degeneracy and influencing energy levels. The analysis takes into account topological and electronic aspects, revealing their effects on electronic structures. A significant part of the thesis is devoted to the Kitaev chain, which plays a central role. The superconducting coupling properties of the Kitaev chain are examined and Majorana fermions become a focal point of investigation. Experimental efforts related to Majorana fermions are discussed, highlighting their presence in several systems that will be discussed in chapters 3 and 4 of the thesis where we will use the Kitaev chain as a basis for developing a model for nanoribbons.

Bringing together all the presented ingredients leads to the development of a model for graphene nanoribbons with ferromagnetic edges, which can potentially host Majorana fermions. The model considers parameters such as nearest-neighbor hopping, Rashba spin-orbit interaction, triple superconductor coupling, and an external Zeeman effect field. Several topological phase transitions are observed, linked to spin-polarized Majorana fermions, demonstrating the connection between topological transitions and the presence of Majorana fermions that is presented in the third chapter.

Furthermore, the study emphasizes the potential of MZMs to distinguish spin states in zigzag honeycomb and pentagonal nanoribbons, offering new perspectives for identifying spin-polarized MZMs in various materials. Silicene-based superconductor nanoribbons with Rashba spin-orbit coupling and external magnetic fields are explored for their potential in

quantum computing.

In summary, this thesis presents a comprehensive exploration of quasi two-dimensional materials, topological properties, and the emergence of Majorana fermions. providing a background on the interesting possibilities of these materials in quantum computing.

Keywords: nanoribbons, tight binding, Majorana fermions, topological phase transitions

LIST OF FIGURES

2.1	Scheme showing the model of the SSH chain with a chain with the same atom (in blue) with alternating bonds V_1 and V_2	23
2.3	Energy Dispersion in Finite SSH Chain: This figure presents the energy dispersion plot for a finite SSH chain with V_2 varying, picture the band gap in the energy spectrum and its relationship with the bulk transition with V_2 varying. . .	26
2.4	Zero-Energy States in Finite SSH Chain: This figure displays energy eigenvalues as a function of n for a finite SSH chain, emphasizing the existence of zero-energy states and their implications.	27
2.5	Squared wave function or probability per site in SSH Chain: This figure show-cases wave functions within a finite SSH chain, particularly focusing on zero-energy states and electron localization at the chain edge.	28
2.6	Scheme showing the Rice-Mele chain model with a chain with two different atoms (in blue and red) with alternating bonds V_1 and V_2	29
2.7	SSH Band Structure where $V_2 = 1t$	30
2.8	Rice Mele Band Structure ($\epsilon = 0.1$) and $V_2 = 1t$	31
2.9	Band structure of the Eq.2.10. Here we can see that the band structure is shifted by ϵ value downwards the red line is the fermi energy $E(k)=0$ when $\epsilon \neq 0$	32
2.10	Visual depiction of the band structure as dictated by the Hamiltonian in Eq.2.10. Highlights the unique position of the Fermi level when $\epsilon = \mu \neq 0$	32
2.11	The energy dispersion described by the Hamiltonian in Eq.2.4, with parameters as shown in the graph. Notably, the presence of Zero Modes is evident, and a transition from a trivial to a topological phase becomes apparent at $V_2 = 1t$.”. . .	34

2.12	Energy spectrum of the Hamiltonian in Eq.2.4, with the parameter $\varepsilon = 0.1$. It is clear that when $\varepsilon \neq 0$, the zero modes disappear and now there is a gap separating the energies.	35
2.13	the Energy spectrum corresponds to the Hamiltonian described in Eq.2.4 and complies with the specified parameters $\varepsilon = 0.1$ and $\mu = 0.1$, the structure that previously featured a gap now reverts to zero modes, primarily due to the chemical potential aligning with the local energy level.	36
2.14	This figure presents the energy dispersion in line with the Hamiltonian from Eq.2.4 and the defined parameters. Observations reveal that with $\varepsilon = 0.1$ and $\mu = -0.1$, the structure that previously exhibited a gap now displays zero modes once again, a phenomenon resulting from the chemical potential being the negative counterpart of the local energy level.	37
2.15	(a) SSH dispersion energy. (b) Energy per site in the SSH case for $V_1 = 0.5$. (c) Wave function of SSH zero modes for $V_1 = 0.5$. d) Rice-Mele dispersion energy for $\varepsilon = 0.1$. (e) Energy per site in the Rice-Mele case $\varepsilon = 0.1$ and $V_1 = 0.5$. (f) Wave function of the Rice-mele shifted modes for $\varepsilon = 0.1$ and $\varepsilon = -0.1$ for $V_1 = 0.5$	38
2.16	Fig of the Energy bond spectra about the influence of the external magnetic field on the SSH model where $\lambda_z = 0.0, 0.05t, 0.1t, 0.15t$. the color bar is the spin orientation where spin up is 1 and spin down is -1	
2.17	Representation of the SSH chain behaviors influenced by parameters V_1 , μ , and $\lambda_z=0.1$. The Figures a), b), c), d) and e) show the bulk plots for the infinite case, the plots f) is the energy spectra for specific values of V_2 and $V_1 = 1t$ and the plots g), h) is finite energy spectra influenced by chemical potentials with values 0.1t and -0.1 respectively, and the plots i), j), k), l), m) are the plots where we have specific values of V_2 shown in highlights in the graph above in gray and the plots n), o), p), q) and r) are the wave functions for the finite system of the cases above.	

- 2.18 Comparative energy spectra for the Rice-Mele model with varying parameters and applied magnetic field. Fig a) represents the pure SSH case, where ε and λ_z parameters are nullified. Fig b) depicts the RM model behavior with an introduced ε . Fig c) displays the response to a magnetic field λ_z in the system, emphasizing the broken degeneracy. Fig d) gives an overview of specific parameter combinations, highlighting the effects of symmetry breaking and energy accessibility for different spin orientations. In the color bar we have values that can vary from 1 to -1 where 1 would be spin up and -1 spin down.
- 2.19 Energy dispersions and wave functions of the spin-polarized Rice-Mele model under various parameters. Figs a) to d) depict the energy dispersions for an infinite (bulk) system, with a focus on permitted energies in the wave vector space k . Figs e) to j) illustrate the energy spectrum for finite systems with varied V_1 values. Figs k) to n) showcase the localized wave functions corresponding to zero-energy modes or other selected modes based on the energy spectra above.
- 2.20 Finite Kitaev chain for $N = 30$
- 2.21 Representation of the Kitaev chain.
- 2.22 No unpaired Majoranas.
- 2.23 Unpaired Majoranas states.
- 3.1 (a) Sketch of the 2D zHNR geometry adopted here, where N represents its width ($n = 1, \dots, N$). The region within the red dashed area composed of $2N$ nonequivalent A (blue) and B (orange) sites along the y direction represents the unit cell employed in the numerical simulations. The M number of unit cells defines the nanoribbon length ($m = 1, \dots, M$). (b) Representation of the nearest-neighbor hopping t , which is adopted as the energy unit. (c) Schematic of a double-spin KzHNR of width $N = 2$. The equivalent B (A) atoms of the upper (lower) KzHNR are paired with each other via a p -wave superconducting parameter Δ .

- 3.2 Figs (a)-(d): band structure for a $N = 2$ infinity double-spinless KzHNR, considering μ values where the TPTs occur. Figs (e)-(k): the same as top Figs, but considering both spin components (infinite double-spin KzHNR) 3.4. The energies are measured in units of t , and we fix the p -wave superconducting pairing parameter $\Delta = 0.5t$. Additionally, the parameters of the double-spin case (middle and bottom Figs) are $\lambda_R = 0.05t$ and $\lambda_Z = 0.1t$. In the double-spinless case we have four TPTs occurring at: a) $\mu = -1.28t$ b) $\mu = -0.78t$ c) $\mu = -0.50t$ d) $\mu = 0$. For the double-spin case, the TPTs occur at e) $\mu = -1.33t$ with spin down, f) $\mu = -1.23t$ with spin up g) $\mu = -0.84t$ with spin down, h) $\mu = -0.73t$ with spin up, i) $\mu = -0.55t$ with spin down j) $\mu = -0.45t$ with spin up k) $\mu = -0.05t$ with spin down. The density of states, corresponding to the band structure depicted in (k), is plotted in (l), where we can observe the half-metallicity characteristic of those TPTs.
- 3.3 (a) Energy spectrum of a 2D double-spinless KzHNR [Eq. (3.1)] as a function of μ and p -wave pairing $\Delta = 0.5t$, for a KzHNR of width $N = 2$ and length $M = 200$. The numbers on the real axis represent the W associated with the corresponding topological region. (b) Schematic representation of the emergence of MZMs at the ends of the KzHNR for each associated W . Each semicircle represents an MZM generated on the site of the active border of the KzHNR. The two Majoranas connected with the dotted ellipses form a standard fermion. In the topological phase, unpaired Majorana fermions emerge at both ends of each KzHNR, as represented by the semicircles outside the dotted ellipses. The situations (I) and (III) describes $W = 1$, where only the top or bottom KzHNR generates one MZM at each of its ends. Otherwise, in (II) $W = 2$, indicating that both the KzHNRs generate MZMs simultaneously at their corresponding ends.
- 3.4 Scheme of the basis adopted in the Hamiltonian given by the Eqs. (4-8) describing the finite double-spin KzHNR chain of width $N = 2$. The unit cell B , represented by the dashed rectangular area is built with four distinct atoms a_i , b_i , c_i and d_i

- 3.5 Formation of MZMs parameter study: Energy spectra for a $N = 2$ finite double-spin KzHNR as a function of μ . We employed the same parameters set used in all the simulations of the work: $\Delta = 0.5t$, $\lambda_R = 0.05t$ and $\lambda_Z = 0.1t$, but only changing the particular parameter indicated in the figure: I) Length: $M = 10, 50, 100$. II) Extrinsic Rashba spin-orbit coupling $\lambda_R = 0.01t, 0.03t, 0.05t$. III) Superconductor pairing $\Delta = 0.1t, 0.3t, 0.5t$. IV) EMF $\lambda_Z = 0.005t, 0.03, 0.08t$.
- 3.6 (a) Energy spectra of a finite double-spin KzHNR [Eq. 3.15] as a function of μ , $N = 2$ and $M = 200$. The model parameters are $\Delta = 0.5t$, $\lambda_R = 0.05t$ and $\lambda_Z = 0.1t$. The blue and red colors correspond to spin up and down regions at the real axis, respectively. The green lines describe the formation of a regular fermion coming from the combination of Majorana excitations belonging to opposite KzHNRs. (b) Zoomed region of (a) around $E = 0$ for $\mu < 0$, showing in detail the formation of spin-polarized MZMs.
- 4.1 (Color online) Si SNR on Ag(110) surface. (a) and (b) Experimental STM images (uncorrected drift), (c) High-resolution nc-AFM image. (d) Top and cross view of the arrangement of the Si pentagonal building blocks. (a) and (b) Courtesy Eric Salomon, (c) Reprinted with permission from (1). Copyright 2023 American Chemical Society. (d) From Cerda et al.(2).
- 4.2 (Color online) (a) Penta-silicene (p-SiNRs) lattice transformation adopted. (b) Penta-silicene angles. (c) Sketch of nonequivalent Si atoms placed at the vertices of the “square” pentagonal lattice. We also represent the unit cell employed by the atoms inside the dashed rectangle in the simulations.
- 4.3 (Color online) Sketch of the penta-silicene nanoribbons: The penta-silicene system can be viewed as a top and a bottom Kitaev chains hybridized via hopping t . The ellipses represent the superconducting p -wave pairing between the pink (above) and yellow (below) silicon atoms (in the real material, these atoms correspond to the bucked one). The arrows only indicate the spin polarization needed to define a Kitaev chain.
- 4.4 Representation of the simplified pentasilicene scheme with x-projections

- 4.5 Energy dispersion of the bulk system as a function of the chemical potential μ , for the spinless p-SiNR with p -wave superconducting pairing between the atoms localized at the edges, cf. Eq. (1) of the main text. The Zak phase φ_{Zak} , represented by the values 0, 1, and 2, corresponds to the number of MZMs present at the edges of either one or both chains comprising the p-SiNR.
- 4.6 (Color online) **Spinless case: (a)-(c)** Bulk energy dispersion for the spinless p-SiNRs as a function of k_x , for $\mu = 0.0t$, $0.4t$, and $0.7t$, respectively. **(d)** Energy spectrum as a function of the chemical potential. Vertical lines indicate the chosen values of chemical potential shown on top Figs. **(e)-(g)** The energy spectrum with labels the energy levels in increasing order for $\mu = 0.0t$, $0.4t$, and $0.7t$, respectively. **(i)-(k)** Probability density [Eq. (4.34)] associated with zero-energy states, as a function of the lattice site $N = 1 \dots 100$
- 4.7 (Color online) **Spinful case - Magnetic field up: (a)-(e)** Bulk energy dispersion of the superconducting p-SiNRs for the spinful situation, as a function of k_x , for $\mu = -2.7t$, $-2.35t$, $1.1t$, $2.09t$ and $2.2t$, respectively. **(f)** Energy spectrum as a function of the chemical potential. Vertical lines indicate the chosen values of chemical potential shown on top Figs. **(g)-(k)** Energy levels sorted in ascending order. respectively. **(l)-(q)** Probability density [Eq. (4.34)] associated with zero-energy states, as a function of the lattice site $N = 1 \dots 100$
- 4.8 (Color online) **Spinful case - Magnetic field down:** The same situation of Fig. 4.7 but with the magnetic field pointing in the opposed direction.
- 4.9 (Color online) Analysis in detail of the $\mu = 0$ case of Fig. 4.7 with the magnetic field pointing in the up direction.
- 4.10 (Color online) Energy spectrum as a function of the chemical potential μ , for distinct lengths of superconducting p-SiNRs N , namely, for $N = 10$ **(a)**, $N = 20$ **(b)**, $N = 40$ **(c)**, $N = 60$ **(d)** and $N = 100$ **(e)**.

CONTENTS

CHAPTER 1 – INTRODUCTION	18
CHAPTER 2 – THEORETICAL BACKGROUND	22
2.1 SSH Model	22
2.2 Rice-Mele chain	28
2.3 Finite SSH and Rice Mele Chains	33
2.4 Spinful SSH Chain	38
2.5 Rice-Mele Model with spin	
2.6 Kitaev chain	
3.1 Introduction	
3.2 Spinless model and topological phase transitions	
3.3 Phase Transition Calculation in the Spinless Case	
3.4 Spin full model and emergence of spin-polarized MZMs	
3.5 Experimental perspectives	
3.6 Conclusions	
4.1 Introduction	
4.2 Lattice transformations	
4.3 Effective Hamiltonian - spinless case	
4.3.1 Bulk calculations	
4.4 Superconductor coupling	

4.5	Topological Classification and Zak phase topological invariant
4.6	Effective Hamiltonian - spinful case
4.7	Finite spinless p-SiNRs
4.8	Finite spinful p-SiNRs
4.9	Conclusions and Perspectives

APÊNDICE A – STEP-BY-STEP EXPLANATION OF THE CHIRAL MATRIX CALCULATION

REFERÊNCIAS

Chapter 1

INTRODUCTION

Since the synthesis of graphene, two-dimensional materials have attracted much interest, both from theoretical and experimental points of view. From a theoretical perspective, several models were made for the prediction of electronic properties, and with these studies, new analysis techniques were introduced. One technique that has garnered significant interest is the utilization of topological concepts in materials. This involves examining how energy bands evolve in response to varying parameters, such as the chemical potential. This approach will be extensively employed starting from the second chapter, particularly in the discussion of the Kitaev chain model. (3).

In chapter two we will give a small introduction to some models that will be important for understanding the thesis, we will briefly mention their subsections

In subsection One, we provide an introductory exploration into understanding topological models through the lens of the Su-Schrieffer-Heeger (SSH) model—a fundamental model showcasing topology (4). Through this model, we delve into the analysis of electronic band structures, energy spectra of finite systems, and wave functions, unveiling their inherent topological properties. This foundational understanding sets the stage for our examination of various systems that exhibit topological characteristics or are categorized as such. The incorporation of these concepts within condensed matter physics enables us to reevaluate numerous models and categorize them through a topological point of view.

In subsection two, we investigate generalized SSH chains, known as the Rice-Mele (5) model. Our objective is to understand the consequences of these generalizations and how they affect the behavior of SSH with new parameters, also impacting localized zero energy states (6).

In subsection three we focus on the effect of applying external magnetic fields (Zeeman effect) to these structures, breaking spin degeneracy and consequently breaking the time-reversal symmetry. So we will analyze the SSH and Rice-Mele models with these new elements and

show the effect on the energy levels. We will add a spin texture to better visualize the changes in the bands, considering both the topological and electronic aspects and their impact on electronic structures.

In the fourth and final subsection, motivated by Kitaev's ideas, researchers conducted experiments over the last decade (7–10). They used thin wires, *s*-wave superconductors and magnets, in an attempt to observe zero Majorana modes (MZMs) under specific conditions (11). The domain of MZMs has expanded with innovative configurations, such as hybrid systems combining semiconductors (12) and the fusion of chains of ferromagnetic atoms with specific superconductors (13, 14).

The Kitaev chain has a central role in the thesis, and the two main results depend both on the application of the concepts of the Kitaev chain and on the model itself. The Kitaev chain is a toy model where the main element to be explored is the superconducting coupling, so using that new ingredient we will explore the chain with the techniques seen in the previous sections, and add a small discussion about Majorana fermions which would be the main phenomenon associated with the chain of Kitaev.

Now with these three main components: hopping of first neighbors studied in the chains, spin effects, and superconductivity, we will build a model for hexagonal nanoribbons where we will also characterize the model from the topological point of view of the system.

No third chapter will present the model of the hexagonal nanoribbons, the edges of zigzag nanoribbons exhibit a magnetic order, making them favorable sites for the emergence of Majorana fermions at the ribbon ends. However, the spins along these edges aren't fully aligned. The material's bands feature crossings with different spin orientations. To convert these crossings into a Kitaev chain, spin organization is necessary because the system requires spin polarization to exhibit the effects characteristic of the Kitaev chain. Fortunately, established methodologies exist in the literature (15), and many models could potentially demonstrate Majorana fermions due to the straightforward requirements (16). Essentially, a superconductor is needed where certain spins and time-reversal symmetries are eliminated. By varying parameters such as the chemical potential, we can open and close gaps in the material's energy levels.

In our investigation, closing this gap in a finite zigzag nanoribbon marks a transition from a conventional region to a distinct topological one. At this juncture, Majorana fermions emerge at the ribbon ends with zero energy. Our model serves as a basic framework for examining these ribbons, considering fundamental factors such as nearest-neighbor atomic interactions, spin dynamics, superconducting connections at the edges, and the influence of an external magnetic field.

Analyzing the model for infinite zigzag nanoribbons revealed various transitions between different topological phases, correlated with organized-spin Majorana fermions. Essentially, we identified regions within the material where only Majorana fermions with spins aligned either up or down were present. Furthermore, we established a direct linkage between these model transitions and the appearance of zero-energy Majorana fermions in the finite-length version, constituting the primary finding of the third section of our study, which resulted in a published paper (17).

Our study emphasizes the ability of MZMs to distinguish the spin in double-spin zigzag honeycomb nanoribbons (KzHNRs) of the Kitaev model. This arrangement offers a new perspective for identifying the spin states of MZMs beyond traditional 1D Majorana threads. Our findings inspire cutting-edge experimental efforts, especially those aimed at spin-polarized MZMs in silicene-based zHNRs paired with a Pb superconductor, incorporating Rashba spin-orbit coupling (RSOC) and an external magnetic field (EMF).

Motivated by the work of ZGNRs, Finally, after a quarter of a chapter, we will present you with pentagonal nanoribbons a new type of material that in principle has a structure made experimentally, silicene, a two-dimensional layer of silicon atoms, which has gained prominence as a potential basis for tiny electronic devices (18–20). Penta-silicene nanoribbons (p-SiNRs) on Ag(110) substrates have emerged as a testing ground for theories related to MZMs, particularly the Kitaev (2, 17) model. Although concrete evidence for MZMs in current settings remains elusive (21, 22), researchers are optimistic that p-SiNRs can provide vital insights for new types of topological phases where we will have spin polarized majoranas (17).

Our initial exploration addressed a hexagonal configuration model, using graphene or silicene as the base material. We analyze these structures under various parameters, creating a platform for Majorana fermions and topological states. In the same way, we will now propose a model based on Pentasilicene, characterized by its irregular pentagonal shape, to build a theoretical model that would predict its topological dynamics without increasing complexity (23). The interesting thing about this lattice is the symmetry breaking in real space and we can analyze a model completely different from the one previously analyzed.

In the field of quantum computing, silicon nanowires, especially those with topological properties, have potential as bases for (24) quantum computing systems. Challenges persist, as even closely located nanowires exhibiting robust spin-orbit coupling have yet to conclusively showcase topologically protected MZMs (21, 22). The researchers seek to experimentally manifest the Kitaev model on a silicon-based platform (3).

we conclude in chapter five with a summary of our results and mention the publications that

resulted from the work presented in this thesis.

Chapter 2

THEORETICAL BACKGROUND

In this chapter, we will explore basic models to comprehend the following two chapters. In the first section, we will introduce the SSH model, which is a simple model but helps understand how topological model analyses can be conducted. In the second section, we introduce the Rice-Mele model (25), which serves as an extension of the SSH model where the chiral symmetry of the SSH model is broken, offering a more comprehensive perspective. It provides valuable insights into the changes and behaviors observed in topological systems and will discuss its impacts on topological analyses.

In the third section, we will provide a brief introduction to the finite model for the systems presented (SSH and Rice-Mele).

In sections four and five, we will introduce an external magnetic field to both presented models and discuss how the behavior changes with this new parameter.

In section six, we will introduce the Kitaev model (3), which is the main model to understand the following two chapters as it introduces triplet-type superconducting pairing to the problem. We will also discuss Majorana fermions and how they appear in one-dimensional systems.

2.1 SSH Model

The SSH model is important in the study of one-dimensional topological chains, offering a simple exploration of topology. It was inspired by Trans-polyacetylene, a carbon chain known for its alternating double and single bonds. In the SSH model, we only look at electron energies, so all energy modes studied in both this section and the next section do not have Majorana zero modes, this is because in the SSH model there is no p-type superconducting pairing, which is the main ingredient for the emergence of Majorana fermions, which will be presented in the next topic along with the Kitaev chain. Some works may have other approaches on how Majorana

fermions can appear in this type of system (26, 27), but here, we simply aim to understand the behavior of a simple chain. Similarly, the SSH model is a linear chain of uniform atoms connected by hopping interactions V_1 and V_2 . This mimics the double and single bonds in Trans-polyacetylene. To understand the complexity and its properties, we use the effective tight-binding model, as discussed earlier. In this explanation, we will present the model structure by examining its associated Hamiltonian

$$\mathcal{H}_{SSH} = \sum_n V_1 a_n b_n^\dagger + V_2 a_n b_{n-1}^\dagger + H.c., \quad (2.1)$$

Where a unit cell runs as a region starting in orange in the Fig2.1

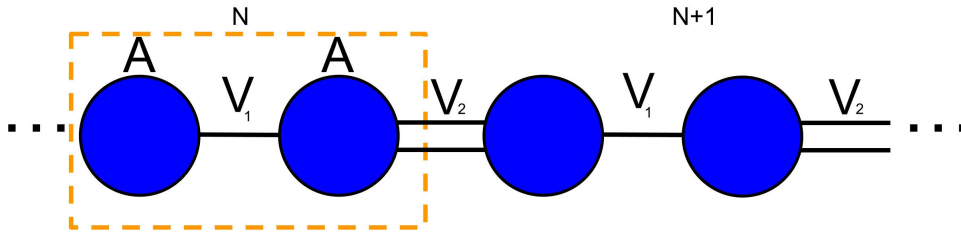


Figure 2.1: Scheme showing the model of the SSH chain with a chain with the same atom (in blue) with alternating bonds V_1 and V_2

In Hamiltonian Eq.(2.1), the operators a^\dagger and a represent the creation and annihilation operators, respectively. In this notation, an electron is annihilated at site "n" and created at site "n+1". The parameter V_1 corresponds to the energy probability associated with this event, commonly known as hopping.

Figure 2.1 provides a schematic illustration of the SSH chain. In this diagram, we can observe that there are two atoms per unit cell connected by V_1 and V_2 is the coupling between neighboring cells, rendering them non-equivalent. Specifically, on the left side of atom A, there is a V_1 bond, while on the right side, there is a V_2 bond. Conversely, for atom A, the situation is reversed; the left side has a V_2 bond, and the right side has a V_1 bond. Consequently, the unit cell is delineated by the orange rectangle. To initiate the physical characterization of the system, it is crucial to construct a set of graphs to characterize the band structure and energies of the finite system that offer insights into the system's behavior.

The first step in this process involves using the Hamiltonian and performing a Fourier transform. This transformation takes us into reciprocal space (k-space), where we work with wave vectors k and can examine the structure of degenerate bands to understand how the model is established to make the band structure.

To derive the band structure in reciprocal space, we conduct the Fourier transform. To elucidate this procedure, let us analyze the effects of the operators on the atoms within the unit cell:

$$a_k = \frac{1}{\sqrt{N}} \sum_i^N a_i e^{i\vec{k} \cdot \vec{r}_i} \quad ; \quad a_k^\dagger = \frac{1}{\sqrt{N}} \sum_i^N a_i e^{-i\vec{k} \cdot \vec{r}_i} \quad (2.2)$$

In Eq. (2.5), the operators a_k and a_k^\dagger in reciprocal space are derived from the original operators a_n and a_n^\dagger in real space through a Fourier transform. This transformation involves summing over all unit cells (N) and multiplying each term by a phase factor determined by the wave vector \vec{k} and the position vector \vec{r}_i of the unit cells. These transformations yield valuable insights into the electronic properties and band structure of the SSH chain in reciprocal space, we can also observe that there is chirality in this system as there is a matrix S that respects $SH(k)_{SSH}S = H(k)_{SSH}$.

The SSH model with the Fourier transform can be expressed in matrix form.

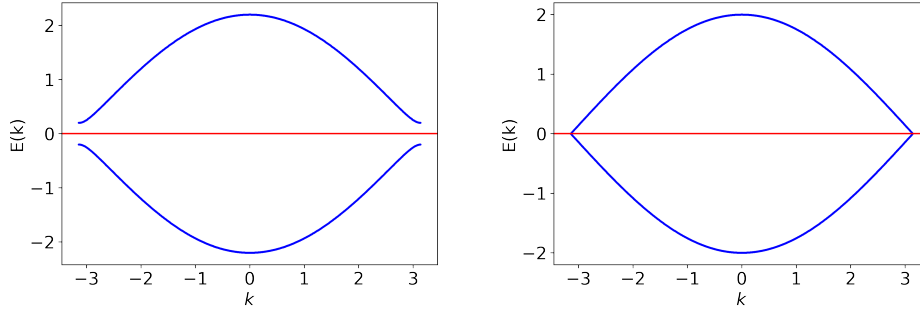
$$H(k)_{SSH} = \begin{bmatrix} a^\dagger & b^\dagger \end{bmatrix} \begin{bmatrix} 0 & V_1 + V_2 e^{ik} \\ V_1 + V_2 e^{-ik} & 0 \end{bmatrix} \begin{bmatrix} a \\ b \end{bmatrix} \quad (2.3)$$

With this matrix form, we can create a program to analyze the accessible eigenvalues of the system for a specific set of values. In this case, I will fix the parameter $V_1 = 1$ and vary the parameter V_2 freely, allowing us to obtain the corresponding graphs.

In the following graphs, Fig. (2.2a), Fig. (2.2b), and Fig. 2.2c, we observe different band structure variations, representing distinct phases in the SSH model. These phases include an insulating state with a band gap, a metallic state with a gapless band, and a topological insulator state with a unique gapped band pattern. Let us briefly explore each phase before delving into energy dispersion plots.

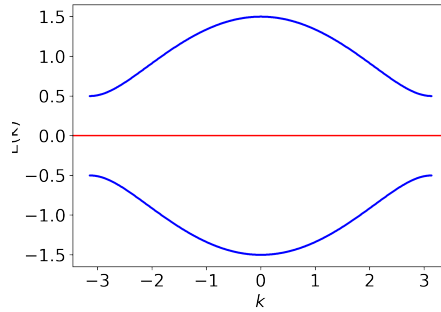
Fig. (2.2a) illustrates the insulating phase, where electrons are confined to the lower energy band. The Fermi energy determines the band occupation, resulting in only the lower half being filled. Because of the absence of accessible states in the system, electron mobility is severely restricted, leading to insulating behavior.

In Fig. (2.2b), we observe the metallic phase, characterized by the touching or crossing of the two energy bands at a specific point. The Fermi energy remains at zero, favoring electronic transitions between nearby energy levels gapless. This allows electrons to flow freely, leading to electrical conductivity in the material.



(a) SSH Band Structure at $V_2 = 1.2$: This subfigure displays the band structure of the SSH model with $V_2 = 1.2$, representing an insulating phase.

(b) SSH Band Structure at $V_2 = 1.0$: This subfigure shows the band structure of the SSH model with $V_2 = 1.0$, illustrating the metallic phase.



(c) SSH Band Structure at $V_2 = 0.5$: This subfigure exhibits the band structure of the SSH model with $V_2 = 0.5$, highlighting the topological insulator phase.

In Fig. (2.2c), we find the topological insulator state, a fascinating phase that exhibits unique band structure characteristics. Unlike conventional insulators, the topological insulator possesses an insulating behavior in the bulk of the material but harbors conducting states along its edges or surfaces, known as edge states. Here we cannot observe any effective difference in the band structure for the infinite case because we are looking at the energy states of the bulk, so we will have to do other analyzes of the energy of the finite system.

To generate the energy dispersion plot, we will use the Hamiltonian (2.1). However, this time, we will apply it to a finite system. This involves selecting a specific number, N , of unit cells to form a finite chain, leading to a matrix representation of the Hamiltonian.

This approach allows us to investigate how the energies of the finite system change when one of the hoppings varies while the other remains constant in this one-dimensional chain. Employing this method enhances our comprehension of the specific topological alterations present within the system.

To proceed with the construction of the energy dispersion plot, we will employ numerical methods and utilize a computational program to diagonalize the matrix and obtain its eigenval-

ues. By systematically varying the parameter V_2 , we can explore the behavior of the system and obtain the corresponding energy energies.

The energy dispersion will then depict the relationship between the energy and the parameter V_2 . This allows us to visualize how the electronic states in the SSH chain respond to changes in the coupling strength V_2 and gain insights into the energy dispersion of the finite system.

This approach enables us to study the electronic properties of the SSH chain in a finite setting, providing valuable information about its energy levels and electronic band behavior, which is crucial for understanding the behavior of one-dimensional systems and exploring their potential applications in various areas of condensed matter physics.

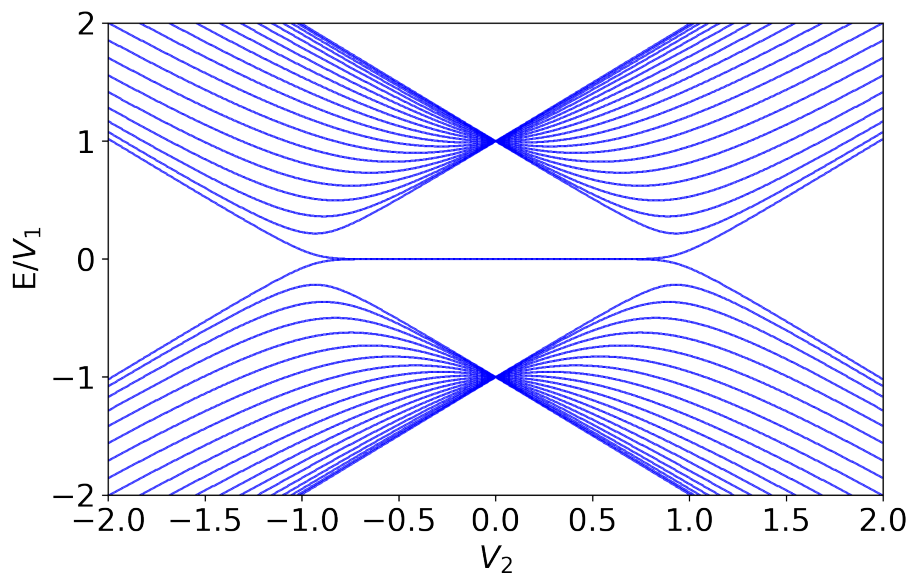


Figure 2.3: Energy Dispersion in Finite SSH Chain: This figure presents the energy dispersion plot for a finite SSH chain with V_2 varying, picture the band gap in the energy spectrum and its relationship with the bulk transition with V_2 varying.

The energy dispersion plot shown in Fig. 2.3 illustrates the behavior of the finite SSH chain as a function of the parameter V_2 . Each value of V_2 corresponds to a particular system configuration, and within each of them, there are multiple accessible energy levels.

In this specific case, we can observe that there is a range of energies centered around zero within the system. This region extends from approximately -1 to 1, indicating a band gap (this gap is exact for infinite chain) in the energy spectrum. This interesting transition aligns with the Bulk transition, establishing a significant relationship known as the bulk-bound correspondence, which implies the presence of a phase transition in the system.

Further investigation into the correlation between these two graphs would provide valuable

insights into the underlying physics of the SSH chain and its finite behavior. Before proceeding with this analysis, it is essential to calculate the wave functions for a finite system. For this purpose, I will perform the necessary calculations to explore the electronic states within the finite SSH chain thoroughly.

This calculation incorporates the previously obtained eigenvectors for the finite case, enabling us to examine all possible wave functions within the system. Focus specifically on wave functions corresponding to zero energy. Now we can create a new graph of the energies of the finite system as a function of its size n where we can observe whether for a given value of V_2 we have zero energies which are the localized and topologically protected edge states

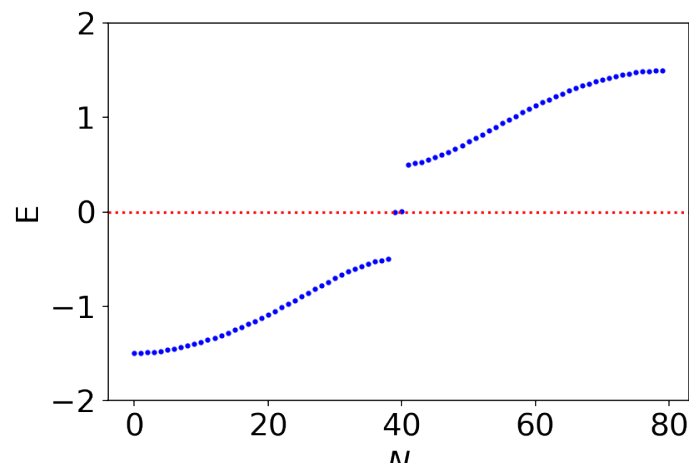


Figure 2.4: Zero-Energy States in Finite SSH Chain: This figure displays energy eigenvalues as a function of n for a finite SSH chain, emphasizing the existence of zero-energy states and their implications.

In Fig 2.4, we can see that there are only two energies at zero, and we filter out these energies to plot the vectors (eigenvectors) by n which is the size of the one-dimensional system, obtaining the wave functions at zero as follows. Here, we do not see Majorana fermions because our model does not have superconduction coupling. Therefore, we are examining only the potential energies of two electrons in the chain.

To characterize the phase transition in the SSH model, we make use of a combination of graphs, each providing valuable insights into the system behavior. The different plots contribute to a comprehensive understanding of the topological phase transition:

In fig2.2b The bulk plot displays the opening and closing of the band gap as the parameter V_2 varies. Although this observation alone does not offer conclusive evidence, it serves as an initial indication of a potential topological phase transition.

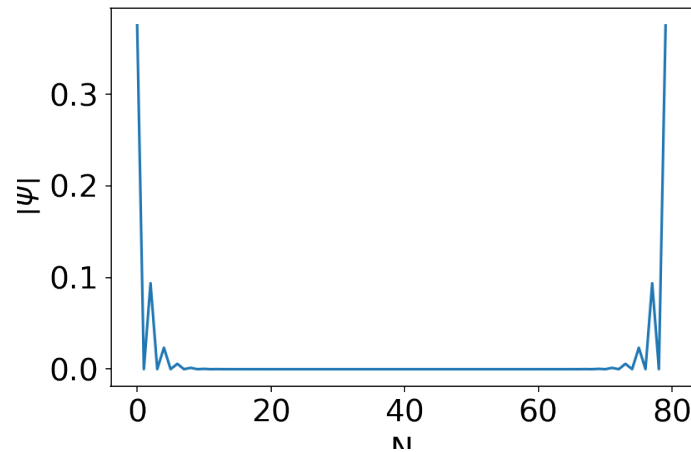


Figure 2.5: Squared wave function or probability per site in SSH Chain: This figure showcases wave functions within a finite SSH chain, particularly focusing on zero-energy states and electron localization at the chain edge.

In fig2.3 the finite SSH chain plot, we find zero-energy states occurring at specific values of V_2 associated with the phase transition. For example, when $V_2 = 1$, the gap closes, and the system exhibits zero-energy modes, further supporting the occurrence of a topological phase transition here we are in phase transition and we have no localized edge states.

In fig2.4 the energy for a fixed V_2 in the region with zero-energy modes (e.g., $V_2 = 0.5$), we identify two zero-energy states. This specific analysis provides more detailed information about the corresponding wave functions and adds to the evidence for the topological transition.

In fig2.5 The computation of the wave functions for a particular value of V_2 (e.g., $V_2 = 0.5$) reveals electron states localized at the edges of the system. This observation reinforces the notion of a topological phase transition without requiring the calculation of more complex topological invariants like the Chern number which will be explained later.

In subsequent chapters, our research will search into the numerical calculation of various topological invariants for other systems. The initial numerical approach has laid the groundwork for further investigations in our work.

2.2 Rice-Mele chain

Now we would like to introduce another model, which is a generalization of the SSH model. Instead of having the same atom repeating in the chain, we would have two different atoms. It may seem like a simplistic generalization, but this model hides a rich physics, especially in its structure. First, let us write it Hamiltonian. Here we are interested in knowing how the topology

of the system would change for a chain with two different types of atoms with different system energies.

$$H_t = \sum_n (\varepsilon - \mu) a_n a_n^\dagger - (\varepsilon + \mu) b_n b_n^\dagger + \sum_n V_1 a_n b_n^\dagger + V_2 a_n b_{n-1}^\dagger + H.c. \quad (2.4)$$

Where a unit cell runs as a region starting in orange in Fig. 2.6 With the Hamiltonian defined, the

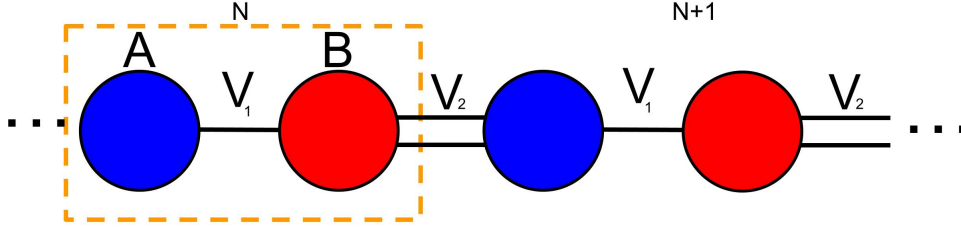


Figure 2.6: Scheme showing the Rice-Mele chain model with a chain with two different atoms (in blue and red) with alternating bonds V_1 and V_2

key distinction lies in the terms ε_1 and ε_2 which are the energies of sites A and B, respectively but here we are interested in a specific case where $\varepsilon_1 = -\varepsilon_2 = \varepsilon$ which is the case of Eq.2.4, which govern the energies of the sites in the generalized SSH model. In this chain, the first site is denoted as $N = 1$, where the operators $a_{i,\alpha}^\dagger$ and $b_{j,\alpha}$ create and annihilate electrons at site A and B in the unit cell, respectively. Employing the Fourier transform allows us to explore the band structure in reciprocal space, providing valuable insights into the electronic properties of the system.

Here we will do the Fourier transform in the same way as we did previously, but now we have two different types of sites A and B:

$$\begin{aligned} a_k &= \frac{1}{\sqrt{N}} \sum_i^N a_i e^{i\vec{k} \cdot \vec{r}_i} & ; & & a_k^\dagger &= \frac{1}{\sqrt{N}} \sum_i^N a_i e^{-i\vec{k} \cdot \vec{r}_i} \\ b_k &= \frac{1}{\sqrt{N}} \sum_i^N b_i e^{i\vec{k} \cdot \vec{r}_i} & ; & & b_k^\dagger &= \frac{1}{\sqrt{N}} \sum_i^N b_i e^{-i\vec{k} \cdot \vec{r}_i} \end{aligned} \quad (2.5)$$

The Hamiltonian in reciprocal space takes the form:

$$\begin{aligned} H_t &= \sum_n \sum_{k_x} \sum_{k'_x} (\varepsilon - \mu) \frac{1}{N} a_k^\dagger e^{-i\vec{k}n} a_{k'} e^{i\vec{k}'n} + (-\varepsilon - \mu) \frac{1}{N} b_k^\dagger e^{-i\vec{k}n} b_{k'} e^{i\vec{k}'n} + \\ &V_1 \frac{1}{N} a_k^\dagger e^{-i\vec{k}n} b_{k'} e^{i\vec{k}'n} + V_2 \frac{1}{N} a_k^\dagger e^{-i\vec{k}n} b_{k'} e^{i\vec{k}'n-1} + h.c.. \end{aligned} \quad (2.6)$$

we can organize like

$$\begin{aligned}
H_t = & \sum_{k_x} \sum_{k'_x} (\varepsilon - \mu) a_k^\dagger a_{k'} \sum_n \frac{1}{N} e^{in(\vec{k}'_x - \vec{k}_x)} + (-\varepsilon - \mu) b_k^\dagger b_{k'} \sum_n \frac{1}{N} e^{in(\vec{k}'_x - \vec{k}_x)} \\
& + V1 a_k^\dagger b_{k'} \sum_n \frac{1}{N} e^{in(\vec{k}'_x - \vec{k}_x)} + V2 (e^{-ik'}) a_k^\dagger b_{k'} \sum_n \frac{1}{N} e^{in(\vec{k}'_x - \vec{k}_x)} + h.c..
\end{aligned} \tag{2.7}$$

but $\sum_n \frac{1}{N} e^{in(\vec{k}' - \vec{k})} = \delta_{k,k'}$ this,

$$H_t = \sum_{k_x} \sum_{k'_x} (\varepsilon - \mu) a_k^\dagger a_{k'} \delta_{k,k'} + (-\varepsilon - \mu) b_k^\dagger b_{k'} \delta_{k,k'} + V1 a_k^\dagger b_{k'} \delta_{k,k'} + V2 (e^{-ik'}) a_k^\dagger b_{k'} \delta_{k,k'} + h.c.. \tag{2.8}$$

Performing the sum into k' , we can express the Hamiltonian as:

$$H_t = \sum_{k_x} (\varepsilon - \mu) a_k^\dagger a_k + (-\varepsilon - \mu) b_k^\dagger b_k + V1 a_k^\dagger b_k + V2 (e^{-ik}) a_k^\dagger b_k + h.c.. \tag{2.9}$$

we can now observe that there is no chirality in this Hamiltonian because is not a matrix S that respects $SH(k)_{SSH}S = H(k)_{SSH}$ like in the SSH model 2.3.

$$H_t = \begin{pmatrix} \varepsilon - \mu & V1 + V2(e^{-ik}) \\ V1 + V2(e^{ik}) & -\varepsilon - \mu \end{pmatrix} \tag{2.10}$$

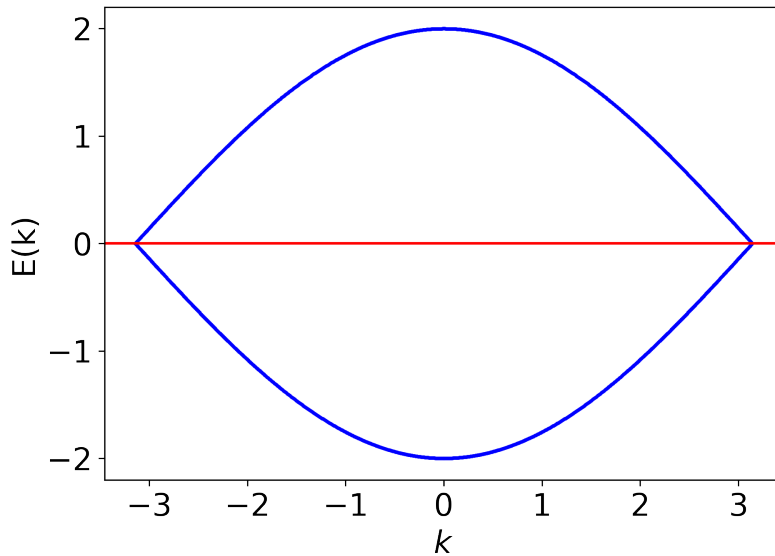


Figure 2.7: SSH Band Structure where $V_2 = 1t$.

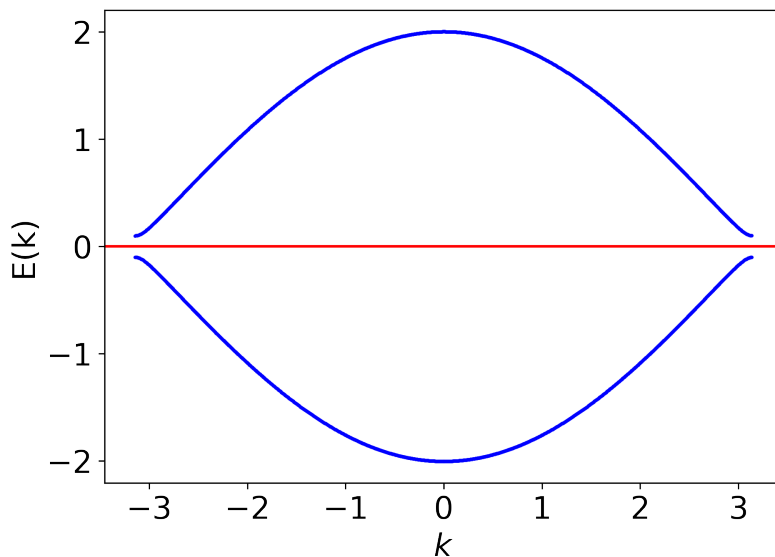


Figure 2.8: Rice Mele Band Structure ($\varepsilon = 0.1$) and $V_2 = 1t$.

as we can see in the upcoming figures, the energy gap only closes for epsilon equal to zero. This observation provides a deeper understanding of the energy band behavior under specific parameter settings.

As we search deeper into the analysis of the band structure across a variety of parameters, similar observations are made as in the finite case. Particularly of note is the parameter $V_2 = 1t$, which serves as a pivotal value for our explorations because at this value we indicate a topological phase transition.

In our thorough examination of band structures, various interesting patterns and features become apparent because depending on the parameter V_1 we have metallic structures and structures with gaps, so we will show some points about these analyzes.

From our presented information, a key point is the behavior of the energy gap. It becomes clear that this gap gets smaller, especially when epsilon is zero. This observation enhances our understanding, because with the variation of a parameter we can control the gap.

As we go deeper into analyzing the band structure, we start to notice both similarities and differences compared to previous model (SSH) in finite systems. An important factor in our analysis is the parameter $V_2 = 1t$, which has consistently played a significant role in energy levels of the energy spectrum.

Figure (2.7) offers valuable insights into this investigation. In this figure, we see the band structure as defined by the Hamiltonian in Equation (2.10). Among the various V_1 values shown,

the emergence of a zero-gap semiconductor is especially noteworthy. This observation may suggest a potential phase transition, a hypothesis that gains credibility, especially when the parameter V_2 is adjusted to $1t$.

Additionally, Figure (2.9) highlights another aspect of our investigation. It reveals a distinct band gap whenever $\varepsilon \neq 0$, a behavior that distinguishes it from patterns documented in previous studies.

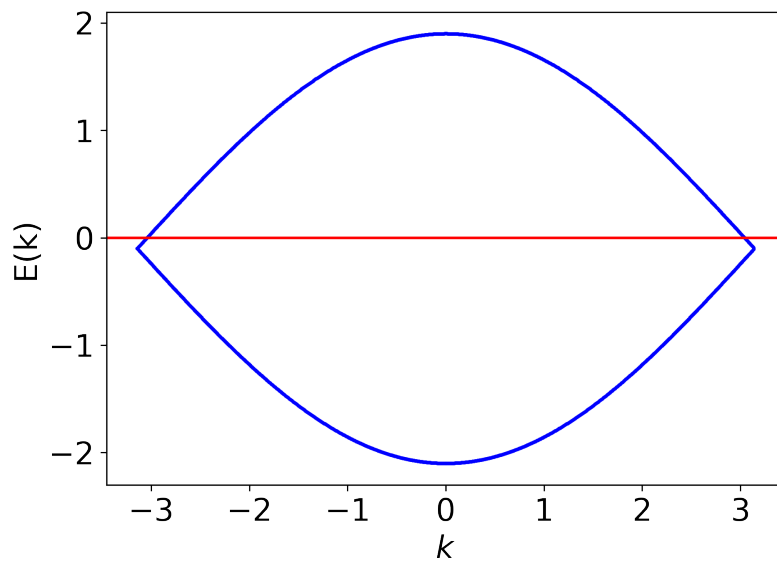


Figure 2.9: Band structure of the Eq.2.10. Here we can see that the band structure is shifted by ε value downwards the red line is the fermi energy $E(k)=0$ when $\varepsilon \neq 0$.

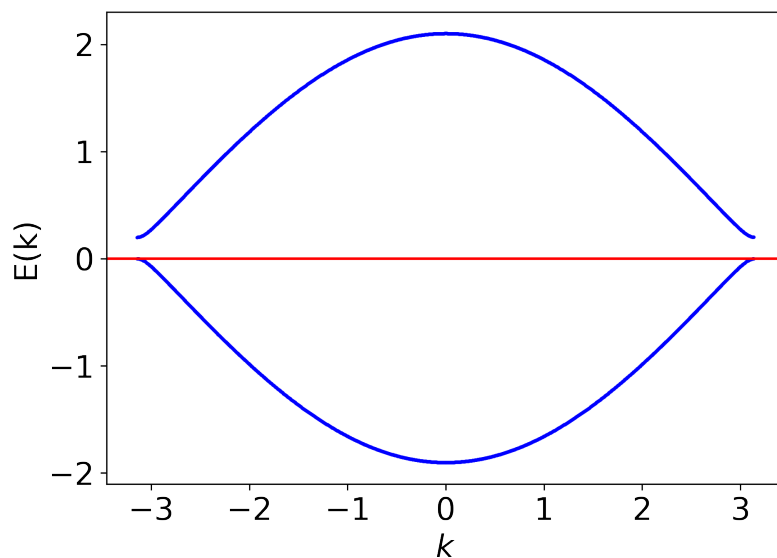


Figure 2.10: Visual depiction of the band structure as dictated by the Hamiltonian in Eq.2.10. Highlights the unique position of the Fermi level when $\varepsilon = \mu \neq 0$.

A noteworthy observation pertains to the Fermi level. When we set $\varepsilon = 0.1$ and $\mu = -\varepsilon$ as our parameters, the Fermi level precisely intersects the peak of the valence band. However, when μ matches ε , it tends to align itself with the conduction band.

Taken together, these observations and figures provide a detailed understanding of the various subtleties associated with band structures, particularly within the context of the infinite form framework.

2.3 Finite SSH and Rice Mele Chains

This section explores the intricacies of energy dispersion patterns governed by the Hamiltonian, specifically particularized for a system with $N = 40$ atoms. The figures presented here illuminate the dispersion characteristics under various values of chemical potentials (μ) and site energies (ε).

When we shift our focus to a finite system with a limited number of atoms, we can compute the energy levels supported by the system for each value of t_1 . Notably, this system exhibits a different behavior compared to the SSH model, which features a plateau at zero energy. Instead, in this case, we observe two distinct shifted plateaus, one at a positive epsilon value and the other at a negative epsilon value. To modify this behavior, Now we will demonstrate cases where the chemical potential is non-zero because with this analysis we will see that there are cases from a topological point of view and zero energy modes. This addition allows us to control the occupation of the Fermi level, with this adjustment, we can set one of the plateaus to zero energy, resulting in a difference of two epsilon units between the two plateaus as we can see in(2.13).

Now, let us proceed to examine the energy levels of a specific system, for instance.

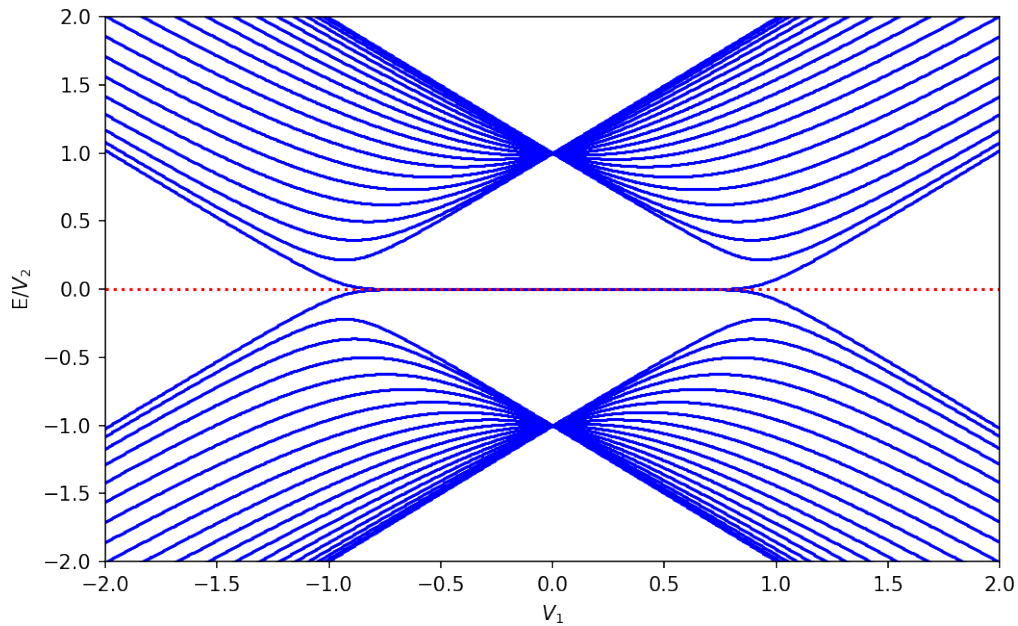


Figure 2.11: The energy dispersion described by the Hamiltonian in Eq.2.4, with parameters as shown in the graph. Notably, the presence of Zero Modes is evident, and a transition from a trivial to a topological phase becomes apparent at $V_2 = 1t$.

After looking at Figure 2.11, we can see that there are energy modes with zero energy in the red line on the graph. These zero-energy modes exist between the $V_1 = 1t$ and $V_1 = -1t$ regions in the finite system. These states with zero energy indicate a transition in the topological phase of the system. This means that for $V_1 > 1t$, the system has a gap and is considered trivial. However, the system exhibits localized energies in the region where these zero-energy states appear.

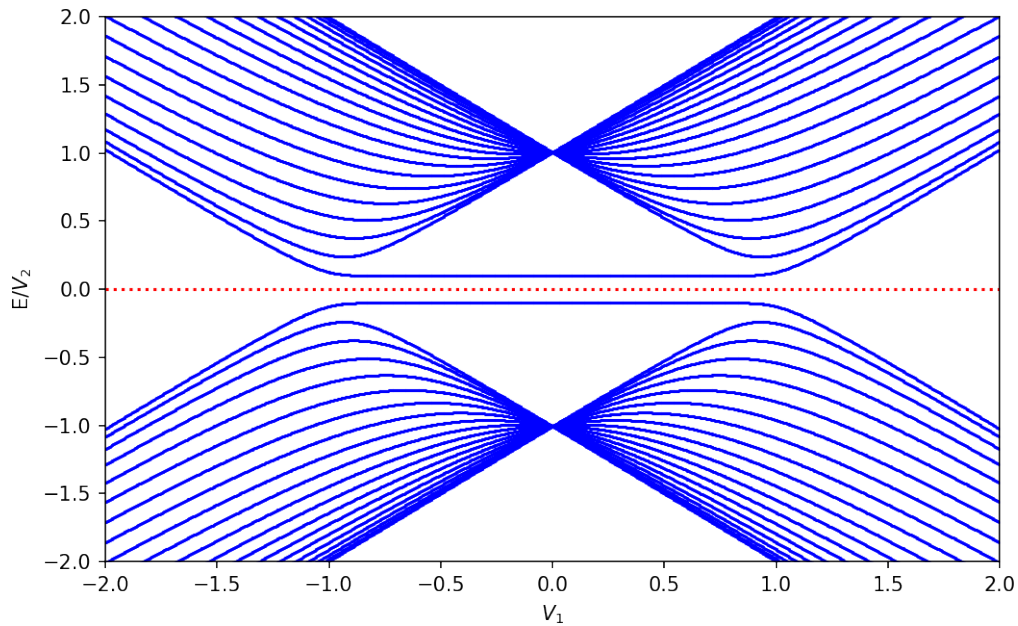


Figure 2.12: Energy spectrum of the Hamiltonian in Eq.2.4, with the parameter $\varepsilon = 0.1$. It is clear that when $\varepsilon \neq 0$, the zero modes disappear and now there is a gap separating the energies.

After analyzing Figure 2.12, we observe a shift away from the previous prevalence of zero-energy states. When a non-zero ε value is introduced, a gap emerges in the region where these zero-energy states used to dominate. This indicates that the system has become more responsive to variations in site energy.

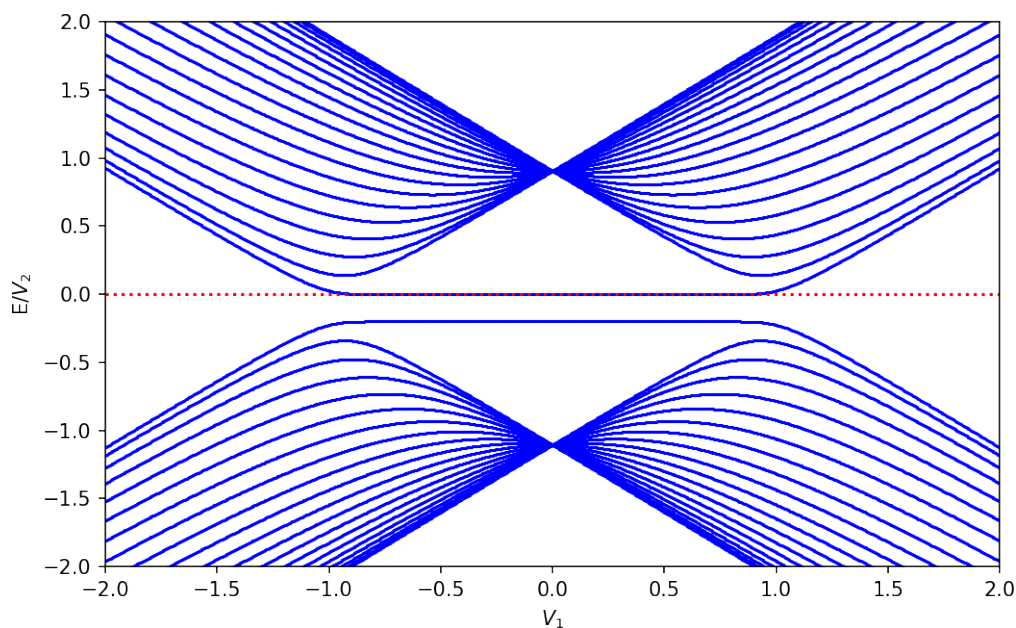


Figure 2.13: the Energy spectrum corresponds to the Hamiltonian described in Eq.2.4 and complies with the specified parameters $\varepsilon = 0.1$ and $\mu = 0.1$, the structure that previously featured a gap now reverts to zero modes, primarily due to the chemical potential aligning with the local energy level.

The patterns depicted in Figure 2.13 introduce an additional dimension to the conversation. When μ equals ε , the energy dispersion behavior undergoes a further alteration, reintroducing zero modes. This implies a subtle interplay between μ and ε , where they can either here we have two situations where we can have zero majorana modes where we have $\varepsilon = -\mu$ or $\varepsilon = \mu$.

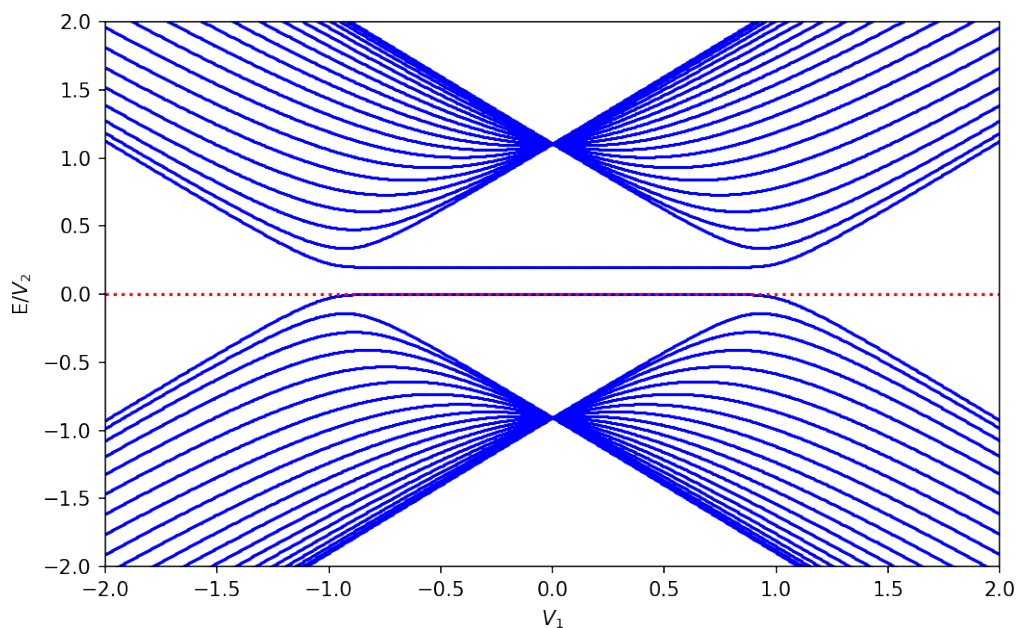


Figure 2.14: This figure presents the energy dispersion in line with the Hamiltonian from Eq.2.4 and the defined parameters. Observations reveal that with $\varepsilon = 0.1$ and $\mu = -0.1$, the structure that previously exhibited a gap now displays zero modes once again, a phenomenon resulting from the chemical potential being the negative counterpart of the local energy level.

Finally, Figure 2.14 highlights the reappearance of zero modes when μ equals the negative value of ε . This underscores the intricate interplay between the chemical potential and site energy in shaping the overall topological properties of the system.

In summary, these observations provide a comprehensive insight into energy dispersion patterns with varying V_1 . They emphasize the significant impacts of μ and ε on the topological traits of the system.

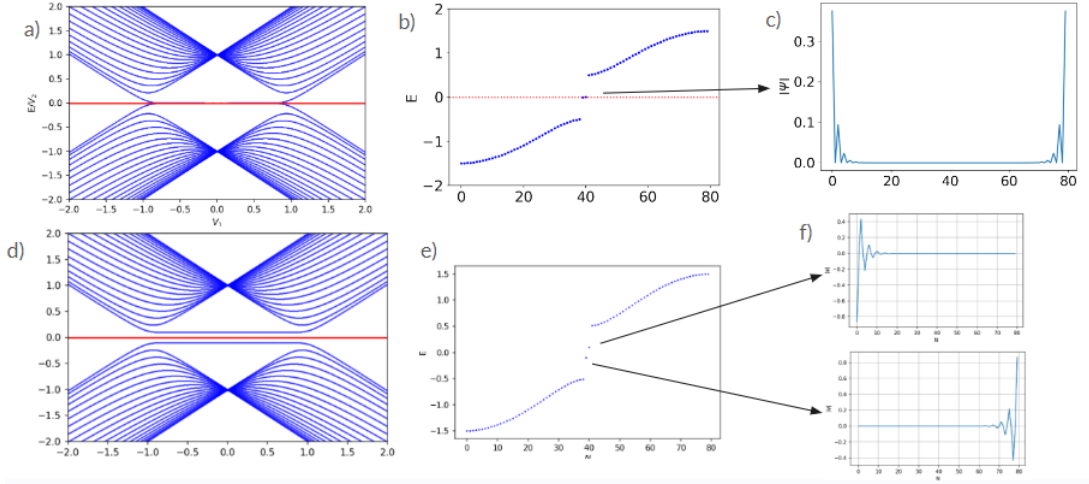


Figure 2.15: (a) SSH dispersion energy. (b) Energy per site in the SSH case for $V_1 = 0.5$. (c) Wave function of SSH zero modes for $V_1 = 0.5$. (d) Rice-Mele dispersion energy for $\epsilon = 0.1$. (e) Energy per site in the Rice-Mele case $\epsilon = 0.1$ and $V_1 = 0.5$. (f) Wave function of the Rice-mele shifted modes for $\epsilon = 0.1$ and $\epsilon = -0.1$ for $V_1 = 0.5$.

In the figure (2.15), we can see the case of SSH in (a), (b), (c) in (a) is the energy spectrum where we can see that there are zero energy modes depending on the value of V_1 , in (b) we have the energies per site of the system where we can see that we have two modes of energy at zero and in (c) are the wave functions of one of these two energy modes.

in the same figure we have in (d), (e) and (f) the behavior of Rice-Mele for $\epsilon = 0.1$, in (d) we can observe that we no longer have zero energy modes, but now we have a gap and two energy plateaus one for $\epsilon = 0.1$ and one for -0.1 . In (e) we have the energies per site for $V_1 = 0.5$ where we can see that where before in the ssh model we had two zero energy modes, now we have one energy shifted by 0.1 and one shifted by -0.1. In f) we can observe two wave functions, one located on the left and the other located on the right, which correspond to the modes described in f)

2.4 Spinful SSH Chain

In this section, we have introduced a new term to our SSH model, referred to as the Zeeman term, as presented in equation (2.12). This addition allows us to account for the influence of magnetism on our system. Consequently, our matrix representation expands to accommodate these changes. We now describe our system using a revised set:

$$\Phi = (a_{k,\sigma}, b_{k,\sigma}, a_{k,-\sigma}, b_{k,-\sigma})$$

When we examine the Hamiltonian in the vector k -space, our model transforms according to the representation shown in Eq. (2.14). As a result of this modification, we obtain new energy values, as we can see below. This provides an alternative perspective on understanding the SSH chain when spin considerations are taken into account.

The SSH Hamiltonian is given by:

$$\mathcal{H}_{SSH} = -V_1 \sum_n a_{n,\sigma}^\dagger a_{n,\sigma} - V_2 \sum_n a_{n+1,\sigma}^\dagger b_{n,\sigma} + H.c., \quad (2.11)$$

The Zeeman term is

$$H_Z = \sum_{n,\sigma} \lambda_z \text{sign}(\sigma) \left(a_{n,\sigma} a_{n,\sigma}^\dagger + b_{n,\sigma} b_{n,\sigma}^\dagger \right) + H.c. \quad (2.12)$$

where the term sigma is the spin component of the system λ_z is the parameter proportional to the magnetic field. The total Hamiltonian is given by

$$H_{total} = H_{SSH} + H_Z \quad (2.13)$$

$$\begin{bmatrix} -\mu + V_Z & V_1 + V_2(e^{-ik}) & 0 & 0 \\ V_1 + V_2(e^{ik}) & -\mu + V_Z & 0 & 0 \\ 0 & 0 & -\mu - V_Z & V_1 + V_2(e^{-ik}) \\ 0 & 0 & V_1 + V_2(e^{ik}) & -\mu - V_Z \end{bmatrix} \quad (2.14)$$

This matrix represents the magnetic field on the nanoribbon in the space of wave vectors k , now we can diagonalize it and obtain its self-energies. From the Hamiltonian, we can derive the eigenenergies analytically:

$$E_1 = \lambda_z - \mu - \sqrt{(V_1 + V_2 e^{ik})(V_1 e^{ik} + V_2)} e^{ik} e^{-ik} \quad (2.15)$$

$$E_2 = \lambda_z - \mu + \sqrt{(V_1 + V_2 e^{ik})(V_1 e^{ik} + V_2)} e^{ik} e^{-ik} \quad (2.16)$$

$$E_3 = -\lambda_z - \mu - \sqrt{(V_1 + V_2 e^{ik})(V_1 e^{ik} + V_2)} e^{ik} e^{-ik} \quad (2.17)$$

$$E_4 = -\lambda_z - \mu + \sqrt{(V_1 + V_2 e^{ik})(V_1 e^{ik} + V_2)} e^{ik} e^{-ik} \quad (2.18)$$

In this first figure (2.16), we show how the magnetic field affects the SSH energy spectrum. In figure (2.16) a) for $N=40$, we can observe that without the presence of a magnetic field, there are zero-energy modes, as previously observed, which contain topologically protected end states between $V_1 = -1$ and $V_1 = 1$. With the application of a small magnetic field in Figure 2.16 b), the spin degeneracy is broken, and we now have two energy states near zero energy, separated by twice the magnetic field parameter. In the case with the application of a field $\lambda_z = 0.05t$, we have states that are no longer at zero energy and have been shifted by $\lambda_z = 0.05t$. Thus as

can be seen from the spin texture color (in the figure (2.16) shown we have the spin up with the color red and the spin down with the color blue, we will continue with these guidelines until the end of the thesis), these states are all polarized with spin-up. Conversely, we can see that the same effect occurs for spin-down states, but these states are shifted downwards. Therefore, the displacement between the two bands is $2\lambda_z$. We observe in Figures 2.16 c) and 2.16 d) that increasing the magnetic field also increases the separation, keeping the effect consistent. It is important to note that if the applied field were is reverse, the result wall be the opposite, meaning that energies for spin-down would shift upwards, and spin-up would shift downwards.

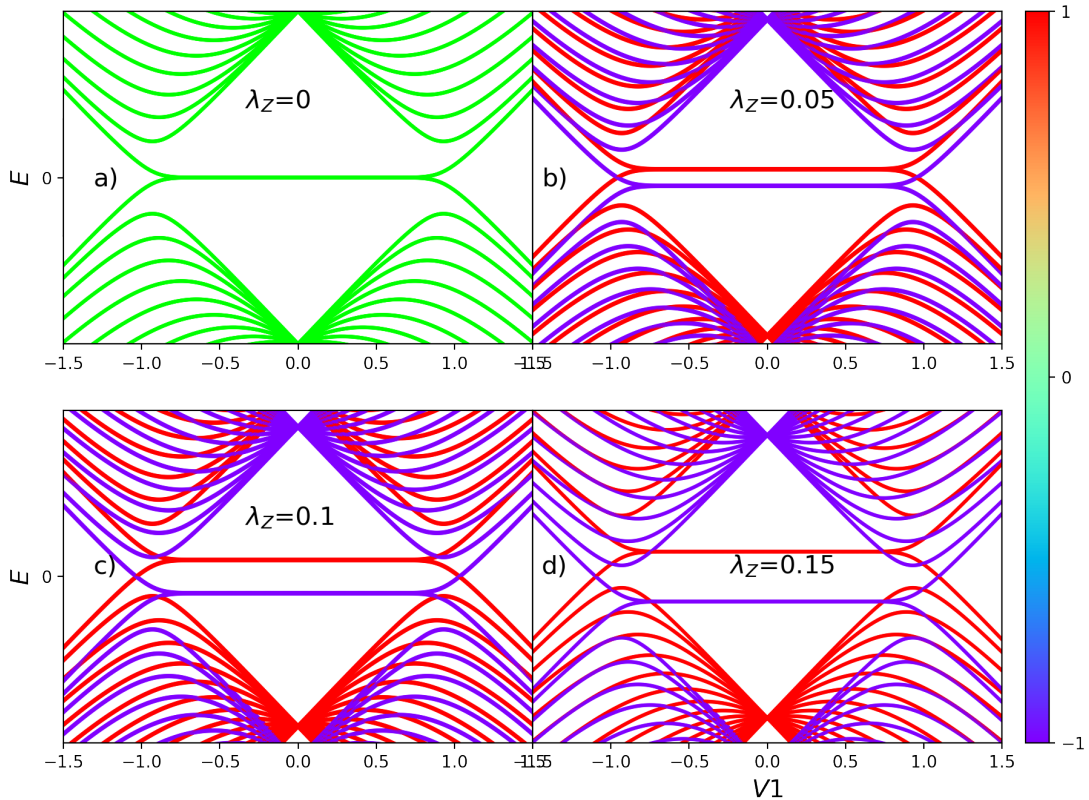


Figure 2.16: Fig of the Energy band spectra about the influence of the external magnetic field on the SSH model where $\lambda_z = 0.0, 0.05t, 0.1t, 0.15t$. the color bar is the spin orientation where spin up is 1 and spin down is -1

In Fig Fig.(2.17), we display several plots illustrating the behaviors of the SSH chain under the influence of parameters V_1 and λ_z . In the graphs of Fig Fig. 2.17, we have the bulk figures from Fig. (2.17) a) to Fig. (2.17) e), which represent the Fourier transform of the Hamiltonian for different values of $V_1 = 0.5t, 0.5t, 1t, 0.5t, 1t$. In the second level, we have finite energy spectrum figures for the system. Specifically, we have Fig. a) for the chemical potential $\mu = 0t$,

Fig.(2.17) g) for $\mu = 0.1t$, and Fig.(2.17) h) for $\mu = -0.1t$. In the third level, Fig.(2.17) i) to Fig. (2.17) m) shows the energy spectra for specific values of V_1 . Finally, Fig.(2.17) n) to Fig.(2.17) r) display the wave functions for the finite system for each value of V_1 .

From graphs (f) to (g), we have the finite case with a variation in hopping V_1 . Figures (2.17) (i) to (m) represent auto energies organized in ascending order. Finally, Fig. (2.17) from (n) to (r) are the wave functions.

Now, in Fig. 2.17, we examine of how the SSH chain behaves for a specific field $\lambda_z = 0.1t$. We can see in Fig 2.17 the bulk (infinite case) from (a) to (e), where in Fig (a), there is a gap. The value of V_1 is indicated by a gray vertical line in graph (f), which corresponds to the region covered by the energy graph (i) and the wave function in figure (n). Now, let us conduct a brief analysis of the graphs.

In Fig. 2.17 (a), there is a gap, but no specific indications can be made. However, when we look at Fig. 2.17 (f), as explained earlier, with the application of a magnetic field, there are no longer zero modes because they have shifted in value up and down. Therefore, the energies are no longer accessible in the system because of the parameters. Continuing the discussion, in Fig. (i), we can observe that there are now two up modes shifted upwards and two down modes shifted downwards. In Fig. n), we can see that the wave function is not localized. Thus, we conclude that for these parameters, we do not obtain any topological states as there are no localized wave functions or zero-energy modes.

Now, continuing the analysis, let's move to Fig. (b), where, in addition to the previous elements, we add a chemical potential of the order of the field $\mu = \lambda_z = 0.1t$. However, we observe that in the bulk, nothing has changed for the same value of V_1 . Now, moving to Fig. (g), we can see a difference where the energy modes are now zero for spin-up. Therefore, the leftmost vertical line in the region of zero energies is now inside. This can be confirmed in the energies of this system in Fig. (j), where there are now two zero-energy modes with spin projection along the z-axis up. Finally, we can observe the localized wave functions in Fig. (o). Therefore, here we are in a topological region.

As complementary figures, we have Fig. c), which represents a topological transition region where the gap closes for the red bands at $k = \pi$, indicating a metallic region. The value of $V_1 = 1t$ from the second gray vertical line in Fig. g) is observed here. In Fig. k), we can see that there are no more zero-energy levels and a more continuous energy spectrum where the energy levels are continuous, and the wave function in Fig. p) is not localized at the edges.

Analyzing the problem further, we move on to Fig. d), where the chemical potential is

of the opposite order to the field, $\mu = -\lambda_z = -0.1t$. However, we observe that in the bulk, nothing has changed for the same value of V_1 . Now, moving to Fig. h), we can see a difference where the energy modes are now zero for spin-down. Therefore, the leftmost vertical line in the region of zero energies is now inside. This can be confirmed in the energies of this system in Fig. j), where there are now two zero-energy modes with spin projection along the z-axis down. Finally, we can observe the localized wave functions in Fig. o), which have colors compatible with spin-down. Therefore, here we are in a topological region but with opposite spin.

We have Fig. (e), which represents a topological transition region where the gap closes for the blue bands at $k = \pi$, indicating a metallic region. The value of $V_1 = 1t$ from the second gray vertical line in Fig. h) is observed here. In Fig. m), we can see that there are no more zero-energy levels and a more continuous energy spectrum where the energy levels are continuous, and the wave function in Fig. p) is not localized at the edges.

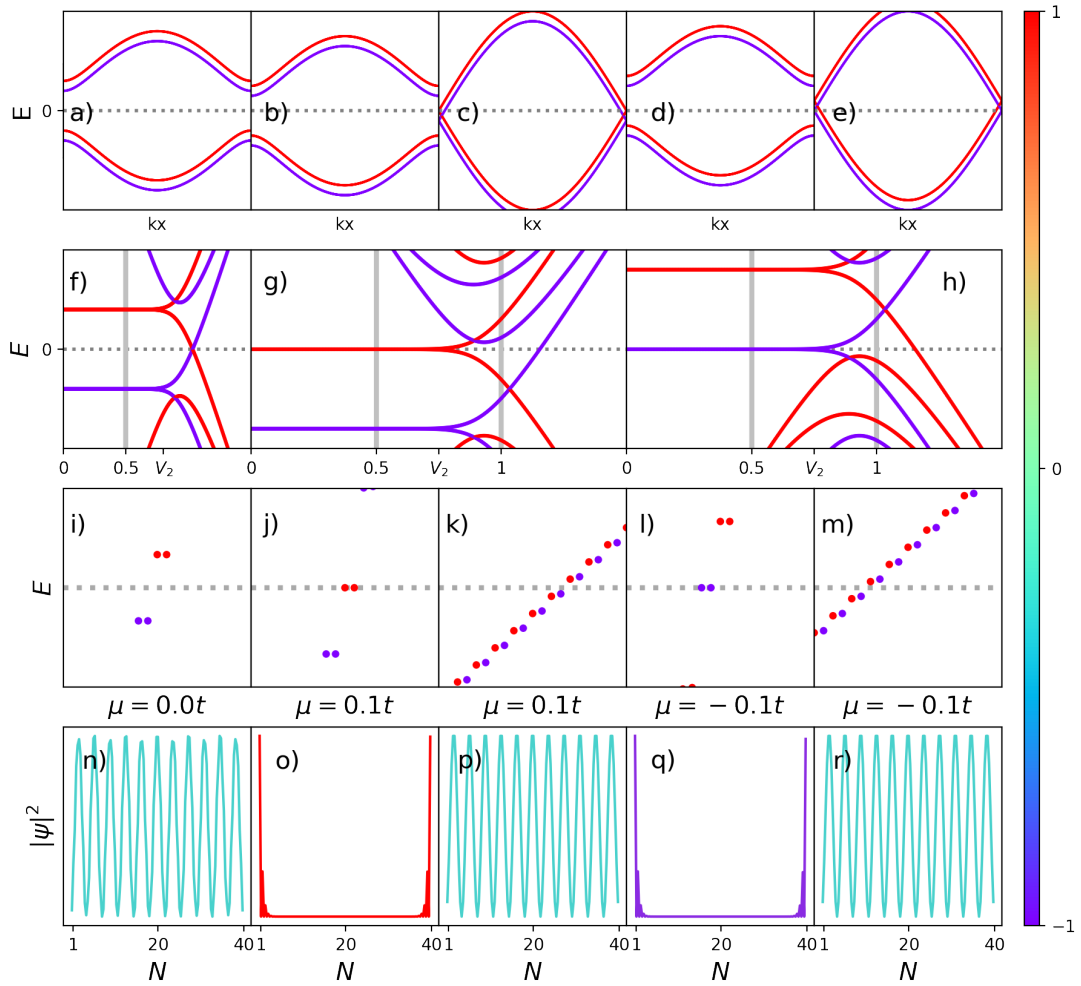


Figure 2.17: Representation of the SSH chain behaviors influenced by parameters V_1 , μ , and $\lambda_z=0.1$. The Figures a), b), c), d) and e) show the bulk plots for the infinite case, the plots f) is the energy spectra for specific values of V_2 and $V_1 = 1t$ and the plots g), h) is finite energy spectra influenced by chemical potentials with values $0.1t$ and -0.1 respectively, and the plots i), j), k), l), m) are the plots where we have specific values of V_2 shown in highlights in the graph above in gray and the plots n), o), p), q) and r) are the wave functions for the finite system of the cases above.

Through our comprehensive analysis of the SSH chain, particularly when considering the inclusion of the spin component λ_z , several significant findings. The SSH chain demonstrates a clear sensitivity to parameter variations, across a spectrum of scenarios, encompassing both infinite and finite settings. Furthermore, the chain behavior, especially under the influence of changing chemical components, contributes valuable insights to our comprehension of the system.

The visual representations in the figures (2.16) -(2.17) provide an exploration of the SSH chain characteristics, encompassing energy spectra and wave functions. the introduction of the spin component λ_z introduces an additional complexity to our investigation. The importance of considering spin when analyzing the system. It is worth noting that even with the addition of the magnetic effect in this chain, we still do not have Majorana fermions here because we do not have any coupling effects between electrons and holes, such as a superconducting type p which is a main ingredient.

In short, this exploration of the SSH chain, with the spin component λ_z , we can see new behaviors of the system resulting in new phenomena of the SSH chain with magnetic field apply.

2.5 Rice-Mele Model with spin

Now let us apply the external magnetic field to the Rice-mele model (RM) chain, we applied the same approach used in the previous section, where we introduced the Zeeman effect into the RM Hamiltonian, as described in Eq. 2.19, and its matrix form in the reciprocal space of wave vectors k is given in Eq. (2.20), and the eigenenergies accessible by the system are given by Eq. (2.21).

$$\begin{aligned} \mathcal{H}_{RM} = & -V_1 \sum_n c_{A,n}^\dagger c_{B,n} - V_2 \sum_n c_{A,n+1}^\dagger c_{B,n} + \\ & (\epsilon_A - \mu) \sum_n c_{A,n}^\dagger c_{A,n} + (\epsilon_B - \mu) \sum_n c_{B,n}^\dagger c_{B,n} + H.c., \end{aligned} \quad (2.19)$$

$$\begin{bmatrix} \lambda_z + \epsilon - \mu & V_1 + V_2 e^{ik} & 0 & 0 \\ V_1 + V_2 e^{-ik} & \lambda_z - \epsilon - \mu & 0 & 0 \\ 0 & 0 & -\lambda_z + \epsilon - \mu & V_1 + V_2 e^{ik} \\ 0 & 0 & V_1 + V_2 e^{-ik} & -\lambda_z - \epsilon - \mu \end{bmatrix} \quad (2.20)$$

Now we can put it in matrix form where we can identify a matrix with two blocks, one up and one down and we can diagonalize it using sympy analytically

$$E_1(k) = \lambda_z - \mu - e^{-ik}\sqrt{\Delta} \quad (2.21)$$

$$E_2(k) = \lambda_z - \mu + e^{-ik}\sqrt{\Delta} \quad (2.22)$$

$$E_3(k) = -\lambda_z - \mu - e^{-ik}\sqrt{\Delta} \quad (2.23)$$

$$E_4(k) = -\lambda_z - \mu + e^{-ik}\sqrt{\Delta}. \quad (2.24)$$

$$\Delta = \left(V_1^2 e^{ik} + V_1 V_2 e^{2ik} + V_1 V_2 + V_2^2 e^{ik} + \varepsilon^2 e^{ik} \right) e^{ik}. \quad (2.25)$$

Now we used a Python program to numerically calculate the energy states accessible by the system for specific parameters. In the same manner as we did previously, we will begin by analyzing the energy spectrum for a finite system of 40 atoms.

In Fig 2.18, we can observe four different plots. In Fig. 2.18 a), we have the pure SSH case, as the parameters ε and λ_z are both zero. Even though they are added to the Hamiltonian, we obtain the same results as before. It is worth noting that all energy spectrum graphs are plotted a function of V_2 on the horizontal axis. Moving on to Fig. 2.18 b), it's the RM model with the parameter $\varepsilon = 0.1t$, but with $\lambda_z = 0$. In this case, we can compare the two graphs and notice that we no longer have zero-energy modes, and there is a gap region of 2ε between the energy levels in the energy spectrum.

In Fig. 2.18 c), now with $\lambda_z = 0.05t$, we have a similar effect to the SSH case, but now each energy plateau has experienced a degeneracy breaking due to the magnetic field. We now have regions of allowed energies only for spin-up and only for spin-down, and each energy plateau has undergone this splitting, resulting in four energy plateaus, two for spin-up and two for spin-down. In Fig. 2.18 d), we analyze a specific set of parameters where $\varepsilon = \lambda_z$. In this scenario, the energy that suffered the symmetry breaking, which had higher energy than the chemical potential, now overlaps with the accessible energies for spin-down exactly on top of the energies accessible for spin-up from the symmetry-breaking in the lower energy levels. Consequently, we now have a region of zero-mode energies where both spin-up and spin-down states, and they are no longer degenerate.

Now that we have systems with this profile described in Fig. 2.18 d), let us delve deeper into Fig 2.19, where we will analyze the generated figures, ranging from bulk energies to wave functions.

In Fig. 2.19, we have defined the parameters as $V_1 = 1$, $\lambda_z = 0.1t$, and ε with two values,

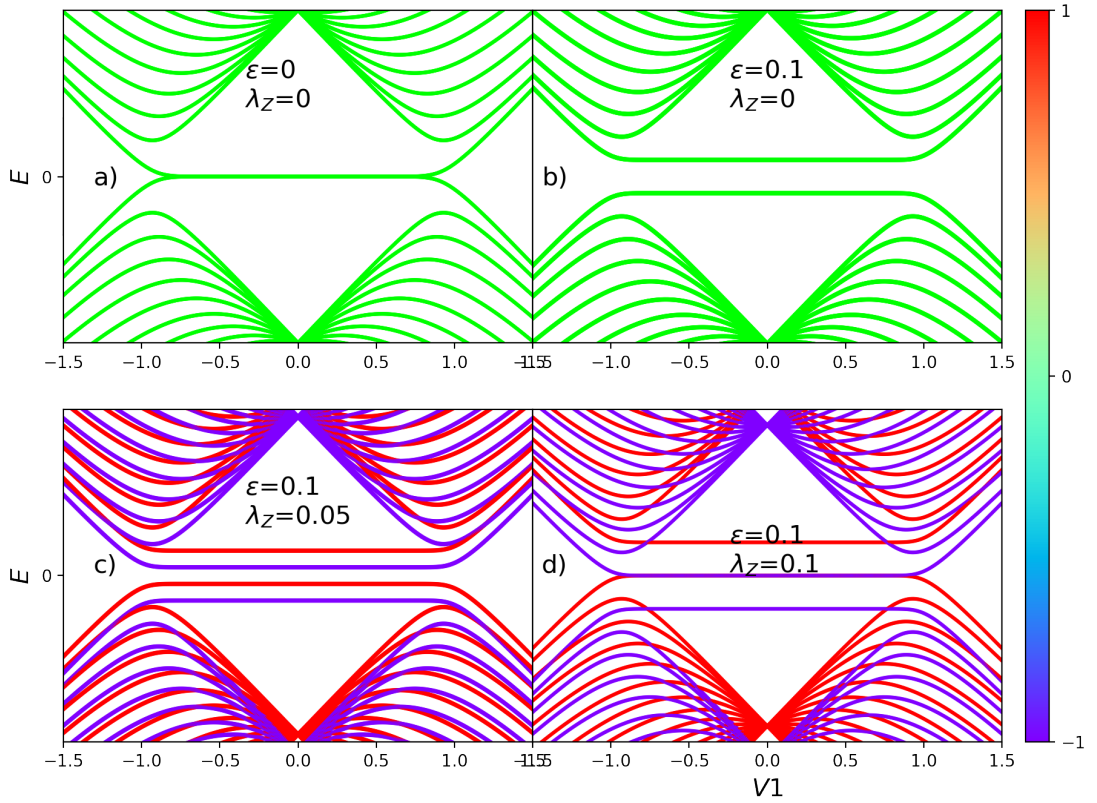


Figure 2.18: Comparative energy spectra for the Rice-Mele model with varying parameters and applied magnetic field. Fig a) represents the pure SSH case, where ε and λ_z parameters are nullified. Fig b) depicts the RM model behavior with an introduced ε . Fig c) displays the response to a magnetic field λ_z in the system, emphasizing the broken degeneracy. Fig d) gives an overview of specific parameter combinations, highlighting the effects of symmetry breaking and energy accessibility for different spin orientations. In the color bar we have values that can vary from 1 to -1 where 1 would be spin up and -1 spin down.

± 1 . From Fig.2.19 a) to d), we see the energy dispersions of the system. Essentially, we are examining the allowed energies in the wave vector k space. This system might be referred to as "infinite" or "bulk" since translational symmetry exists along the x-axis. In Fig.2.19 e) and f), we present the energy spectrum for a finite system, implying it lacks translational symmetry, across various V_1 values. This means we are looking at multiple distinct systems. Notably, both systems maintain zero-state energies up to $V_1 = 1$. In Fig.2.19 g) to j), we have the energy spectrum for certain curves highlighted in light gray in the preceding figures (2.19). For instance, Fig.2.19 g) corresponds to the value $V_1 = 0.5t$. Lastly, Fig.2.19 k) to n) show wave functions of the zero energies from the figures above them, be they continuous spectra or those without zero energies. We will select a random wave function mode from all possible modes to analyze

further.

In Fig.2.19 a), we observe an energy dispersion with a gap. This figure corresponds to $V_1 = 0.5t$, as indicated by the vertical gray line in Fig. 2.19 e) - the energy spectrum for this system. Here, we can see two zero states, each with a defined spin direction: one upwards and the other downwards. In Fig.2.19 k), the two wave functions plotted for each energy level are discerned; blue represents the energy with spin down and red indicates the energy with spin up. With these parameters in this system, we have spin-polarized ends, with each tip having an edge state opposite to the other, thereby constituting a topologically protected state.

Continuing the discussion with Fig.2.19 b), we witness a phase transition where $V_1 = 1$. We can observe that the second line of Fig.2.19 e) aligns with this value, indicating closed bands, which suggests a metallic state. Further, in Fig.2.19 h), the energy spectrum now appears continuous, meaning there are no zero modes, and its wave function in Fig.2.19 l) is not localized.

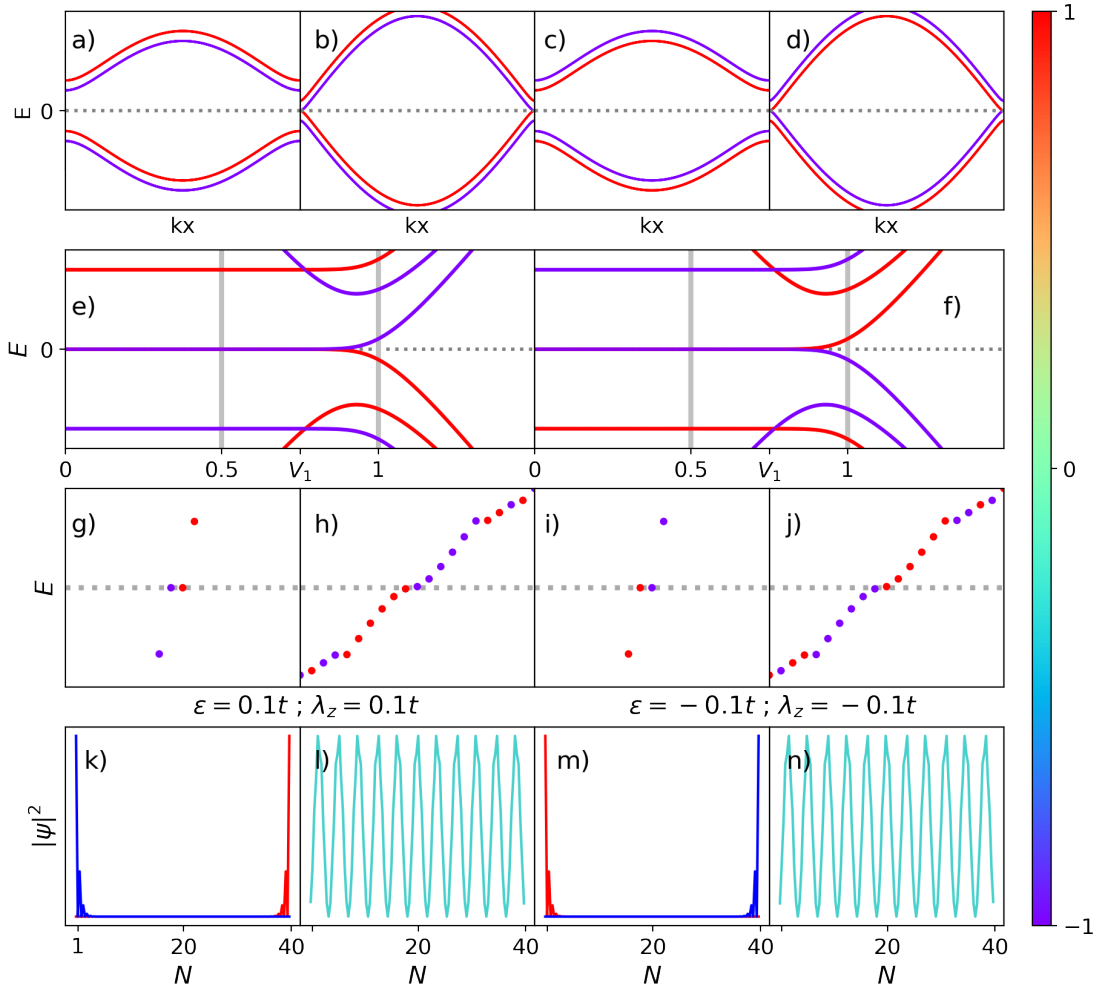


Figure 2.19: Energy dispersions and wave functions of the spin-polarized Rice-Mele model under various parameters. Figs a) to d) depict the energy dispersions for an infinite (bulk) system, with a focus on permitted energies in the wave vector space k . Figs e) to j) illustrate the energy spectrum for finite systems with varied V_1 values. Figs k) to n) showcase the localized wave functions corresponding to zero-energy modes or other selected modes based on the energy spectra above.

In Fig.2.19 c), we have the parameters $\lambda_z = \varepsilon = -0.1t$. This represents the inverse situation of Fig.2.19 a). In this case, the bands are inverted from a spin perspective. This inversion can also be observed in Fig.2.19 f), where previously, the blue energies that were pointing upwards have been replaced by up energy states. In Fig.2.19 i), we notice that the energies remain at zero but are inverted. Moving to Fig.2.19 m), the wave functions localized at the boundaries now appear to be the inverse of what is shown in Fig.2.19 k). With these parameters, we can discern that the system is inverted from the standpoint of spin in this topologically protected system.

Lastly, this inversion is also evident in Fig.2.19 d), where Fig.2.19 j) is the inverse of Fig.2.19 h). However, the energy spectrum remains continuous, and as a result, the wave function is not localized as seen in Fig.2.19 n).

From our observations, it is evident that by applying an external magnetic field, we can achieve zero-energy modes without the need for a chemical potential. Moreover, we can obtain polarized spin modes on different edges of the nanowire for the RM chain. Furthermore, we can determine the spin on each side using the magnetic field and the energy of the sites, it is worth mentioning that this result is the first original result of this thesis, this work has yet to be written.

2.6 Kitaev chain

Starting from the seminal work of Read and Green (28) on two-dimensional p -wave superconductors, Kitaev proposed a simplified one-dimensional (1D) toy model (3). In this model, unpaired Majorana zero modes (MZMs) appear at opposite ends of a p -wave superconducting tight-binding chain. Remarkably, it took less than a decade (7) to understand that it could experimentally realize Kitaev original proposal. Some setups (8–10) employed hybrid devices composed of a 1D semiconductor nanowire with strong Rashba spin-orbit coupling (RSOC), in contact with a conventional s -wave superconductor and under an external magnetic field (EMF) longitudinal to the nanowire. Topological protected MZMs emerge at the nanowire ends (11) when the nanowire chemical potential lies on the bulk p -wave superconducting induced-gap.

In the study of condensed matter physics, Majorana modes are notable as they behave as both particles and their own anti-particles(29). These modes are commonly explored in superconducting systems because of a characteristic known as particle-hole symmetry (PHS). You can find them on the surfaces of p -wave superconductors, especially when their wave function has a spin of $p = 1$ (triplet state). This tells us that Cooper pairs formed from electrons in a specific state (30).

This brings us to the Kitaev model, a concept based on depositing iron atoms onto a superconducting lead surface (31). At its core, the model revolves around three main components:

1. The natural interactions, known as spin-orbit and Rashba interactions, seen in a system like a zigzag nanoribbon.
2. An external magnetic field that helps set the spin direction in the nanowire and fine-tune the size of the gap between them.

3. Using an "s" superconductor as a base for the nanowires, promoting the formation of a "p" type pairing due to their close proximity.

In simpler terms, the Kitaev model describes a chain of spinless particles that support p -wave superconductivity. Here the Kitaev model is interpreted as spinless, but in reality it would already be spinpolarized with only one type of spin, for example the chain would be completely spin polarized with spin up or down.

While Kitaev initial research did not search into spin, later studies have. For instance, Jeon's team(14) used advanced tools to differentiate between Majorana modes and other states in iron atom chains. There are also additional spin-focused studies that search into unique effects and behaviors in specific setups(32–34).

The Kitaev chain is a one-dimensional theoretical model spinless of spinless fermions, that helps us understand the properties of Majorana-bound states. the Hamiltonian for the Kitaev chain, is:

$$H = -\mu \sum_n^N c_n^\dagger c_n - t \sum_n^{N-1} (c_{n+1}^\dagger c_n + h.c.) + \Delta e^{i\phi} \sum_n^{N-1} (c_n c_{n+1} + h.c.), \quad (2.26)$$

where c_n^\dagger and c_n respectively create and destroy an electron at position n . t refers to the electron "hop" from one position to another. μ is the chemical potential, indicating the energy difference from the ground state. Δ and ϕ are related to a special kind of electron pairing, p -wave pairing, and its phase.

It is worth noting that this Hamiltonian does not consider both electron spins, which means it is not symmetric under time reversal, summetry terms transformation

To determine the energy spectrum and eigenstates for any set of parameters, we can express the problem in matrix form. We first use the fermionic anticommutation relations

$$\{c_x, c_{x'}^\dagger\} = \delta_{x,x'} \quad \text{and} \quad \{c_x, c_{x'}\} = \{c_x^\dagger, c_{x'}^\dagger\} = 0, \quad (2.27)$$

This allows us to represent the Hamiltonian in a more simmetric form

$$\begin{aligned}
H = & -\mu \sum_n^N (c_n^\dagger c_n - \frac{1}{2}) - \frac{t}{4} \sum_n^{N-1} (c_{n+1}^\dagger c_n - c_{n+1} c_n^\dagger) \\
& + \frac{\Delta e^{i\phi}}{4} \sum_n^{N-1} (c_n c_{n+1} - c_{n+1} c_n) + h.c.).
\end{aligned} \tag{2.28}$$

For a more concise representation, we use a column vector of fermion operators

$$\Psi \equiv \left(c_1, c_1^\dagger, c_2, c_2^\dagger, \dots, c_n, c_n^\dagger \right)^T, \tag{2.29}$$

Resulting in

$$H = \Psi^\dagger \mathcal{M} \Psi. \tag{2.30}$$

where \mathcal{M} is given by

$$\mathcal{M} = \begin{pmatrix} -\mu & 0 & -t & \Delta e^{-i\phi} & \dots & 0 & 0 & 0 \\ 0 & \mu & -\Delta e^{i\phi} & t & \dots & 0 & 0 & 0 \\ -t & -\Delta e^{-i\phi} & -\mu & 0 & \dots & 0 & 0 & 0 \\ \Delta e^{i\phi} & t & 0 & \mu & \dots & 0 & 0 & 0 \\ \vdots & & & & & & & \\ 0 & 0 & 0 & \dots & -\mu & 0 & -t & \Delta e^{-i\phi} \\ 0 & 0 & 0 & \dots & 0 & \mu & -\Delta e^{i\phi} & t \\ 0 & 0 & 0 & \dots & -t & -\Delta e^{-i\phi} & -\mu & 0 \\ 0 & 0 & 0 & \dots & \Delta e^{i\phi} & t & 0 & \mu \end{pmatrix}, \tag{2.31}$$

By diagonalizing matrix 2.31, we can obtain the energy spectrum as a function of the chemical potential, μ .

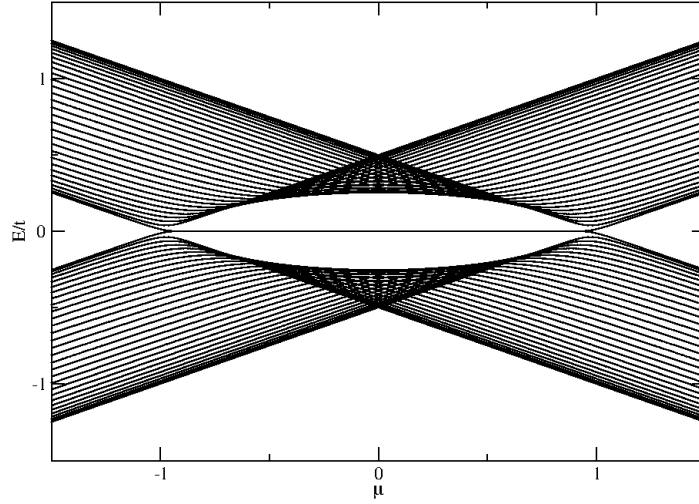


Figura 2.20: Finite Kitaev chain for $N = 30$.

Fig. 2.20 shows the energy spectrum for a 30-site Kitaev chain, where the zero energy modes appear at $\mu/t < 1.0$, being a signature of the emergence of Majorana fermions. Another feature we can notice is the particle-hole symmetry which comes from the construction of the Hamiltonian displayed in the system on the vertical axis in relation to the chemical potential $\mu = 0.0$ energy.

Now we consider the Born-von Karman boundary condition, to study the bulk properties of the chain. The Fourier transform the creation and annihilation operators,

$$c_n = \frac{1}{\sqrt{2\pi}} \sum_k e^{ikx_n} c_k ; c_n^\dagger = \frac{1}{\sqrt{2\pi}} \sum_k e^{-ikx_n} c_k, \quad (2.32)$$

in which $x_n = na$, and $a = 1$ is the lattice constant, we can rewrite the Hamiltonian 2.26 in terms of the wave vectors, in momentum space

$$H = \frac{1}{2} \sum_k \left((-\mu - t\cos(k)) c_k^\dagger c_k + (\mu + t\cos(k)) c_{-k}^\dagger c_{-k} - i\Delta \sin(k) c_{-k} c_k \right) + h.c. \quad (2.33)$$

Using the matrix representation:

$$H = \begin{pmatrix} c_{-k}^\dagger & c_k \end{pmatrix} \begin{pmatrix} -\mu - t\cos(k) & i\Delta \sin(k) \\ -i\Delta \sin(k) & \mu + t\cos(k) \end{pmatrix} \begin{pmatrix} c_{-k} \\ c_k^\dagger \end{pmatrix}. \quad (2.34)$$

To better characterize Majorana fermions, we can rewrite the Hamiltonian (2.26) in forms of MF operators, that must follow the properties of these quasi-particles:

$$\gamma^\dagger = \gamma \text{ and } \gamma^2 = 1, \quad (2.35)$$

where γ operator. We can write the fermionic operators in terms of usual Majorana operators as follows:

$$\begin{aligned} c_n^\dagger &= \frac{(\gamma_{2n-1} - i\gamma_{2n})}{2}, \\ c_n &= \frac{(\gamma_{2n-1} + i\gamma_{2n})}{2}, \end{aligned} \quad (2.36)$$

and from the relation above we have

$$\begin{aligned} \gamma_{2n} &= i(c_n^\dagger - c_n), \\ \gamma_{2n-1} &= c_n^\dagger + c_n. \end{aligned} \quad (2.37)$$

Considering the model consisting of a one-dimensional chain of N sites, each capable of carrying a fermionic state $c_n^\dagger|\Psi\rangle$, or equivalently, two modes of Majorana γ_{2n-1} and γ_{2n} , as shown in the Fig. (2.21).

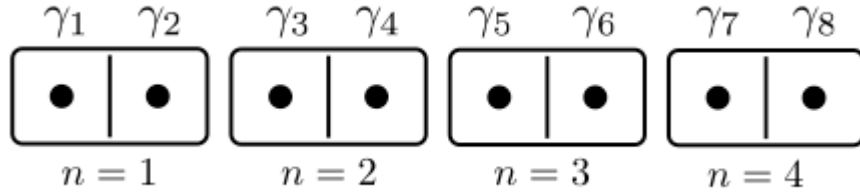


Figura 2.21: Representation of the Kitaev chain.

In terms of Majorana operators the Hamiltonian (2.26) reads

$$H = -\frac{\mu}{2} \sum_{n=1}^N (1 + i\gamma_{2n-1}\gamma_{2n}) - \frac{i}{4} \sum_{n=1}^{N-1} [(\Delta + t)\gamma_{2n}\gamma_{2n+1} + (\Delta - t)\gamma_{2n}\gamma_{2n+1}]. \quad (2.38)$$

We can analyze this Hamiltonian in two limit cases. The first one corresponds to $\mu < 0$ but $t = \Delta = 0$, which we can interpret as a pairing between Majoranas γ_{2n-1} and γ_{2n} at the same lattice site, as we can see in Fig. (2.22)

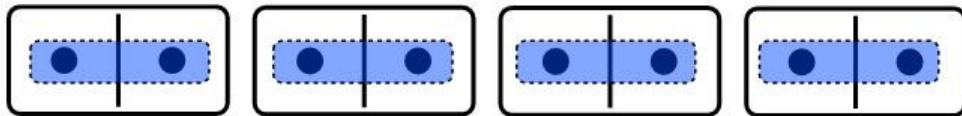


Figura 2.22: No unpaired Majoranas.

The Hamiltonian 2.38 reduces to

$$H = -\frac{\mu}{2} \sum_{n=1}^N (1 + i\gamma_{2n-1}\gamma_{2n}), \quad (2.39)$$

where the spectrum of the system presents a gap, since it costs a finite energy $|\mu|$ to add a spinless electron to the chain. These conclusions are still valid even away from this fine-tuned condition as long as the gap persists, the chain remains in the trivial phase, and this case are called topologically trivial phase.

The second case is more complex and interesting, which $t = \Delta \neq 0$ and $\mu = 0$ this case is called topological phase (non-trivial). The Hamiltonian (2.38) is now given by

$$H = -i\frac{t}{2} \sum_{n=1}^{N-1} (\gamma_{2n}\gamma_{2n+1}), \quad (2.40)$$

which corresponds to pairing Majoranas at adjacent sites, as indicated in the Fig.2.23

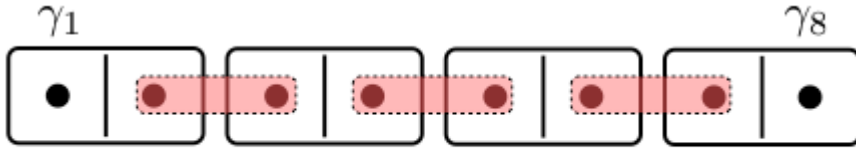


Figura 2.23: Unpaired Majoranas states.

Observe that the first and last modes do not participate in the Hamiltonian, this chain has two states with zero energy located at its edges. We then have a one-dimensional system with a bulk gap and zero energy states at the edges in the topological phase for $\frac{|\mu|}{t} < 1$

Capítulo 3

DOUBLE ZIGZAG HONEYCOMB NANORIBBONS

3.1 Introduction

As discussed in the previous chapter, we now have a solid foundation to develop a theoretical model of a nanoribbon. Let's begin constructing this model by considering a honeycomb-type nanoribbon with zigzag terminations. In this initial stage, we will describe the nanoribbon, including the hoppings and superconductivity, but excluding the spin degree of freedom. This model will be similar to the Kitaev model but adapted to our nanoribbon system. After constructing the model, we will proceed to create graphs and evaluate the initial results.

In the second part of the model, we will introduce the spin degree of freedom in a manner similar to what was done in the SSH and Rice-Mele models. Then, we will apply the same methodology to analyze the generated graphs and describe the underlying physics of this more complex system.

Another kind of setup came up after the development of epitaxially grown hybrid semiconductor-superconductor systems in which two or three facets of the hexagonal InAs nanowire core were covered by Al (12). This setup is a hybrid platform that employs a naturally occurring quantum dot (QD) at the end of the nanowire as a spectrometer (35–38) to measure the nonlocality degree and the spin canting angles of the nonlocal MZMs (33, 39). A chain of ferromagnetic atoms aligned over a conventional *s*-wave superconductor with strong RSOC also was considered as a hybrid system supporting the existence of MZMs (13, 14). In this scenario, the essential ingredients to generate MZMs at the ends of the chain are the ferromagnetic interaction between atoms that composes the chain and the RSOC induced on the chain by the superconducting substrate. A helpful review of the experimental state-of-the-art on this subject can be found in Refs. (22, 40).

The manifestation of MZMs in 1D hybrid semiconductor-superconductor nanowires, known as Majorana nanowires, and magnetic chains on top of *s*-wave superconductors are fully unders-

tood from a theoretical point of view (11, 41, 42). Recent studies have been pointing out the need to fabricate cleaner and disorder-free Majorana nanowires with an induced hard superconducting gap (43–45), in which distinct measurements have to be performed to corroborate indeed the existence of topologically protected MZMs (46–48). In this scenario, alternative 2D honeycomb lattice setups offer a prolific and little-explored platform wherein topological Majorana quasiparticle excitations can emerge. Between them, we can indicate two theoretical precursor studies: One proposes the generation of MZMs on quantum wires formed in bilayer graphene by electrostatic confinement(49) and the other studied the formation of MZMs on an armchair nanoribbon in the presence of spatially varying magnetic fields (50). Both systems are put in contact with an *s*-superconductor.

We also draw attention to zigzag honeycomb nanoribbons (zHNRs) built up from Xenes graphene-like family (51–53), where X represents single elements from group III to group VI of the periodic table. Despite the challenges of growing zHNRs of the Xenes family in conventional *s*-wave superconductors (54–56), such a kind of 2D lattice offers an alternative for engineering *p*-wave superconducting pairing required to realize MZMs. Probably, silicene (X=Si) is the most promising candidate of this family for obtaining a zHNR geometry with the ability to host MZMs (57, 58). Its energy spectra (59) can be spin-polarized by applying an external electric field perpendicular to the zHNR sheet plane (60–62), giving rise to an effective extrinsic RSOC that breaks its mirror symmetry [see Eq. (3.18)]. Silicene also presents an excellent potential to produce half-metallic transport and pure spin-current (63–65).

Another possibility discussed in section 3.5 to realize *p*-wave superconductivity to produce a Kitaev chain is related to the property of zHNRs from Xenes materials to exhibit ferromagnetic ordering at their edges (66) due to internal repulsive Coulombic interactions (53). Thus, this inborn spin alignment at the zHNR edges can be employed to induce the superconducting pairing with *p*-wave symmetry when the zHNRs are put in proximity with a *s*-wave superconductor. This procedure is similar to previous studies with ferromagnetic chains from Yazdani’s group (13, 14), but we do not theoretically implement it in this work.

Despite the spinless nature of Kitaev work, some proposals have explored the spin properties of MZMs in different contexts. Jeon et al. (14), employed a spin-polarized STM for distinguishing between topological MZMs and other trivial in-gap states in chains of Fe atoms deposited on top of superconducting Pb. Spin-polarization of MZMs was also accounted to investigate the Kondo effect in a QD coupled to a metallic contact and a pair of MZMs (32), and to study the transport properties of a finite-length Majorana nanowire placed between a dot and a metallic lead (33, 34).

Since the theoretical work by Fu and Kane that MZMs was predicted to be present inside a core of vortex topological superconductors (67) and the possibility of spin-polarized them was pointed out in reference (68). Its experimental detection was realized in a topological insulator-superconductor $\text{Bi}_2\text{Te}_3/\text{NbSe}_2$ heterostructure(69). The spin polarization of those core states can be probed by measuring the local polarized density of states (LDOS) employing scanning tunneling microscopy and spectroscopy (STM/STS) via excitations in the vortex state (70, 71). Moreover, the MZMs was also employed as an alternative way of performing quantum computing operations (72–74), allowing the transference of spin qubits QDs and unpolarized MZMs, and also realizing nontrivial two-qubit gates. As proposed in this work, the discrimination of the spin degrees of freedom of the MZMs in topological superconductor vortices or zigzag nanoribbons can contribute to building topological quantum gates employing the spins of both MZMs and QDs simultaneously.

In this work, we report the possibility of spin discriminating MZMs in zHNRs geometry [Fig. 3.1(a)], which we refer to as double-spin Kitaev zigzag honeycomb nanoribbons (KzHNR). This double nanoribbon structure mimics two parallel Kitaev chains connected by the hopping t , as indicated in Fig. 3.1(c). Our findings reveal that we can access the spin species of the MZMs in a double spin KzHNR by tuning the chemical potential of the chains, which is not feasible in standard 1D Majorana nanowires. In this scenario, we suggest an experimental proposal to discriminate spin-polarized MZMs in zHNRs structures of silicene grown over a Pb superconductor in the presence of RSOC and an EMF. Our findings could contribute to paving the way for studying hybrid topological-conventional polarized QD qubits using Majorana spintronics.

3.2 Spinless model and topological phase transitions

We first consider a double-spinless KzHNR as a generalization of the Kitaev chain (3) to characterize the topological phase transitions (TPT) of the system through corresponding winding numbers (75), computed for the infinite case. By considering a tight-binding chain in a zHNR geometry, we define a spinless phenomenological model as a Kitaev ladder-type (76). We represent in Fig. 3.1(c), the first nearest neighbor (NN) hopping t between nonequivalent sites A and B and the p -wave superconducting pairing, indicated by arrows, between equivalent sites A or B located at the edges of the KzHNR. The Hamiltonian describing such a model reads

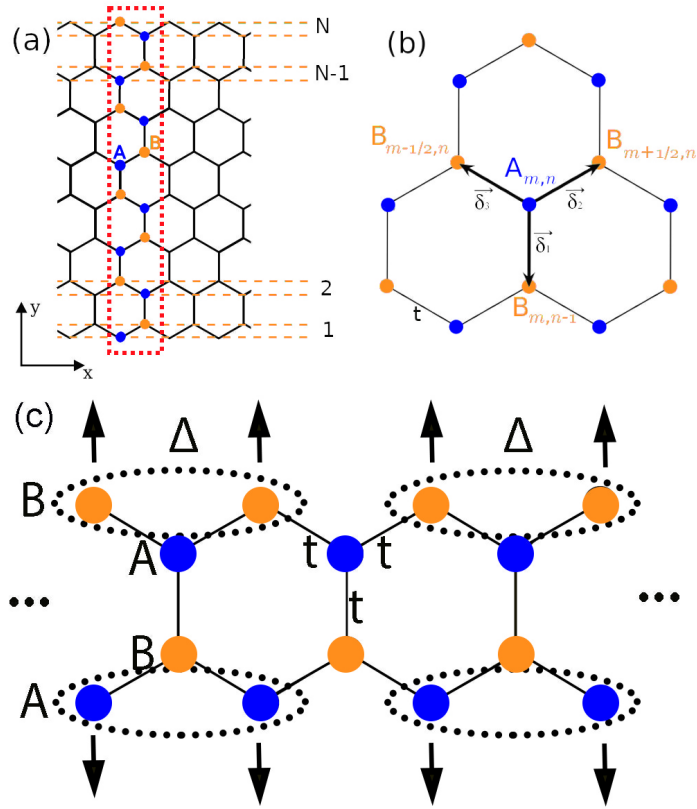


Figure 3.1: (a) Sketch of the 2D zHNR geometry adopted here, where N represents its width ($n = 1, \dots, N$). The region within the red dashed area composed of $2N$ nonequivalent A (blue) and B (orange) sites along the y direction represents the unit cell employed in the numerical simulations. The M number of unit cells defines the nanoribbon length ($m = 1, \dots, M$). (b) Representation of the nearest-neighbor hopping t , which is adopted as the energy unit. (c) Schematic of a double-spin KzHNR of width $N = 2$. The equivalent B (A) atoms of the upper (lower) KzHNR are paired with each other via a p -wave superconducting parameter Δ .

$$H = H_t + H_\Delta, \quad (3.1)$$

where,

$$H_t = \sum_{m,n} [t(a_{m,n}^\dagger b_{m,n-1} + a_{m,n}^\dagger b_{m-1/2,n} + a_{m,n}^\dagger b_{m+1/2,n}) - \sum_n \mu [a_{n,n}^\dagger a_{n,n} + b_{n,n}^\dagger b_{n,n}] + \text{H.c.}], \quad (3.2)$$

corresponds to the NN hopping term t , as indicated in Fig. 3.1(b), where, μ is the chemical potential and the operators $a_{m,n}^\dagger/b_{m,n}$ creates/annihilates an electron at site A/B of the unit cell.

Moreover, the Hamiltonian

$$H_{\Delta} = \sum_{m,n} \Delta [a_{m,n}^{\dagger} a_{m+1,n}^{\dagger} - a_{m,n}^{\dagger} a_{m-1,n}^{\dagger} + b_{m,n+1}^{\dagger} b_{m+1,n+1}^{\dagger} - b_{m,n+1}^{\dagger} b_{m-1,n+1}^{\dagger} + \text{H.c.}], \quad (3.3)$$

describes the p -wave superconducting pairing of the double-spinless KzHNR, where Δ is the pairing strength between sites B in the top and between sites A in the bottom of each KzHNR, as indicated in Fig. 3.1(c). Once particle-hole, time-reversal, and chiral symmetries are preserved by the Hamiltonian [Eqs. (3.1)-(3.3)], it belongs to the BDI symmetry group class with \mathbb{Z} index (77, 78).

3.3 Phase Transition Calculation in the Spinless Case

We will consider the infinite double KzHNR case. We are interested in calculating the winding numbers, the band structure, and the topological phase transitions exhibited by the system. In the main text of the work, we use this information as guidelines to interpret the emergence of MZMs in the finite case. By considering the Fourier transform of Eqs. 3.2 and 3.3, the total Hamiltonian can be written as

$$H = H_t + H_{\Delta}, \quad (3.4)$$

with the first nearest neighbor hopping and the superconductor pairing term. In the momentum representation, the Hamiltonian can be written as

$$H_t = - \sum_{k,n} [\mu (a_{k,n}^{\dagger} a_{k,n} + b_{k,n}^{\dagger} b_{k,n}) + t (a_{k,n}^{\dagger} b_{k,n-1} - 2a_{k,n}^{\dagger} b_{k,n} \cos(ka/2)) + \text{H.c.}],$$

$$H_{\Delta} = \sum_{k,n} [2i\Delta \sin(k) (a_{k,n}^{\dagger} a_{-k,n}^{\dagger} + b_{k,n+1}^{\dagger} b_{-k,n+1}^{\dagger}) + \text{H.c.}], \quad (3.5)$$

where $n = 1, 2$, corresponding to the top and bottom chain index. In the Bogoliubov-de Gennes (BdG) form we can express the Hamiltonian as:

$$\frac{1}{2} \sum_k \Psi^{\dagger} h(k) \Psi, \quad (3.6)$$

$$\Psi \equiv \left(a_{k,1}, a_{-k,1}^{\dagger}, b_{k,1}, b_{-k,1}^{\dagger}, a_{k,2}, a_{-k,2}^{\dagger}, b_{k,2}, b_{-k,2}^{\dagger} \right).$$

We obtain the total Hamiltonian in the following matrix form

$$h(k) = \begin{pmatrix} -2\mu & \Delta_k & -\varepsilon & 0 & 0 & 0 & 0 & 0 \\ \Delta_k^* & +2\mu & 0 & \varepsilon & 0 & 0 & 0 & 0 \\ -\varepsilon & 0 & -2\mu & \Delta_k & -t & 0 & 0 & 0 \\ 0 & \varepsilon & \Delta_k^* & +2\mu & 0 & t & 0 & 0 \\ 0 & 0 & -t & 0 & -2\mu & \Delta_k & -\varepsilon & 0 \\ 0 & 0 & 0 & t & \Delta_k^* & +2\mu & 0 & \varepsilon \\ 0 & 0 & 0 & 0 & -\varepsilon & 0 & -2\mu & \Delta_k \\ 0 & 0 & 0 & 0 & 0 & \varepsilon & \Delta_k^* & +2\mu \end{pmatrix}, \quad (3.7)$$

where $\Delta_k = 2i\Delta \sin(k)$ and $\varepsilon = -2t \cos(k/2)$. This Hamiltonian has the dispersion relations given by

$$\begin{aligned} E_{1,2,3,4} &= \pm \sqrt{\frac{-2\Delta^2 + 2\zeta_1 + t^2 \pm \tilde{\varepsilon}(4\mu + t)}{2}}, \\ E_{5,6} &= \pm \sqrt{\frac{-2\Delta^2 + 2\zeta_2 + t^2 - \tilde{\varepsilon}(4\mu - t)}{2}}, \\ \text{and } E_{7,8} &= \pm \sqrt{-\Delta^2 + \varepsilon^2 + 2\zeta_3 + \tilde{\varepsilon}(2\mu - t/2)}, \end{aligned} \quad (3.8)$$

with $\zeta_1 = \varepsilon^2 + 2\mu^2 + 2\mu t$, $\zeta_2 = \varepsilon^2 + 4\mu^2 - 2\mu t$, $\zeta_3 = 2\mu^2 - \mu t + t^2$ and $\tilde{\varepsilon} = \sqrt{4\varepsilon^2 + t^2}$. It is worth noting that Eq. (3.7) satisfies both the particle-hole and time-reversal symmetries, since

$$\mathcal{C}h(k)\mathcal{C}^{-1} = -h(-k), \quad (3.9)$$

and

$$\mathcal{T}h(k)\mathcal{T}^{-1} = h(-k), \quad (3.10)$$

where \mathcal{C} and \mathcal{T} are charge conjugation and time-reversal operators (77, 78), respectively.

Eq. (3.7) also satisfies the chiral symmetry

$$\mathcal{K}h(k)\mathcal{K}^{-1} = -h(k), \quad (3.11)$$

in which the chiral operator is defined by the anti-commutation relation $[\mathcal{K}, h(k)]_+ = 0$. Thus, one can write $h(k)$ in its corresponding chiral form by performing the following unitary transformation:

$$\tilde{h}(k) = \mathcal{U}^\dagger h(k) \mathcal{U} = \begin{bmatrix} 0 & A(k) \\ A^*(k) & 0 \end{bmatrix}, \quad (3.12)$$

where $A(k)$ is a 4×4 chiral matrix given by

$$A(k) = \begin{bmatrix} -4i\Delta \sin(k) + 4\mu & -4t \cos\left(\frac{k}{2}\right) & 0 & 0 \\ -4t \cos\left(\frac{k}{2}\right) & -4i\Delta \sin(k) + 4\mu & 2t & 0 \\ 0 & 2t & -4i\Delta \sin(k) + 4\mu & -4t \cos\left(\frac{k}{2}\right) \\ 0 & 0 & -4t \cos\left(\frac{k}{2}\right) & -4i\Delta \sin(k) + 4\mu \end{bmatrix}. \quad (3.13)$$

Once particle-hole, time-reversal, and chiral symmetries are preserved by $h(k)$, the corresponding system belongs to the BDI symmetry group class with \mathbb{Z} index (77, 78), with its topology being characterized by the associated Chern number invariant (79), i.e., the winding number (75, 76)

$$W = Tr \int_{-\pi}^{\pi} \frac{dk}{2\pi i} A_k^{-1} \partial_k A_k = - \int_{-\pi}^{\pi} \frac{dk}{2\pi i} \partial_k \ln[Det(A_k)], \quad (3.14)$$

which gives the number of MZMs at the edges of the spinless KzHNR, as discussed in Fig. 3.3. For a better understanding of this calculation, you can refer to the appendix A.

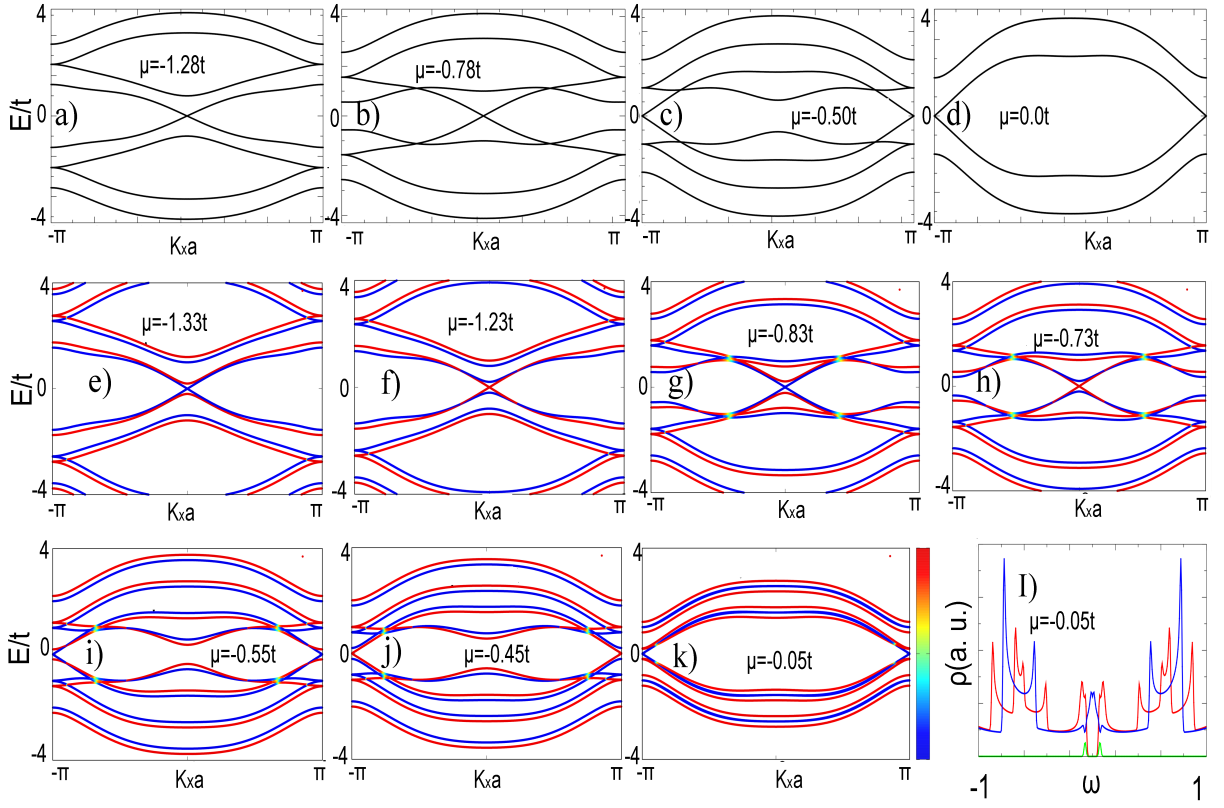


Figure 3.2: Figs (a)-(d): band structure for a $N = 2$ infinity double-spinless KzHNR, considering μ values where the TPTs occur. Figs (e)-(k): the same as top Figs, but considering both spin components (infinite double-spin KzHNR) 3.4. The energies are measured in units of t , and we fix the p -wave superconducting pairing parameter $\Delta = 0.5t$. Additionally, the parameters of the double-spin case (middle and bottom Figs) are $\lambda_R = 0.05t$ and $\lambda_Z = 0.1t$. In the double-spinless case we have four TPTs occurring at: a) $\mu = -1.28t$ b) $\mu = -0.78t$ c) $\mu = -0.50t$ d) $\mu = 0$. For the double-spin case, the TPTs occur at e) $\mu = -1.33t$ with spin down, f) $\mu = -1.23t$ with spin up g) $\mu = -0.84t$ with spin down, h) $\mu = -0.73t$ with spin up, i) $\mu = -0.55t$ with spin down j) $\mu = -0.45t$ with spin up k) $\mu = -0.05t$ with spin down. The density of states, corresponding to the band structure depicted in (k), is plotted in (l), where we can observe the half-metallicity characteristic of those TPTs.

In Fig. 3.2 (a)-(d), we plot the band relation dispersion [Eq. (3.8)] for a $N = 2$ infinity double-spinless KzHNR, considering μ/t values where the TPTs occur. For a) $\mu = -1.28t$ and b) $\mu = -0.78t$, the gap closes at $k = 0$, defining two TPTs and forming a topological phase in this interval with winding number equal to $W = 1$. A new TPT occurs at c) $\mu = -0.50t$, with the gap closing at $\vec{k} = \pi$, and defining a new topological region with winding number equal to $W = 2$ between $\mu = -0.78t$ and $\mu = -0.50t$. Finally, at d) $\mu = 0$ the gap closes again at $\vec{k} = \pi$, defining another TPT, and forming a topological phase with winding number equal to $W = 1$ between $\mu = -0.50t$ and $\mu = 0$. The same transitions appears at the same values for positive chemical potentials, once the system described by Eq. (3.7) exhibits a particle-hole symmetry.

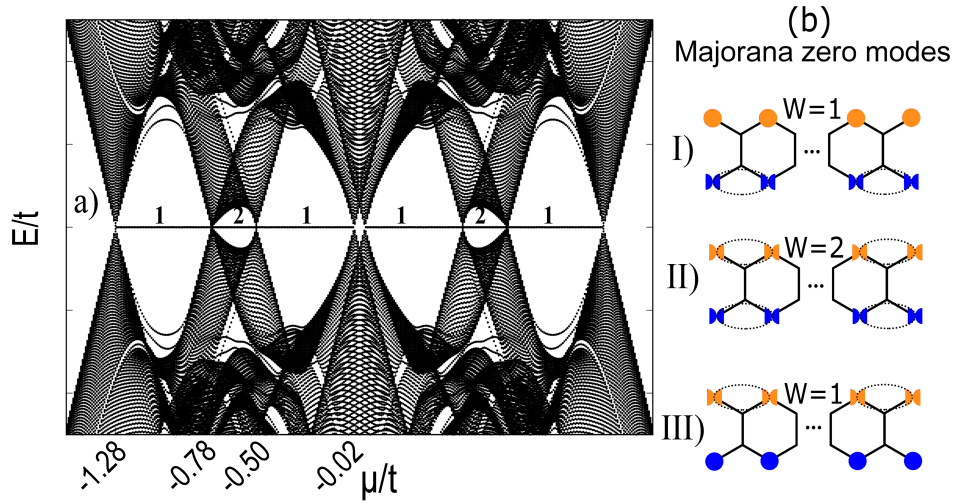


Figure 3.3: (a) Energy spectrum of a 2D double-spinless KzHNR [Eq. (3.1)] as a function of μ and p -wave pairing $\Delta = 0.5t$, for a KzHNR of width $N = 2$ and length $M = 200$. The numbers on the real axis represent the W associated with the corresponding topological region. (b) Schematic representation of the emergence of MZMs at the ends of the KzHNR for each associated W . Each semicircle represents an MZM generated on the site of the active border of the KzHNR. The two Majoranas connected with the dotted ellipses form a standard fermion. In the topological phase, unpaired Majorana fermions emerge at both ends of each KzHNR, as represented by the semicircles outside the dotted ellipses. The situations (I) and (III) describes $W = 1$, where only the top or bottom KzHNR generates one MZM at each of its ends. Otherwise, in (II) $W = 2$, indicating that both the KzHNRs generate MZMs simultaneously at their corresponding ends.

For simplicity, we only have considered a double-spinless KzHNR of width $N = 2$ in our numerical simulations. However, the results presented here are also valid for nanoribbons of larger widths.

Fig. 3.3(a) shows the bulk energy spectrum E/t of the double-spinless KzHNR [Eq. (3.1)] as a function of the chemical potential μ/t . Several TPTs characterized by the closing-and-reopening of superconducting induced gap appear at the $\mu = -1.28t$, $-0.78t$, $-0.50t$, and $-0.02t$, respectively. According to the bulk-boundary correspondence principle (80), the multiplicities of modes on the boundaries associated with the TPTs in bulk are characterized by topological invariants of the bulk energy bands, as the so-called winding number W , for instance. Here, we have found $W = 0$, $W = 1$ and $W = 2$ [see Fig. 3.2(a)-(d)], which are indicated in the corresponding regions of Fig. 3.3(a). Following the bulk-boundary principle, $W = 0$ ($\mu > |1.28t|$) characterizes the trivial phase, where MZMs are absent at the ends of both the KzHNRs. Between $\mu = -1.28t$ and $\mu = -0.78t$, a topological region is characterized by $W = 1$, indicating the emergence of MZMs at opposite ends of either bottom or top KzHNR [Fig.3.3(b), cases (I) and (III)].

Fig. 3.3(a) also exhibits another topological region characterized by $W = 2$ in the interval $-0.78t < \mu < -0.50t$, for instance, corresponding to the situation in which the MZMs arises

simultaneously in the ends of both top and bottom KzHNR, as indicated in the sketch (II) of Fig. 3.3(b). In Fig. 3.3(a), we also can notice that the same TPTs which occur for $\mu < 0$ appear for positive values of μ due to the particle-hole symmetry exhibited by the Hamiltonian of Eq. (3.1)¹.

3.4 Spin full model and emergence of spin-polarized MZMs

To analyze the possibility of distinguishing the spin species of the MZMs, we now discuss the emergence of MZMs at the double-spin KzHNR geometry edges, considering both spin orientations explicitly. We account for the infinite version of the whole spin case (see Fig. 3.2(e-k)). Here we discuss the finite version of the model. To properly break the spin degeneracy of the system, we introduce two additional effects in the Hamiltonian of Eq. (3.1): the extrinsic RSOC and an EMF. The extrinsic RSOC lifts the corresponding bands' spin degeneracy, unless at $\mathbf{k} = 0$. Additionally, the EMF applied perpendicularly to the ribbon plane drives the system through TPTs exhibiting spin-polarized MZMs. In this situation, spin-discriminated MZMs emerge at the ends of the double-spin KzHNR structure. The corresponding generalized Hamiltonian is given by

$$H = H_t + H_\Delta + H_R + H_z, \quad (3.15)$$

which can be written in a new basis of four distinct atoms as indicated in Fig. 3.4. On this basis,

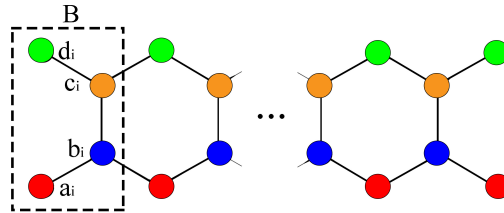


Figura 3.4: Scheme of the basis adopted in the Hamiltonian given by the Eqs. (4-8) describing the finite double-spin KzHNR chain of width $N = 2$. The unit cell B , represented by the dashed rectangular area is built with four distinct atoms a_i, b_i, c_i and d_i .

¹It also should be noticed in Fig. 3.3(a) that there is an uncharacterized small region in the interval $-0.02t < \mu < 0.02t$, which is an effect produced by the finite length of the KzHNR chain considered in the calculations ($M = 200$) and therefore tends to disappear for larger values of M , giving rise to a single TPT at $\mu = 0$.

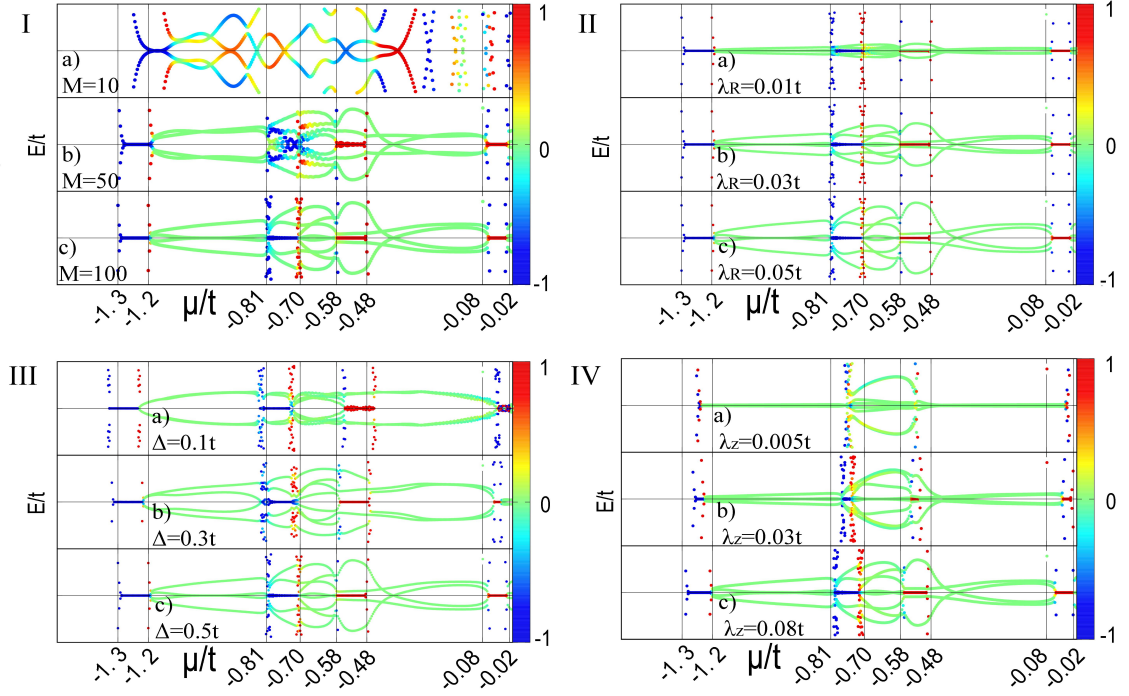


Figure 3.5: Formation of MZMs parameter study: Energy spectra for a $N = 2$ finite double-spin KzHNR as a function of μ . We employed the same parameters set used in all the simulations of the work: $\Delta = 0.5t$, $\lambda_R = 0.05t$ and $\lambda_z = 0.1t$, but only changing the particular parameter indicated in the figure: I) Length: $M = 10, 50, 100$. II) Extrinsic Rashba spin-orbit coupling $\lambda_R = 0.01t, 0.03t, 0.05t$. III) Superconductor pairing $\Delta = 0.1t, 0.3t, 0.5t$. IV) EMF $\lambda_z = 0.005t, 0.03, 0.08t$.

the Hamiltonian describing the NN hopping and the p -wave superconducting pairing reads

$$\begin{aligned}
H_t = & -\frac{\mu}{2} \sum_{i,\sigma}^M (a_{i\sigma}^\dagger a_{i\sigma} - a_{i\sigma} a_{i\sigma}^\dagger + b_{i\sigma}^\dagger b_{i\sigma} - b_{i\sigma} b_{i\sigma}^\dagger + \\
& c_{i\sigma}^\dagger c_{i\sigma} - c_{i\sigma} c_{i\sigma}^\dagger + d_{i\sigma}^\dagger d_{i\sigma} - d_{i\sigma} d_{i\sigma}^\dagger) - \\
& \frac{t}{4} \sum_i^M (a_{i\sigma}^\dagger b_{i\sigma} - b_{i\sigma} a_{i\sigma}^\dagger + b_{i\sigma}^\dagger c_{i\sigma} - c_{i\sigma} b_{i\sigma}^\dagger + d_{i\sigma}^\dagger c_{i\sigma} - c_{i\sigma} d_{i\sigma}^\dagger) - \\
& \sum_i^{M-1} \frac{t}{4} (a_{i\sigma}^\dagger b_{i+1\sigma} - b_{i+1\sigma} a_{i\sigma}^\dagger + d_{i\sigma}^\dagger c_{i+1\sigma} - c_{i+1\sigma} d_{i\sigma}^\dagger) + \text{H.c.},
\end{aligned} \tag{3.16}$$

and

$$\begin{aligned}
H_\Delta = & \sum_i^{M-1} [\Delta (a_{i\sigma} a_{i+1\sigma} - a_{i+1\sigma} a_{i\sigma} + \\
& d_{i\sigma} d_{i+1\sigma} - d_{i+1\sigma} d_{i\sigma}) + \text{H.c.}],
\end{aligned} \tag{3.17}$$

respectively.

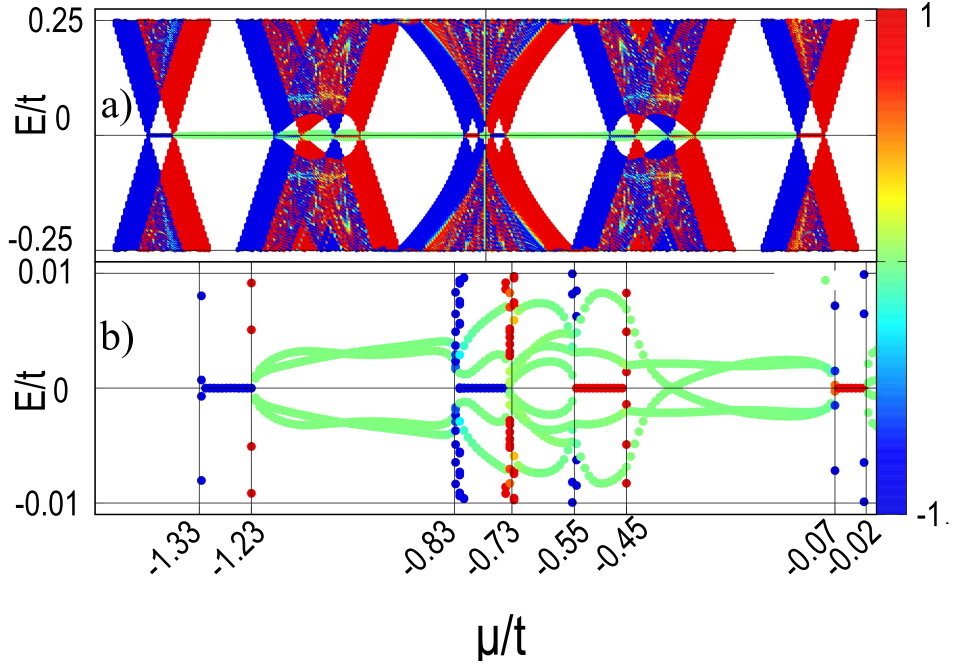


Figure 3.6: (a) Energy spectra of a finite double-spin KzHNR [Eq. 3.15] as a function of μ , $N = 2$ and $M = 200$. The model parameters are $\Delta = 0.5t$, $\lambda_R = 0.05t$ and $\lambda_Z = 0.1t$. The blue and red colors correspond to spin up and down regions at the real axis, respectively. The green lines describe the formation of a regular fermion coming from the combination of Majorana excitations belonging to opposite KzHNRs. (b) Zoomed region of (a) around $E = 0$ for $\mu < 0$, showing in detail the formation of spin-polarized MZMs.

The extrinsic RSOC induced in the KzHNR can be generated by breaking the inversion symmetry due to either a substrate with strong spin-orbit interaction (13) or modulated by the action of an external electric field \vec{E} applied perpendicularly to the nanoribbon plane (60–62, 64, 81, 82). Its corresponding general Hamiltonian reads

$$H_R = \sum_{i,j,\sigma} [ia_{i,\sigma}^\dagger (\vec{u}_{ij} \cdot \vec{\sigma}) a_{j,\sigma} + \text{H.c.}], \quad (3.18)$$

where $\vec{u}_{ij} = \left(\frac{e}{2m^2av_f} \right) \vec{E} \times \vec{\delta}_{ij} = -\frac{\lambda_R}{a} \hat{k} \times \vec{\delta}_{ij}$, with e and m being the charge and mass of the electron, respectively. Moreover, v_f is the Fermi velocity, the lattice constant is given by a and the vector-position $\vec{\delta}_{ij}$ corresponds to the three nearest neighbors, as represented in Fig. 1(b).

Writing Eq. (3.18) in the basis defined in Fig. 3.4, we can write the Rashba Hamiltonian as

$$\begin{aligned}
H_R = & \sum_{i,\sigma}^M i\lambda_R \text{sign}(\sigma) [\gamma_1 (a_{i\sigma}^\dagger b_{i\bar{\sigma}} - b_{i\sigma} a_{i\bar{\sigma}}^\dagger) + \\
& \left(-\frac{1}{2}\right) (b_{i\sigma}^\dagger c_{i\bar{\sigma}} - c_{i\sigma} b_{i\bar{\sigma}}^\dagger) + \gamma_2 (c_{i\sigma}^\dagger d_{i\bar{\sigma}} - d_{i\sigma} c_{i\bar{\sigma}}^\dagger)] \\
& + \sum_{i,\sigma}^{M-1} i\lambda_R \text{sign}(\sigma) [\gamma_2 (b_{i\sigma}^\dagger a_{i+1\bar{\sigma}} - a_{i+1\sigma} b_{i\bar{\sigma}}^\dagger) + \\
& \gamma_1 (d_{i\sigma}^\dagger c_{i+1\bar{\sigma}} - c_{i+1\sigma} d_{i\bar{\sigma}}^\dagger)] + \text{H.c.},
\end{aligned} \tag{3.19}$$

where $\gamma_1 = \left(\frac{1}{2} + i\frac{\sqrt{3}}{2}\right)$, $\gamma_2 = \left(\frac{1}{2} - i\frac{\sqrt{3}}{2}\right)$, λ_R is the extrinsic RSOC parameter and $\sigma = \uparrow, \downarrow$ is the spin index for each operator. The last term of Eq. (3.15)

$$\begin{aligned}
H_z = & \frac{1}{2} \sum_{i,\sigma}^M \lambda_Z \text{sign}(\sigma) [(a_{i,\sigma}^\dagger a_{i,\sigma} - a_{i,\sigma} a_{i,\sigma}^\dagger) + \\
& (b_{i,\sigma}^\dagger b_{i,\sigma} - b_{i,\sigma} b_{i,\sigma}^\dagger) + (c_{i,\sigma}^\dagger c_{i,\sigma} - c_{i,\sigma} c_{i,\sigma}^\dagger) + \\
& (d_{i,\sigma}^\dagger d_{i,\sigma} - d_{i,\sigma} d_{i,\sigma}^\dagger)] + \text{H.c.},
\end{aligned} \tag{3.20}$$

represents an EMF with the magnetization vector pointing to the azimuthal direction (83, 84), where λ_Z is the EMF strength.

Now, we perform a detailed analysis of how the KzHNR length M , the extrinsic RSOC λ_R , the superconducting pairing Δ and the EMF λ_Z affects the emergence of MZMs on the real axis. The Hamiltonian given by Eqs. (4-8), is solved numerically using the basis represented in Fig. 3.4. The calculation becomes more time-consuming as the Hamiltonian matrix dimension grows with the value of M .

In Figs. 3.5(I)-(IV), we plot the energy spectra as a function of μ of a double-spin KzHNR with width $N = 2$ and length $M = 100$, for distinct parameters of the Hamiltonian: $\Delta = 0.5t$, $\lambda_R = 0.05t$, and $\lambda_Z = 0.1t$ except the corresponding varied parameter. We explicitly indicate it in the Figs.

The emergence of polarized MZMs at the edges of the double-spin KzHNR is calculated by computing the mean value of $\langle S_z \rangle = \langle \psi | \hat{S}_z | \psi \rangle$ of MZMs solutions. The label ψ represents eigenvectors of the total Hamiltonian given by Eq. (3.15) and \hat{S}_z is the Pauli matrix in the \hat{z} direction.

Figure 3.5-I shows the dependence of the energy spectra as a function of μ/t for lengths $M = 10$ (a), 50(b) and 100(c) of the double-spin KzHNR, respectively. In Fig (a), we can verify oscillatory patterns for the smallest double spin-KzHNR structure. The oscillating behavior is

expected to appear for short Majorana nanowires due to overlapping MZMs of opposite edges. For $M = 50$ (b), we observe the appearance of MZMs at the real axis around $\mu = 0$ and in the inferior band region in the range, $\mu = [-1.2, -1.3]$. Fig (c) depicts the case of $M = 100$, showing the MZMs on the real axis in all the available topological regions.

Figure 3.5-II shows the dependence of the energy spectra as a function of μ/t with the extrinsic RSOC parameters $\lambda_R = 0.01t, 0.03t$ and $0.05t$. The result shows that a low value of λ_R is sufficient to generate well-defined MZMs on the real axis in all the topological regions.

In Fig. 3.5-III, we observe the dependence of the energy spectra as a function of μ/t for $\Delta = 0.1t, 0.3t$ and $0.5t$, in Figs (a), (b) and (c), respectively. These profiles indicate that the p-wave pairing Δ strongly affects the MZMs formation on the real axis. The MZMs are formed first, for $\Delta = 0.1t$ (a) in the range $\mu = [-1.2, -1.3]$. Only when $\Delta = 0.5t$ (b), the MZMs emerges around $\mu = 0$. Well-defined MZMs arises in the region of $\mu \simeq 0$ only for higher values of Δ .

Fig. 3.5-IV shows the dependence of the energy spectra with the EMF for $\lambda_Z = 0.005t$ (a), $0.03t$ (b) and $0.08t$ (c) as a function of μ/t . The EMF acts uniformly over the MZMs formation for all μ values. The enhancement of λ_Z also increases the number of MZMs over the real axis.

The parameters analysis presented in Fig. 3.5 help us to chose the parameters used in Fig. 3.6, that shows the high-resolution energy spectrum E/t of a finite double-spin KzHNR with $N = 2, M = 200, \Delta = 0.5t, \lambda_R = 0.05t$ and $\lambda_Z = 0.1t$ as a function of μ/t . Fig. 3.6(a) has the same shape of the double-spinless case [Fig. 3.3(a)], but with spin-polarized energies resolved into spin-up (blue color) and spin-down (red color) regions at the real axis. A mirror spin-symmetry concerning $\mu = 0$ is observed in the plot: a spin-up MZMs for $\mu < 0$ changes to spin-down for $\mu > 0$. Moreover, spin-polarized MZMs can be accessed by tuning μ slightly below or above $\mu = 0$.

Fig. 3.6(b) shows the zoomed region of (a) around $E = 0$ for $\mu < 0$, where it is possible to see in detail the emergence of spin-polarized MZMs as μ changes. We can detect these MZMs with well-defined spin orientation via spin-polarized STM measurements (85). The green lines depicted in both Figs of Fig. 3.6 do not represent MZMs, but ordinary fermions, resulting from the combination of MZMs localized at the ends of opposite KzHNRS. This effect tends to disappear as the width N of the double-spin KzHNR increases.

As discussed in the spinless case of Fig. 3.3, the emergence of spin-polarized MZMs on the real axis depicted in Fig. 3.6 is also related to TPTs in the bulk gap. However, each value of μ related to a TPT in the spinless scenario splits into two values of μ , describing TPTs for both spin up and down components. The strength of this splitting is given by the RSOC parameter

λ_R . For details, see Fig. 3.2.

Considering the Fourier transform of the total Hamiltonian given by 3.15, we calculate the topological phase transitions for the infinite spinfull case as a function of the chemical potential. By considering again $n = 1, 2$, as the top and bottom chain indexes,

$$H_t = - \sum_{k,n,\sigma}^N \mu (a_{k,n,\sigma}^\dagger a_{k,n,\sigma} + b_{k,n,\sigma}^\dagger b_{k,n,\sigma}) + t (a_{k,n,\sigma}^\dagger b_{k,n-1,\sigma} - 2a_{k,n,\sigma}^\dagger b_{k,n,\sigma} \cos(ka/2)) + H.c., \quad (3.21)$$

$$H_\Delta = \sum_{k,n,\sigma}^N \Delta_k (a_{k,n,\sigma}^\dagger a_{-k,n,\sigma}^\dagger + b_{k,n+1,\sigma}^\dagger b_{-k,n+1,\sigma}^\dagger) + H.c.; \quad (3.22)$$

$$\Delta_k = 2i\Delta \sin(k),$$

$$H_R = \sum_{k,n,\sigma}^N \Lambda_{R\sigma} \left[-a_{k,n,\sigma}^\dagger b_{k,n-1,\bar{\sigma}} - 2 \cos \left(k/2 - \frac{2\pi}{3} \right) a_{k,n,\sigma}^\dagger b_{k,n,\bar{\sigma}} + b_{k,n,\sigma}^\dagger a_{k,n+1,\bar{\sigma}} + 2 \cos \left(k/2 + \frac{2\pi}{3} \right) b_{k,n,\sigma}^\dagger a_{k,n,\bar{\sigma}} \right] + H.c.; \quad (3.23)$$

$$\Lambda_{R\sigma} = i\lambda_R \text{sign}(\sigma),$$

and

$$H_z = \sum_{k,n,\sigma}^N \text{sign}(\sigma) \lambda_Z (a_{k,n,\sigma}^\dagger a_{k,n,\sigma} + b_{k,n,\sigma}^\dagger b_{k,n,\sigma}) + H.c.. \quad (3.24)$$

In Fig. 3.2(e)-(k), we plot the band structure [Eqs. (3.21) - (3.24)] for a $N = 2$ infinity double-spin KzHNR, considering μ values where the TPTs occur. To discriminate the two possible spin orientations in the edges of the KzHNR, we introduce two new physical effects: the extrinsic RSOC and the EMF given by Eqs. (3.23) and Eq. (3.24). When compared to the previous case, each transition splits into two, one with spin up and the other with spin down, where the split is tuned by the $\lambda_R = \pm 0.05t$ parameter. For example, the TPT that occurs at Fig 3.2(a) $\mu = -1.28t$, for the spinless case splits into $\mu \rightarrow \mu \pm \lambda_R = -1.33t; -1.23t$ in Figs 3.2(e) and (f), respectively. However, in the double-spin case, we did not obtain the winding numbers due to the involved complexity of the calculations.

In Fig. 3.2(l), we plot a typical density of states for $\mu = -0.05t$ in a point where a TPT occurs and that exhibits half-metallicity; what is another striking characteristic that occurs in all the other Majorana TPTs of the system. This effect leads the double-spin KzHNR into a half-metallic state as indicated in Fig. 3.2(l), resulting in insulating behavior for one spin component

and metallic behavior for the other component (86, 87).

3.5 Experimental perspectives

Among available experimental results for realizing a double-spin KzHNR structure, we suggest the silicene deposited on a Pb superconducting substrate as a possible candidate. In the superconducting phase, under the presence of a strong RSOC coming from the Pb and an applied EMF, the Cooper pairs of the Pb substrate can enter into the silicene region via proximity effect, giving rise to a *p*-wave-induced pairing in the double KzHNR structure.

The growth of silicene under Pb substrates was experimentally investigated using guidelines of DFT simulations results (88–91). However, the production of silicene nanoribbons inducing Pb reconstructions on Si(111) surface (92) was not successful. It was obtained short silicene-like nanoribbons directly bonded to the Si(111) layers, and Pb only acted as a surfactant.

A possible route to produce silicene nanoribbons (93) is to use Pb layers on vicinal Si surfaces (54–56), like Si(553) or Si(557). In the case of Pb/Si(553), Pb forms a dense layer. The Pb layer is electronically decoupled from the substrate to a large extent. This is entirely different from the case of Pb-induced Si(111) reconstruction. Strong Pb-Pb bonding within the layer should favor the growth of Si on it without migration of Pb atoms on top of silicene.

Moreover, several previous theoretical studies have shown that the zHNRs accumulate electrons to form localized magnetic moments (94) at its edges. The coupling of atoms belonging to the same edge is ferromagnetic and between atoms from different edges is antiferromagnetic (95–98). This situation is depicted in Fig. 3.1(c). In particular, low-width silicene nanoribbons are predicted to have an antiferromagnetic ground state (99, 100). Another possibility to experimentally realize a double spin-polarized KzHNR is following the recipe of the reference (13): growing an antiferromagnetic nanoribbon or some artificial antiferromagnetic ladder over a strong spin-orbit conventional *s*-wave superconductor. In Appendix B, we present an estimative about the possibilities to experimentally realize a double-spin KzHNR based on silicene layers deposited on top of a Pb superconducting substrate.

3.6 Conclusions

This work reports the possibility of obtaining spin-polarized MZMs at opposite edges of a double-spin KzHNR structure. The regions of energy spectrum E/t with MZMs having well-defined either spin up or down orientations can be accessed by tuning the μ/t of the KzHNRs.

Moreover, these spin-polarized intervals in the $E/t \times \mu/t$ profile are associated with distinct topological phases, characterized by the topological invariant winding number $W = 1$ or $W = 2$. Interestingly enough, for the situation wherein $W = 2$ four MZMs emerge in the double KzHNR geometry: two at the opposite ends of the top zHNR and two at the opposite ends of the bottom one. In this scenario, it should be emphasized that at least four MZMs are required for defining a qubit (101–104). Thus, the proposal is a natural candidate for realizing hybrid quantum computing operations (72, 73) between conventional spin qubits and topological qubits based on MZMs with well-defined spin orientation, suggesting a possible route for performing Majorana spintronics.

Capítulo 4

STUDYING THE EMERGENCE OF MAJORANA ZERO MODES IN PENTA-SILICENE NANORIBBONS

4.1 Introduction

Ultra-scaling of nanoelectronic devices, beyond Moore's law, still using the ubiquitous silicon technology, could come from silicene (18–20), the first silicon-based graphene-like artificial two-dimensional (2D) quantum material, which further engendered the Xenes family (105), and which was used to fabricate an atom-thin channel in a field effect transistor (106, 107). Moreover, topological silicon nanowires hosting Majorana fermions could be a materials platform for a quantum computer (24). However, like other nanowire candidates, even proximitized ones based on heavier constituents with larger spin-orbit coupling, until now, no conclusive experimental measurements guarantee incontrovertibly the existence of topologically protected Majorana-zero-modes (MZMs) for the possible realization of qubits (21, 22). A paradigmatic breakthrough would be the experimental implementation of the generic Kitaev toy model with a silicon platform (3). Theoretically, spin-polarized MZMs could be harbored at the opposite ends of a one-dimensional (1D) linear zig-zag honeycomb nanoribbon (zHNR) mimicking two parallel Kitaev chains connected by a hopping term (17). However, no such setup based on zHNRs has been realized until now. Instead, a realistic implementation might be obtained by using the straight, highly perfect, and massively aligned atom-thin penta-silicene nanoribbons with a very high aspect ratio (p-SiNRs), purely composed of silicon pentagonal building blocks and grown by molecular beam epitaxy on the (110) surface a silver crystal template (2). These p-SiNRs are displayed in Fig. 4.1. We will theoretically demonstrate that these p-SiNRs could constitute a tantalizing disruptive new Kitaev platform.

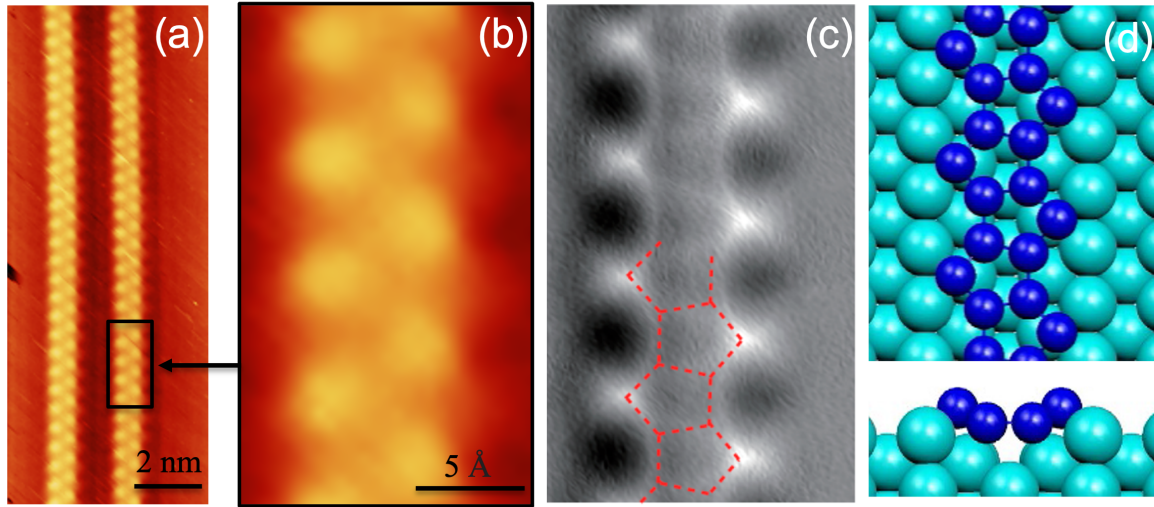


Figure 4.1: (Color online) Si SNR on Ag(110) surface. (a) and (b) Experimental STM images (uncorrected drift), (c) High-resolution nc-AFM image. (d) Top and cross view of the arrangement of the Si pentagonal building blocks. (a) and (b) Courtesy Eric Salomon, (c) Reprinted with permission from (1). Copyright 2023 American Chemical Society. (d) From Cerda et al.(2).

Since the appearance of the generic Kitaev model (3), several platforms were proposed to realize it, both from theoretical (11, 15, 36–38, 41, 42), and experimental points of view (9, 10, 12–14, 35, 108). A helpful review of the experimental state-of-the-art on this subject can be found in Refs. (22, 40, 109).

This model takes into account p -wave superconductor pairing between electrons in different sites of a one-dimensional chain (Kitaev chain) and predicts the existence of unpaired MZMs at opposite ends of a finite Kitaev chain. However, until now, there are no conclusive experimental measurements that guarantee without doubt the existence of topologically protected MZMs (46–48) except, possibly, rare cases, such as chains comprising a few magnetic adatoms placed one by one on a superconducting surface (110, 111). Per se, this situation justifies the search for new platforms.

One possible alternative platform is the one-dimensional (1D) HNRs that have been receiving growing attention in the literature (17, 49, 50, 76). Nevertheless, the mono-elemental 2D graphene-like materials coined Xenes, where X represents elements from group IIIA to group VIA of the periodic table, could constitute possible candidates to build zHNRs with the ability to harbor MZMs at their ends (51–53, 112). Penta-Silicene ($X=Si$) is a highly promising candidate in this family for obtaining a zHNR geometry that can host MZMs (1, 2, 113).

In a previous work (17), we addressed the problem of Majorana spin discrimination em-

ploying a double-spin Kitaev zigzag honeycomb nanoribbons (KzHNR), which mimics two parallel Kitaev chains connected by the hopping t (see figure 1 of (17)). Since such KzHNRs have not been realized in experiments, we look instead in the present work at the possibility of obtaining MZMs in p-SiNRs, harboring Dirac fermions, which have been epitaxially grown on Ag(110) surfaces (2, 114–116). Typically, highly perfect, atom thin, massively aligned single strand p-SiNRs, 0.8 nm in width, and with lengths extending to tens of nanometers were obtained by molecular beam epitaxy upon in situ Si deposition onto Ag(110) surfaces held at room temperature, as shown in Fig. 4.1(a). In scanning tunneling microscopy (STM) and high-resolution nc-AFM images, these p-SiNRs appear as two shifted lines of protrusions along the [110] direction as shown in Fig. 4.1(b-c) and are separated by twice the nearest neighbor Ag-Ag distance, i.e., 0.577 nm. Their hidden internal atomic structure was initially uncovered employing thorough density functional theory (DFT) calculations and simulations of the STM images (2), pointing to an arrangement of pure Si pentagonal building blocks, as displayed in Fig. 4.1(d), which defines the missing pentagonal row (P-MR) model employed in the Supplemental information of reference (2) to optimize the angles and the distance between the silicon atoms in the pentagonal arrangement. This unique atomic geometry was later directly visualized by high-resolution non-contact atomic force microscopy (Fig. 4.1(c) from (1)).

We propose an experimental implementation for discriminating spin-polarized MZMs in p-SiNRs grown on the Ag(110) surface and all aligned along the [110] direction. Since silver is not a superconductor, we will proximitize them with lead, a conventional Bardeen–Cooper–Schrieffer (BCS) superconductor with a relatively high critical temperature of $T_c = 7.2$ K, upon evaporating *in situ* a thin lead film on top through a mask, as already mentioned in (105). Indeed, Pb can be easily grown on Ag(110) surfaces (117) and is known to interact only very weakly with the SiNRs, preserving their integrity and their electronic properties (88, 90). Then, detecting and distinguishing the MZMs at the ends of the SiNRs will be done *in situ* at low temperatures with the sSTM following the methodology of Yazdani and co-workers (118).

In this work, we will show that the spinless and spinful p-SiNRs with p -wave superconducting pairing reveal the emergence of topologically protected MZMs at opposite ends of the p-SiNRs.

4.2 Lattice transformations

In Fig. 4.2(a), to reduce the geometry complexity of the p-SiNR and facilitate the tight-binding calculations, we redefine its structure using square-shaped pentagons. Now the projec-

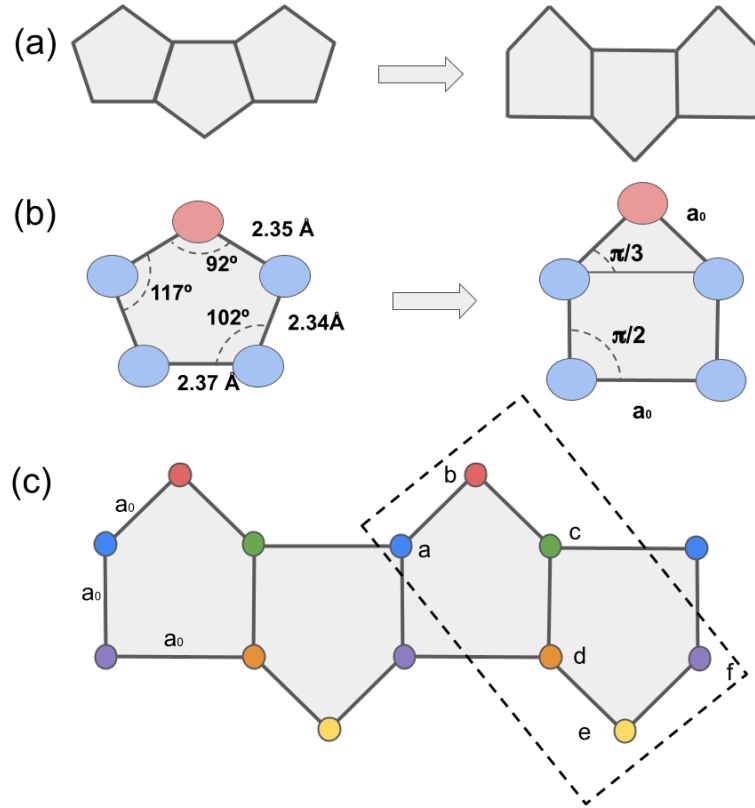


Figura 4.2: (Color online) (a) Penta-silicene (p-SiNRs) lattice transformation adopted. (b) Penta-silicene angles. (c) Sketch of nonequivalent Si atoms placed at the vertices of the “square” pentagonal lattice. We also represent the unit cell employed by the atoms inside the dashed rectangle in the simulations.

tion of the atoms that make three bonds over the x -axis are symmetrical. In the geometry of the pentagons that constitute the p-SiNRs of Fig. 4.2(b), four silicon atoms are located on the missing row plane, and only one exhibits a buckling structure (pink atoms). We neglect the buckling structure of these atoms and employ a planar configuration composed of square-shaped pentagons. As the distance between the silicon atoms that constitute the pentagons are close, we consider them equal to the lattice parameter of the p-SiNR, a_0 , and the nearest neighbor hopping equal to t . $M \equiv 2na_0$, where a_0 is the distance between atoms, as indicated in Fig. 4.2 and M is the size of the nanoribbon and N is the number of rowed unit cells. Fig. 4.2(c) exhibits the shape of the p-SiNR and the unit cell composed of six atoms inside the dashed rectangle employed in the calculations. We expect these simplifications will not change the results once we keep the lattice features.

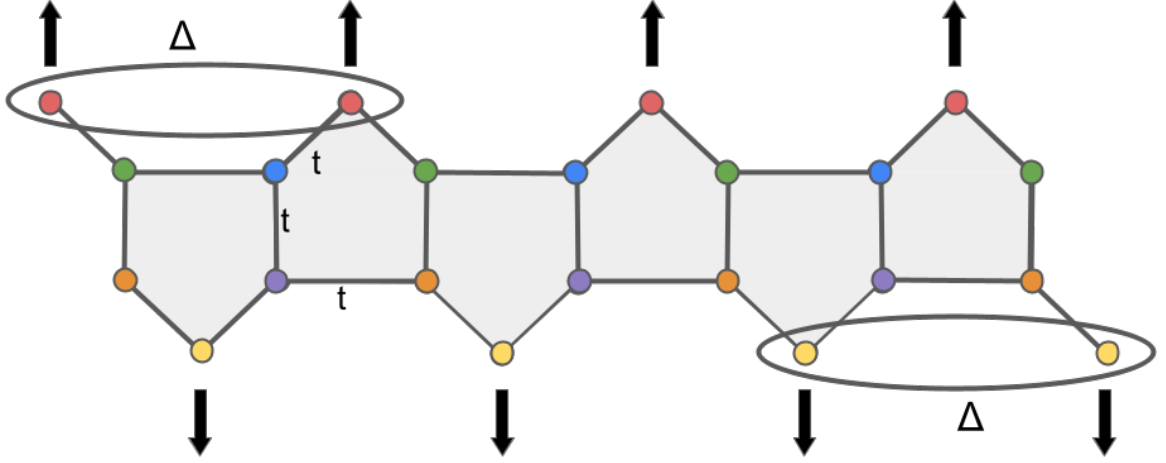


Figure 4.3: (Color online) Sketch of the penta-silicene nanoribbons: The penta-silicene system can be viewed as a top and a bottom Kitaev chains hybridized via hopping t . The ellipses represent the superconducting p -wave pairing between the pink (above) and yellow (below) silicon atoms (in the real material, these atoms correspond to the bucked one). The arrows only indicate the spin polarization needed to define a Kitaev chain.

4.3 Effective Hamiltonian - spinless case

The total Hamiltonian, which describes the p-SiNR of Fig. 4.3 is given by

$$H = H_t + H_\Delta, \quad (4.1)$$

with

$$\begin{aligned}
H_t = & - \sum_{i=1}^N \mu \left(a_{i,+}^\dagger a_{i,+} - a_{i,-}^\dagger a_{i,-} + b_{i,+}^\dagger b_{i,+} - b_{i,-}^\dagger b_{i,-} + \right. \\
& c_{i,+}^\dagger c_{i,+} - c_{i,-}^\dagger c_{i,-} + d_{i,+}^\dagger d_{i,+} - d_{i,-}^\dagger d_{i,-} + \\
& \left. e_{i,+}^\dagger e_{i,+} - e_{i,-}^\dagger e_{i,-} + f_{i,+}^\dagger f_{i,+} - f_{i,-}^\dagger f_{i,-} \right) - \\
& \sum_{i=1}^N t \left(a_i^\dagger b_i - b_i a_i^\dagger + b_i^\dagger c_i - c_i b_i^\dagger + \right. \\
& \left. c_i^\dagger d_i - d_i c_i^\dagger + d_i^\dagger e_i - e_i d_i^\dagger + e_i^\dagger f_i - f_i e_i^\dagger \right) - \\
& \sum_{i=1}^{N-1} t \left(a_{i+1}^\dagger f_i - f_i a_{i+1}^\dagger + a_{i+1}^\dagger c_i - c_i a_{i+1}^\dagger + d_{i+1}^\dagger f_i - f_i d_{i+1}^\dagger \right) + H.c,
\end{aligned} \quad (4.2)$$

where μ is the chemical potential, all the hopping terms between the atoms equal t , which is considered the energy unit. The index (-) and (+) differentiate the creation and annihilation operators of electrons and holes. The system Hamiltonian of Eq. (4.2) was built according to

the unit cell of nonequivalent Si atoms (a,b,c,d,e,f) shown in Fig. 4.2(b).

The p-SiNRs are grown on Ag(110) surfaces in the setup proposed here. However, silver is not a superconductor, and to generate a p -wave pairing Δ on the pink atoms of Fig. 4.3, we evaporate in situ a thin lead film over the Ag(110) surface in such a way that the buckled silicon atoms enter in contact with the lead atoms. Under the presence of a strong RSOC coming from the Pb atoms and an applied magnetic field, the s -wave Cooper pairs of the Pb film can enter into the p-SiNH region via proximity effect (Andreev reflections) (11), giving rise to a p -wave-induced pairing in the double p-HNRs structure. By following the same procedure done in our previous work (17) and based on the Kitaev model (3), we introduce a spinless superconducting pairing between the “external” atoms of the same type as shown in Fig. 4.3. The Hamiltonian, which describes such a pairing, reads

$$H_{\Delta} = \sum_{i=1}^{N-1} \Delta \left(b_i^{\dagger} b_{i+1}^{\dagger} - b_{i+1}^{\dagger} b_i^{\dagger} + e_i^{\dagger} e_{i+1}^{\dagger} - e_{i+1}^{\dagger} e_i^{\dagger} + \text{H.c.} \right), \quad (4.3)$$

where Δ is the superconducting pairing strength associated with the symmetry of the superconducting (SC) gap, and H.c is the hermitian conjugate.

4.3.1 Bulk calculations

To do the fourier transform and to calculate the properties we are interested in we can simplify the system by doing the projection of atoms “b” and “e” on the x axis. Now as we can see in the figure 4.4 we have two chains interconnected by atoms “c”, “d” and “a” , “f”. Considering this new lattice, and considering that all hoppings (“t”) are equal, we can build the Hamiltonian Eq.4.2. The parameter a_0 is the side of the square and the distance between ‘a’ and ‘b’ (‘d’ and ‘e’) is $a_0/2$.

Taking into account that our system has transnational symmetry in the direction of the x axis, we can make the transformation to the space of the wave vectors k , where we can calculate the band structures of the Bulk, for this we have to make a discrete Fourier transform .

$$a_n = \frac{1}{\sqrt{N}} \sum_k a_k e^{ikR_a} \quad (4.4)$$

where R_a is the position of the atom in the x axis. Using this transformation in a arbitrary case for operator “ a_{aj+R_a} ” and “ b_{aj+R_b} ” where R_a and R_b are the positions of the atoms a and b

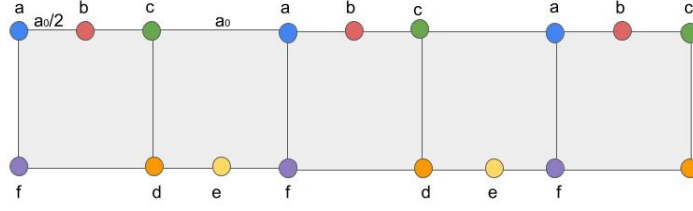


Figura 4.4: Representation of the simplified pentasilicene scheme with x-projections

respectively.

$$\begin{aligned}
 \sum_n^N a_j^\dagger b_j &= \sum_j \frac{1}{\sqrt{N}} \sum_k a_k^\dagger e^{-ik(a_j+R_a)} \sum_j \frac{1}{\sqrt{N}} \sum_k b_{k'} e^{ik'(a_j+R_b)} \\
 &= \frac{1}{N} \sum_k \sum_{k'} a_k^\dagger b_{k'}^\dagger \sum_j e^{-ik(a_j+R_a)} b_{k'} e^{ik'(a_j+R_b)} \\
 &= \sum_k \sum_{k'} a_k^\dagger b_{k'}^\dagger \frac{1}{N} \sum_j e^{-i(k-k')a_j} e^{-i(k'R_a)} e^{i(kR_b)}
 \end{aligned} \tag{4.5}$$

using

$$\frac{1}{N} \sum_n^N e^{-ian(k-k')} = \delta_{k,k'} \tag{4.6}$$

$$\begin{aligned}
 \sum_k \sum_{k'} a_k^\dagger b_{k'}^\dagger (\delta_{k,k'}) e^{-i(k'R_a)} e^{i(kR_b)} \\
 = \sum_k a_k^\dagger b_k e^{ik(R_b-R_a)}
 \end{aligned} \tag{4.7}$$

now we can use the Eq. 4.7 to make the Fourier transform to our Hamiltonian. for example the first term in the Hamiltonian Eq.4.2 ($a_i^\dagger b_i$) where the position in x axis for “a” is $R_a = 0$ and for “b” is $R_b = a/2$ and substitute in Eq. 4.7 we have the first term in k space.

$$\sum_n^N a_i^\dagger b_i = \sum_k a_k^\dagger b_k e^{ik(a_0/2)} \tag{4.8}$$

Doing for the other terms, we have our Hamiltonian in k space ($H(k)$).

$$\begin{aligned}
 H(k) &= \sum_k a_k^\dagger b_k e^{ik(a_0/2)} + a_k^\dagger f_k + a_k^\dagger c_k e^{ik(-a_0)} + b_k^\dagger c_k e^{ik(a_0/2)} + \\
 & c_k^\dagger d_k + d_k^\dagger e_k e^{ik(a_0/2)} + d_k^\dagger f_k e^{ik(-a_0)} + e_k^\dagger f_k e^{ik(a_0/2)} H.c
 \end{aligned} \tag{4.9}$$

$$H(k) = [\Phi]^T \begin{bmatrix} 0 & -te^{\frac{ia_0k}{2}} & -te^{-ia_0k} & 0 & 0 & -t \\ -te^{-\frac{ia_0k}{2}} & 0 & -te^{\frac{ia_0k}{2}} & 0 & 0 & 0 \\ -te^{ia_0k} & -te^{-\frac{ia_0k}{2}} & 0 & -t & 0 & 0 \\ 0 & 0 & -t & 0 & -te^{\frac{ia_0k}{2}} & -te^{-ia_0k} \\ 0 & 0 & 0 & -te^{-\frac{ia_0k}{2}} & 0 & -te^{\frac{ia_0k}{2}} \\ -t & 0 & 0 & -te^{ia_0k} & -te^{-\frac{ia_0k}{2}} & 0 \end{bmatrix} [\Phi] \quad (4.10)$$

where

$$\Phi = [a, b, c, d, e, f] \quad (4.11)$$

4.4 Superconductor coupling

To introduce superconducting coupling we will make the couplings on the two edges of the nanoribbon, on the upper edge we will use the coupling on atoms “b”, and for the lower edge we will use the coupling on atoms “e”. Now we can see that we have two kitaev chains, one at the top and one at the bottom. these chains are connected by hopping but not by the superconducting coupling.

The Hamiltonian for this case is described as

$$\begin{aligned} H_{\Delta} = & -\mu \sum_n a_n^{\dagger} a_n + b_n^{\dagger} b_n + c_n^{\dagger} c_n + d_n^{\dagger} d_n + e_n^{\dagger} e_n + f_n^{\dagger} f_n + \\ & \Delta \sum_n b_{n+1/2}^{\dagger} b_{n+1/2+2}^{\dagger} - b_{n+1/2}^{\dagger} b_{n-1/2-1}^{\dagger} + \\ & e_{n+1/2+1}^{\dagger} e_{n+1/2-2}^{\dagger} - e_{n+1/2+1}^{\dagger} e_{n+1/2-2}^{\dagger} + H.c, \end{aligned} \quad (4.12)$$

where now we have a fermionic creation operator (b^{\dagger}) and a hole creation operator (b^{\dagger}) together.

the fourier transform for electrons are

$$c_j = \frac{1}{\sqrt{N}} \sum_k c_k e^{ikR_a} \quad (4.13)$$

the fourier transform for holes are

$$c_j = \frac{1}{\sqrt{N}} \sum_k c_{-k} e^{-ikR_a} \quad (4.14)$$

In the same way that we made an arbitrary case for the bulk, we will make it for this case.

$$\begin{aligned}
\sum_j^N c_j^\dagger c_j^\dagger &= \sum_j \frac{1}{\sqrt{N}} \sum_k c_k^\dagger e^{ik(aj+R_a)} \sum_{k'} \frac{1}{\sqrt{N}} c_{-k'}^\dagger e^{-ik'(aj+R_b)} \\
&= \frac{1}{N} \sum_k \sum_{k'} c_k^\dagger c_{-k'}^\dagger \sum_j e^{ik(aj+R_a)} e^{-ik'(aj+R_b)} \\
&= \sum_k \sum_{k'} c_k^\dagger c_{-k'}^\dagger \frac{1}{N} \sum_j e^{-i(k'-k)aj} e^{i(kR_a)} e^{-i(kR_b)} \\
&= \sum_k \sum_{k'} c_k^\dagger c_{-k'}^\dagger (\delta_{k,k'}) e^{i(k'R_a)} e^{-i(kR_b)} \\
\sum_j^N c_j^\dagger c_j^\dagger &= \sum_k c_k^\dagger c_{-k}^\dagger e^{ik(R_a-R_b)}
\end{aligned} \tag{4.15}$$

R_a and R_b are the positions on the x axis. Now apply Eq.4.15 in the Hamiltonian Eq. 4.12

$$\begin{aligned}
H_\Delta &= \Delta \sum_n b_k^\dagger b_{-k}^\dagger e^{-2ika_0} - b_k^\dagger b_{-k}^\dagger e^{2ika_0} + e_k^\dagger e_{-k}^\dagger e^{-2ika_0} - e_k^\dagger e_{-k}^\dagger e^{2ika_0} + H.c., \\
H_\Delta &= \Delta \sum_n -2i \sin(2a_0k) b_k^\dagger b_{-k}^\dagger - 2i \sin(2a_0k) e_k^\dagger e_{-k}^\dagger + H.c.,
\end{aligned} \tag{4.16}$$

To accommodate the holes, a redundancy must be introduced in the old Hamiltonian Eq.4.16, but now for the hole operators, and the new form of the Hamiltonian is

$$\begin{aligned}
H_t &= \sum_n a_n^\dagger b_{n+1/2} - a_n b_{n+1/2}^\dagger + a_n^\dagger c_{n-1} - a_n c_{n-1}^\dagger + a_n^\dagger f_n - a_n f_n^\dagger \\
&\quad b_{n+1/2}^\dagger c_{n+1} - b_{n+1/2} c_{n+1}^\dagger + \\
&\quad c_{n+1}^\dagger d_{n+1} - c_{n+1} d_{n+1}^\dagger + \\
&\quad d_{n+1}^\dagger f_n - d_{n+1} f_n^\dagger + d_{n+1}^\dagger e_{n+3/2} - d_{n+1} e_{n+3/2}^\dagger + \\
&\quad e_{n+3/2}^\dagger f_{n+2} - e_{n+3/2} f_{n+2}^\dagger + H.c.
\end{aligned} \tag{4.17}$$

in the k space the total Hamiltonian ($H(k)$) is

$$H(k) = H_t(k) + H_\Delta(k) = [\Phi]^T \begin{bmatrix} H(k) & H_\Delta(k) \\ H_\Delta^*(k) & -H^*(-k) \end{bmatrix} [\Phi] \tag{4.18}$$

where

$$\Phi = (a_k, b_k, c_k, d_k, e_k, f_k, a_{-k}^\dagger, b_{-k}^\dagger, c_{-k}^\dagger, d_{-k}^\dagger, e_{-k}^\dagger, f_{-k}^\dagger) \tag{4.19}$$

4.5 Topological Classification and Zak phase topological invariant

The classification of the topological phases of matter is provided by the analysis of fundamental symmetries for a given Hamiltonian in the discrete reciprocal space (77, 79, 119), namely time-reversal ($\mathcal{T}\mathcal{R}$), particle-hole ($\mathcal{P}\mathcal{H}$) or charge conjugation and chiral symmetries (\mathcal{K}).

For the particular case of the spinless penta-silicene nanoribbons (p-SiNRs) with p -wave superconducting pairing at their edges [Eq. (1) of main text], it is verified that both $\mathcal{T}\mathcal{R}$ and $\mathcal{P}\mathcal{H}$ symmetries are preserved, once

$$\mathcal{T}h(k)\mathcal{T}^{-1} = h(-k) \quad (4.20)$$

and

$$\mathcal{C}h(k)\mathcal{C}^{-1} = -h(-k), \quad (4.21)$$

where \mathcal{T} and \mathcal{C} are the time-reversal and charge conjugation operators, respectively, and $h(k)$ is a matrix coming from the Hamiltonian of Eq. (1) in the manuscript, rewritten in the Bogoliubov-de Gennes (BdG) representation, i.e.,

$$\mathcal{H}(k) = \frac{1}{2} \sum_k \Psi_k^\dagger h(k) \Psi_k, \quad (4.22)$$

with

$$\Psi_k \equiv (a_k, a_{-k}^\dagger, b_k, b_{-k}^\dagger, c_k, c_{-k}^\dagger, d_k, d_{-k}^\dagger, e_k, e_{-k}^\dagger, f_k, f_{-k}^\dagger)^T \quad (4.23)$$

being the spinor, which accounts the assumption of $\mathcal{P}\mathcal{H}$ symmetry.

The fulfilment of both $\mathcal{T}\mathcal{R}$ and $\mathcal{P}\mathcal{H}$ symmetries directly implies that the \mathcal{K} symmetry is also preserved (119), meaning that

$$\mathcal{K}h(k)\mathcal{K}^{-1} = -h(k), \quad (4.24)$$

where $\mathcal{K} = \mathcal{T} \cdot \mathcal{C}$ corresponds to the chiral operator. Moreover, from the relations expressed in Eqs. (A.2), (A.4) and (A.6), we obtain $\mathcal{T}^2 = 1$, $\mathcal{C}^2 = 1$ and $\mathcal{K}^2 = 1$, meaning that the BdG Hamiltonian [Eq. (4.22)] of the spinless superconducting p-SiNR [Eq. (1), main text] is a representative of the BDI symmetry class (119), the same class of the well-known Kitaev chain (3).

It is worth mention that spinless superconducting p-SiNR is a simplification which takes into account an ‘‘intrinsic’’ magnetic field. The presence of this field is crucial for inducing the

formation of p -wave superconducting pairing along the nanoribbon edges. However, in practical experimental setups, the source of the spin-polarization is an external magnetic field that naturally breaks the \mathcal{TR} symmetry and hence, \mathcal{K} symmetry. From this argument, the ‘‘artificial’’ \mathcal{TR} symmetry of the spinless model can be neglected, and thus the BdG Hamiltonian of Eq. (4.22) belongs to the D symmetry class (79, 119). Therefore, the p-SiNR in presence of an applied magnetic field is a \mathbb{Z}_2 superconductor in one-dimension (11, 119), once the proposed double-spin Kitaev zigzag nanoribbon configuration can be regarded as two interconnected Kitaev chains with a hopping term (cf. discussion in the main text).

From the previously discussed perspective, the topological and trivial phases of the spinless p -wave superconducting p-SiNR, as described by the BdG Hamiltonian of Eq. (4.22), can be distinguished by the Zak number topological invariant (120)

$$\varphi_{\text{Zak}} = - \int_{-\pi}^{\pi} \frac{dk}{2\pi i} \partial_k \ln [\text{Det}(A(k))]. \quad (4.25)$$

A nonzero quantized Zak phase φ_{Zak} is associated to the emergence of topologically protected edge states, which is an outcome of the conventional bulk-boundary correspondence (77, 119). Specifically, the integer values of φ_{Zak} topological invariant corresponds to the number of topologically protected edge modes present in the system and characterizes its topological phase transitions (TPTs).

To compute the Zak number through Eq. (4.25), it is necessary to obtain a chiral matrix $\mathcal{A}(k)$ associated with $h(k)$, which is performed through the computation of an unitary transformation outlined below:

$$\tilde{h}(k) = \mathcal{U}^\dagger h(k) \mathcal{U} = \begin{bmatrix} 0 & A(k) \\ A^*(k) & 0 \end{bmatrix}, \quad (4.26)$$

bringing $h(k)$ to its chiral form, where

$$A(k) = \begin{bmatrix} 2\mu & 2te^{\frac{ik}{2}} & 2te^{-ik} & 0 & 0 & 2t \\ 2te^{-\frac{ik}{2}} & 2\Phi_k + 2\mu & 2te^{\frac{ik}{2}} & 0 & 0 & 0 \\ 2te^{ik} & 2te^{-\frac{ik}{2}} & 2\mu & 2t & 0 & 0 \\ 0 & 0 & 2t & 2\mu & 2te^{\frac{ik}{2}} & -2te^{-ik} \\ 0 & 0 & 0 & 2te^{-\frac{ik}{2}} & 2\Phi_k + 2\mu & 2te^{\frac{ik}{2}} \\ 2t & 0 & 0 & -2te^{ik} & 2te^{-\frac{ik}{2}} & 2\mu \end{bmatrix}, \quad (4.27)$$

is the chiral matrix, with $\Phi_k = i\Delta \sin(2k)$.

By considering Eq. (4.27) and Eq. (4.25), and employing numerical integration, it becomes feasible to compute the Zak number for several values of chemical potential μ . The ma-

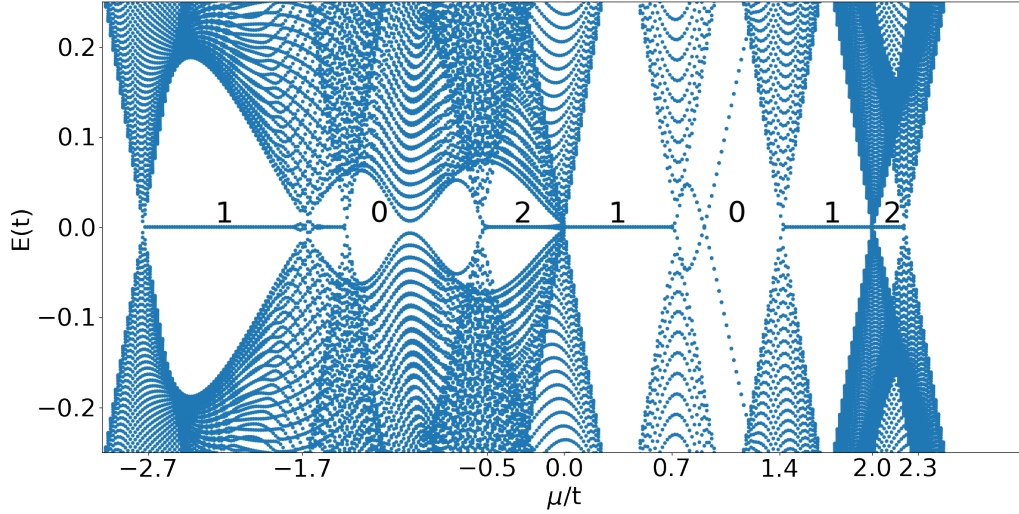


Figure 4.5: Energy dispersion of the bulk system as a function of the chemical potential μ , for the spinless p-SiNR with p -wave superconducting pairing between the atoms localized at the edges, cf. Eq. (1) of the main text. The Zak phase φ_{Zak} , represented by the values 0, 1, and 2, corresponds to the number of MZMs present at the edges of either one or both chains comprising the p-SiNR.

nipulation of μ triggers the closing and subsequent reopening of the superconducting gap, a phenomenon closely related to the TPTs, as discussed in the main text.

In this context, Fig. 4.5 illustrates the Zak number across distinct regions in the bulk energy dispersion of the spinless p -wave superconducting p-SiNR. Notably, a Zak phase of zero corresponds to regions where zero-modes are absent, indicating that the system resides within the topologically trivial phase. Conversely, for $\varphi_{\text{Zak}} \neq 0$, zero-energy modes emerge, indicating the presence of topologically protected Majorana zero modes (MZMs) at the edges of either one ($\varphi_{\text{Zak}} = 1$) or both top/bottom chains ($\varphi_{\text{Zak}} = 2$) of the p-SiNR (17).

4.6 Effective Hamiltonian - spinful case

In order to properly account for the spin degree of freedom in the superconducting p-SiNRs, we follow our previous work (17). We introduce a Zeeman effect due to the application of an external magnetic field perpendicular to the p-SiNRs plane. We also consider a Rashba spin-orbit coupling (RSOC) from an external electric field perpendicular to the chain. Such criterion comes from the fact that our chain is in contact with a substrate that produces a break time-reversal symmetry (121–123).

The Hamiltonian, which accounts for the Zeeman effect, reads:

$$H_z = \sum_{n,\sigma} Z \operatorname{sgn}(\sigma) \left(a_{i,\sigma}^\dagger a_{i,\sigma} + b_{i,\sigma}^\dagger b_{i,\sigma} + c_{i,\sigma}^\dagger c_{i,\sigma} + d_{i,\sigma}^\dagger d_{i,\sigma} + e_{i,\sigma}^\dagger e_{i,\sigma} + f_{i,\sigma}^\dagger f_{i,\sigma} + H.c. \right), \quad (4.28)$$

wherein Z is the effective strength of the Zeeman field and $\sigma = \uparrow, \downarrow$ is the spin index of each operator representing the Si atoms in the p-SiNRs structure.

The extrinsic RSOC induced in the p-SiNRs can be modulated by the action of an external electric field \vec{E} applied perpendicularly to the nanoribbon plane (60, 62, 81, 82). Its corresponding general Hamiltonian reads

$$H_R = \sum_{n,\sigma} i c_{i,\sigma}^\dagger (\vec{u}_{i,j} \cdot \vec{\gamma}) c_{j,\bar{\sigma}} + H.c., \quad (4.29)$$

where $\vec{u}_{i,j} = -\frac{R}{a_0} \hat{k} \times \vec{\delta}_{i,j}$, with R being the extrinsic RSOC parameter, $\vec{\delta}_{i,j}$ is the vector that connects the adjacent lattice sites i and j , $\vec{\gamma}$ the Pauli matrices and $\sigma = \uparrow, \downarrow$, is the spin index for each operator, to the system in the p-SiNRs the Eq. 4.29 turns into

$$\begin{aligned} H_R = \sum_{n,\sigma} & \left(\gamma_1 (a_{n,\sigma}^\dagger b_{n+1/2,\bar{\sigma}}) + \gamma_2 (b_{n+1/2,\sigma}^\dagger a_{n,\bar{\sigma}}) + \right. \\ & (a_{n,\sigma}^\dagger c_{n-1}) - (c_{n-1}^\dagger a_{n,\bar{\sigma}}) + (-i) (a_{n,\sigma}^\dagger f_{n,\bar{\sigma}}) + \\ & (i) (f_{n,\sigma}^\dagger a_{n,\bar{\sigma}}) + \gamma_3 (b_{n+1/2,\sigma}^\dagger c_{n+1,\bar{\sigma}}) + \gamma_4 (c_{n+1,\sigma}^\dagger b_{n+1/2,\bar{\sigma}}) + \\ & (-i) (c_{n+1,\sigma}^\dagger d_{n+1,\bar{\sigma}}) + (i) (d_{n+1,\sigma}^\dagger c_{n+1,\bar{\sigma}}) - (d_{n+1,\sigma}^\dagger f_{n,\bar{\sigma}}) + \\ & (f_{n,\sigma}^\dagger d_{n+1,\bar{\sigma}}) + \gamma_3 (d_{n+1,\sigma}^\dagger e_{n+3/2,\bar{\sigma}}) + \gamma_4 (e_{n+3/2,\sigma}^\dagger d_{n+1,\bar{\sigma}}) + \\ & \left. \gamma_1 (e_{n+3/2,\sigma}^\dagger f_{n+2,\bar{\sigma}}) + \gamma_2 (f_{n+2,\sigma}^\dagger e_{n+3/2,\bar{\sigma}}) + H.c., \right) \end{aligned} \quad (4.30)$$

where $\gamma_1 = \frac{-1}{2} + \frac{i\sqrt{3}}{2}$, $\gamma_2 = \frac{1}{2} - \frac{i\sqrt{3}}{2}$, $\gamma_3 = \frac{-1}{2} - \frac{i\sqrt{3}}{2}$ and $\gamma_4 = \frac{1}{2} + \frac{i\sqrt{3}}{2}$.

Notice that from Eqs. (4.28) and (4.29), we are assuming the external Zeeman field Z perfectly perpendicular to the RSOC, i.e, $Z \equiv Z_\perp \neq 0$ and $Z_\parallel = 0$. In Rashba nanowires setups, this condition is responsible for the vanishing of the induced superconducting gap at zero momentum (inner gap) and the opening of a constant gap at finite momentum (outer gap), which characterizes the topological phase transition and the concomitant emergence of MZMs protected by the outer gap (11).

However, from the experimental perspective, ensuring that the magnetic field is applied only in the perpendicular direction of the RSOC field can be challenging. Then, it is natural to

consider also the effects of $Z_{\parallel} \neq 0$. In this situation, we have both components of the Zeeman field, and the critical magnetic field condition for the topological phase transition remains the same. However, the behavior of the outer gap is not constant anymore, which affects the topological protection of the MZMs towards fault-tolerant quantum computing operations. The effect of Z_{\parallel} in the outer gap is not so detrimental if the RSOC is strong.

It is worth noticing that the limiting case of $Z \equiv Z_{\parallel} \neq 0$ and $Z_{\perp} = 0$ can lead to the vanishing of the outer gap, hence preventing the topological phase and emergence of MZMs. Therefore, since our system is qualitatively described by the similar underlying physics of Rashba nanowires, it is appropriate to experimentally ensure the dominance of the magnetic field component perpendicular to the Rashba field.

Considering also the spin degree of freedom on both H_t and H_{Δ} [Eqs. (4.2) and 4.12)], we now can define the total system Hamiltonian as

$$H_{\text{total}} = H_t + H_Z + H_R + H_{\Delta}, \quad (4.31)$$

which can be written in the corresponding Bogolyubov-de Gennes (BdG) form in k -space as $H_{\text{total}}(k) = \Phi^T H_{\text{BdG}}(k) \Phi$, with

$$H_{\text{BdG}}(k) = \begin{bmatrix} H_{\uparrow,\uparrow}(k) & H_{\uparrow,\downarrow}(k) & H_{\Delta,\uparrow,\uparrow}(k) & H_{\Delta,\uparrow,\downarrow}(k) \\ H_{\uparrow,\downarrow}(k) & H_{\downarrow,\downarrow}(k) & H_{\Delta,\downarrow,\uparrow}(k) & H_{\Delta,\downarrow,\downarrow}(k) \\ H_{\Delta,\uparrow,\uparrow}^*(-k) & H_{\Delta,\uparrow,\downarrow}^*(-k) & H_{\uparrow,\uparrow}^*(-k) & H_{\uparrow,\downarrow}^*(-k) \\ H_{\Delta,\downarrow,\uparrow}^*(-k) & H_{\Delta,\downarrow,\downarrow}^*(-k) & H_{\downarrow,\uparrow}^*(-k) & H_{\downarrow,\downarrow}^*(-k) \end{bmatrix}, \quad (4.32)$$

where $H_{\sigma,\sigma'}(\pm k)$ and $H_{\Delta,\sigma,\sigma'}(\pm k)$ represent the matrix elements for different spin directions and the matrix elements corresponding to the part of the matrix where superconducting couplings Δ appear, respectively. The spinor Φ was constructed with the fermionic operators in the following order:

$$\begin{aligned} \Phi^T = & (a_{k,\uparrow}, b_{k,\uparrow}, c_{k,\uparrow}, d_{k,\uparrow}, e_{k,\uparrow}, f_{k,\uparrow}, \\ & a_{k,\downarrow}, b_{k,\downarrow}, c_{k,\downarrow}, d_{k,\downarrow}, e_{k,\downarrow}, f_{k,\downarrow}, \\ & a_{-k,\uparrow}^{\dagger}, b_{-k,\uparrow}^{\dagger}, c_{-k,\uparrow}^{\dagger}, d_{-k,\uparrow}^{\dagger}, e_{-k,\uparrow}^{\dagger}, f_{-k,\uparrow}^{\dagger}, \\ & a_{-k,\downarrow}^{\dagger}, b_{-k,\downarrow}^{\dagger}, c_{-k,\downarrow}^{\dagger}, d_{-k,\downarrow}^{\dagger}, e_{-k,\downarrow}^{\dagger}, f_{-k,\downarrow}^{\dagger}). \end{aligned} \quad (4.33)$$

The spin alignment for each situation in the next section is computed numerically. We calculate the mean value of the Pauli matrix in \hat{z} direction \hat{S}_z , i.e., $\langle \hat{S}_z \rangle = \langle \Psi | \hat{S}_z | \Psi \rangle$, where $|\Psi\rangle$ are the eigenvectors of the total Hamiltonian given by Eq. (4.31).

In hybrid semiconducting-superconducting nanowires, sometimes dubbed Majorana nanowires, the following features strongly suggest the emergence of MZMs at the nanowire

ends (11):

- (a) Closing and subsequent reopening of the superconducting gap in the bulk relation dispersion as the chemical potential μ changes, indicating a topological phase transition (TPT).
- (b) Emergence of persistent zero-modes for specific system parameter values associated with nonoverlapping wave functions localized at the opposite ends of the nanowire.

To investigate the possibility of MZMs in the p-SiNRs, we will analyze the energy spectrum as a function of the chemical potential μ . Initially, we will consider the simplest case of a spinless p-SiNRs with finite size $N = 100$, given by the Hamiltonian of Eq. (4.1); the bulk band structure and the probability density function associated with the zero-energy states which arise in the system energy spectrum.

Both the energies E_n and eigenvectors ψ_n per site are obtained by numerically solving the Schrödinger equation $H\psi_n = E_n\psi_n$ for the Hamiltonian of Eq. (4.1). To evaluate the position dependence of the wave functions associated with zero energy states, we numerically calculate the eigenvector ψ_n when $E_n = 0$, which allows obtaining the probability density per lattice site according to

$$|\psi_n|^2 = \psi_n \psi_n^*. \quad (4.34)$$

4.7 Finite spinless p-SiNRs

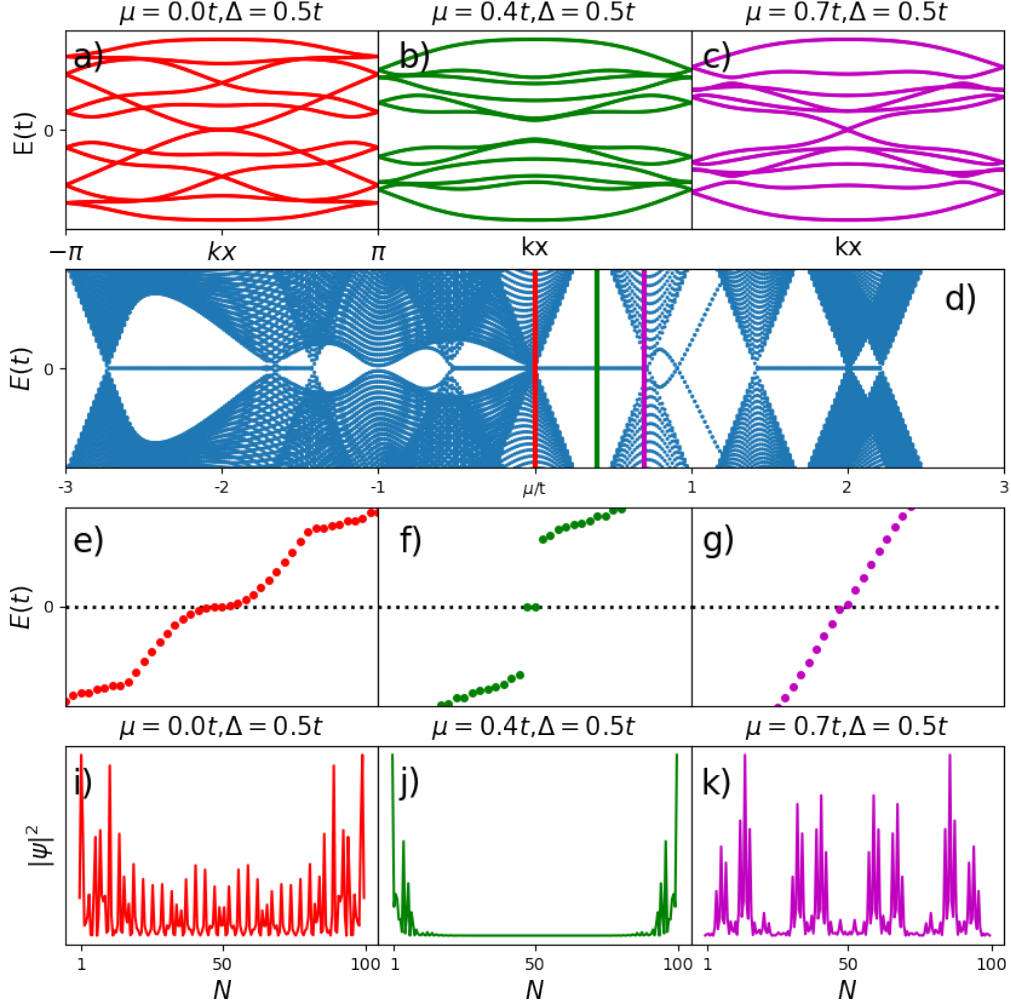


Figure 4.6: (Color online) Spinless case: (a)-(c) Bulk energy dispersion for the spinless p-SiNRs as a function of k_x , for $\mu = 0.0t, 0.4t$, and $0.7t$, respectively. (d) Energy spectrum as a function of the chemical potential. Vertical lines indicate the chosen values of chemical potential shown on top Figs. (e)-(g) The energy spectrum with labels the energy levels in increasing order for $\mu = 0.0t, 0.4t$, and $0.7t$, respectively. (i)-(k) Probability density [Eq. (4.34)] associated with zero-energy states, as a function of the lattice site $N = 1 \dots 100$.

In all the calculations we employed the following parameter set: $\Delta = 0.5t, t = 1, Z = 0.1t$, and $R = 0.05t$. The top Figs of Fig. 4.6 show the bulk energy dispersion of the p-SiNRs in the presence of the superconducting p -wave pairing described by Eq. (4.1), along the k_x direction, for three representative values of chemical potential μ [vertical arrows in Fig (d)]. Fig.4.6(a) depicts the closing of the SC gap at $k_x = 0$ for $\mu = 0.0t$. As the value of μ enhances, the SC

gap opens and closes again at $k_x = 0$, as shown in Figs (b) and (c), where $\mu = 0.4t$ and $\mu = 0.7t$, respectively. This closing and reopening of the SC gap with the tuning of μ characterize a topological phase transition. The bulk-boundary correspondence principle (80) ensures the topologically protected MZMs at the ends of the p-SiNRs.

To verify the emergence of MZMs associated with the topological phase transition depicted in Fig. 4.6(a)-(c), in Fig. 4.6(d), we plot the p-SiNRs energy spectrum as a function of μ . There is no zero-energy mode for the values of μ where the gap closes (red and magenta vertical lines). However, when $\mu = 0.4t$ (green vertical line), a zero-energy state arises, indicating the presence of MZMs at the opposite ends of the p-SiNRs, topologically protected by the effective p -wave SC gap [Fig. 4.6(b)]. This finding is similar to what was obtained in our previous work (17), wherein the MZMs emerge at the opposite ends of a finite double zigzag honeycomb nanoribbon.

Fig. 4.6(f) shows isolated zero-energy modes for $\mu = 0.4t$, which are associated with a nonoverlapping wave function, well-localized at the ends of the p-SiNRs, as depicted in Fig. 4.6(j); which together with the topological phase transition [Fig. 4.6(a)-(c)], is a piece of strong evidence that topologically protected MZMs emerge at the opposite ends of the spinless p-SiNRs. In the Supplemental Material (SM), we developed an extensive analysis of the topological and trivial phases of the spinless p -wave superconducting p-SiNR, that can be distinguished by the Zak number topological invariant (120). However, due to the extreme mathematical complexity, we cannot afford to do the same study for the spinful case.

Although there are zero-energy modes for other values of μ [Fig. 4.6(e) and (g)], they are not associated with wave functions well-localized at the ends of the system, as can be seen in Figs. 4.6(i) and (k), for $\mu = 0.0t$ and $\mu = 0.7t$, respectively.

We also highlight that we analyze only one representative region of all energy spectrum shown in Figs. 4.6(d), which presents other ranges of chemical potentials wherein a zero-energy state, associated with the emergence of MZMs, arises. We can also observe that, unlike the system of our previous work (17), the energy spectrum of Figs. 4.6(d) is asymmetric at about $\mu = 0$.

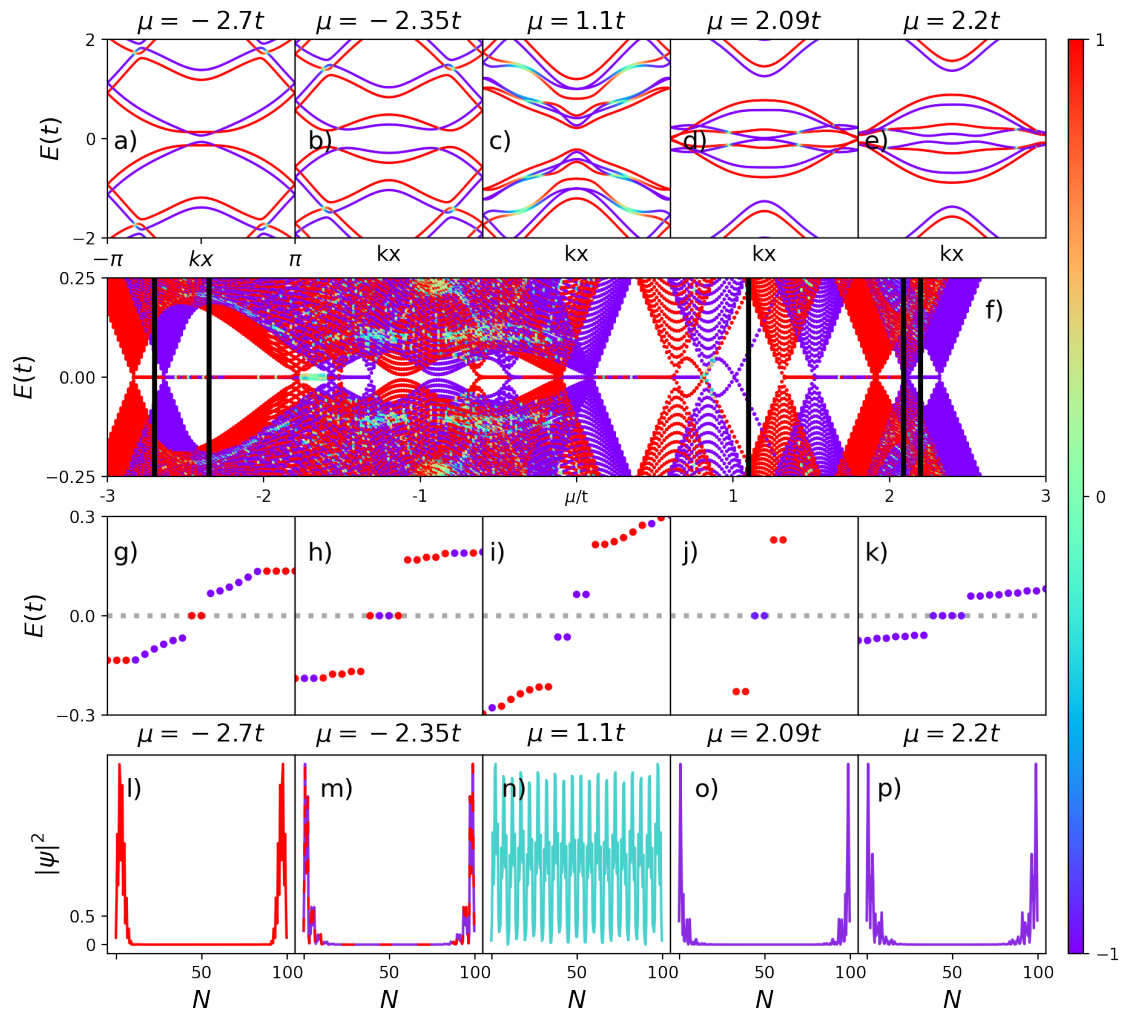


Figure 4.7: (Color online) Spinful case - Magnetic field up: (a)-(e) Bulk energy dispersion of the superconducting p-SiNRs for the spinful situation, as a function of k_x , for $\mu = -2.7t$, $-2.35t$, $1.1t$, $2.09t$ and $2.2t$, respectively. (f) Energy spectrum as a function of the chemical potential. Vertical lines indicate the chosen values of chemical potential shown on top Figs. (g)-(k) Energy levels sorted in ascending order, respectively. (l)-(p) Probability density [Eq. (4.34)] associated with zero-energy states, as a function of the lattice site $N = 1 \dots 100$.

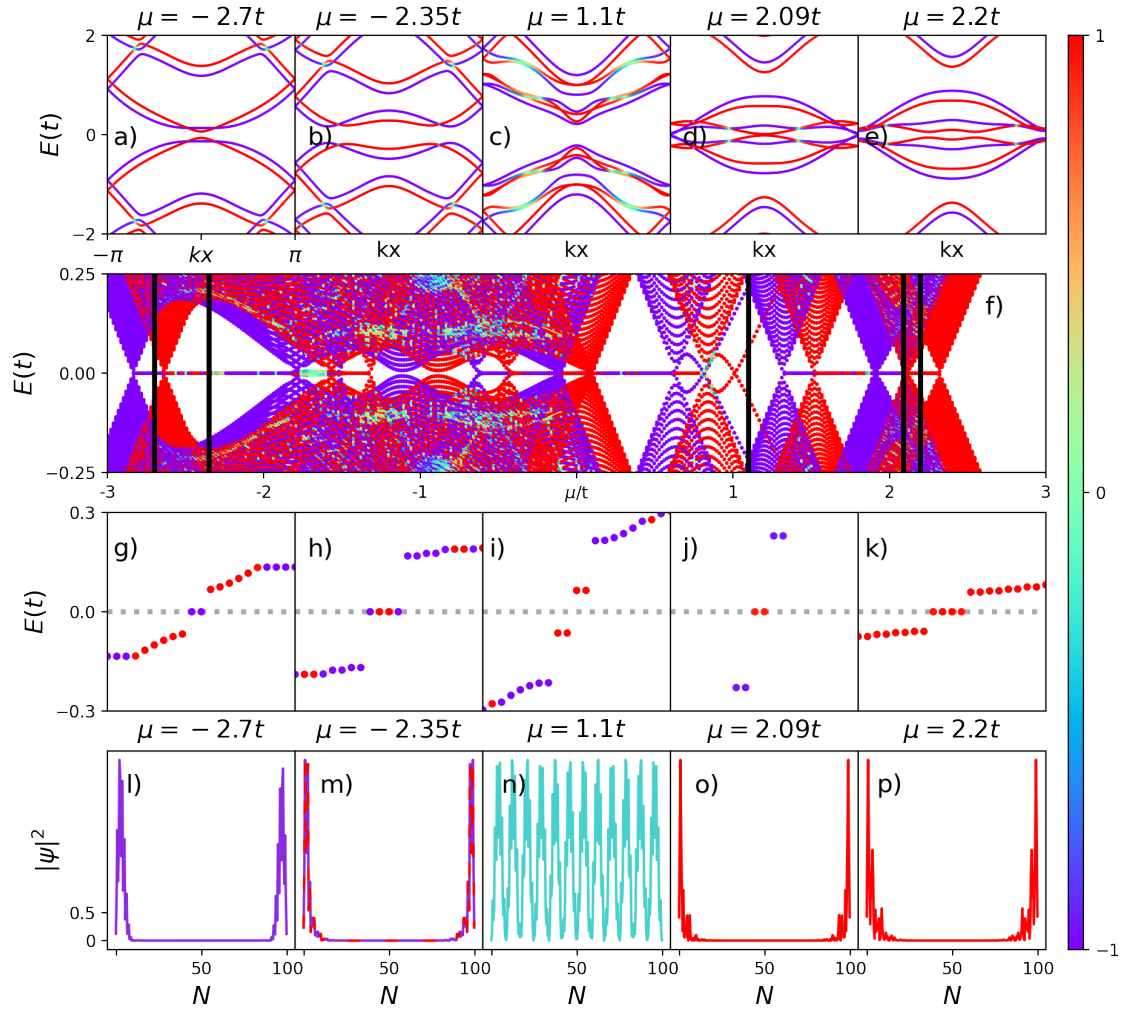


Figure 4.8: (Color online) Spinful case - Magnetic field down: The same situation of Fig. 4.7 but with the magnetic field pointing in the opposed direction.

4.8 Finite spinful p-SiNRs

Now we will analyze how the spinless scenario shown in Fig. 4.6 is affected by the presence of both Zeeman field [Eq. (4.28)] and extrinsic RSOC [Eq. (4.29)] coupling within the spinful description [Eq. (4.31)]. In the following, we have adopted the strength of the magnetic field $Z = 0.1t$ and the intensity of the RSOC, $R = 0.05t$.

Figs. 4.7(a)-(e) exhibit the energy dispersion of the p-SiNRs given by the eigenenergies of BdG Hamiltonian [Eq. (4.32)] as a function of k_x , for distinct values of the chemical potential μ , indicated by vertical lines in Fig. 4.7(f). The spin polarization is indicated by the vertical color

bar, in which the red color represents the spin $\uparrow = 1$, while the blue color stands for spin $\downarrow = -1$, and the light shades of colors mean the spin is neither up nor down. As μ is tuned, we can see the opening and closing of the superconducting gap, thus indicating a TPT, as previously verified in the spinless situation [Fig. 4.6(a)-(c)]. However, here we can notice that each TPT associated with a specific value of μ has a preferential spin orientation, except Fig 4.7(c), where the system exhibits a conventional band gap.

The spin-polarized TPTs in Figs. 4.7(a),(b),(d), and (e) lead to the appearance of spin-polarized zero-modes in Fig. 4.7(f), which shows the system energy spectrum as a function of μ . These zero-modes indicate the emergence of spin-polarized MZMs at the ends of the p-SiNRs as μ is changed, similar to those found in (17).

The Figs (g)-(k) of Fig. 4.7 depict the corresponding energy levels sorted in ascending order, respectively; the different values of μ used to calculate the MZMs are indicated by vertical black lines in Fig. 4.7(f). For $\mu = -2.7t$ [Fig. 4.7(g)], there are two zero modes on the real axis of spin up (red points), associated with nonoverlapping wave functions shown in Fig. 4.7(l). For $\mu = -2.35t$ [Fig. 4.7(h)], there are two energy-states in the spin-up direction and other two with spin-down, associated with degenerate (blue and red) nonoverlapping wave functions shown in Fig. 4.7(m). For $\mu = 1.1t$ [Fig. 4.7(h)], there are four spin-down energy states outside the real axis, there are no MZMs, and the wave functions completely overlap along the ribbon. For $\mu = 2.09t$ [Fig. 4.7(j)], there are two zero modes on the real axis of spin up (red points). Finally, for $\mu = 2.2t$ [Fig. 4.7(k)], there are four MZMs with spin-down energy states on the real axis. This situation happens because, at $\mu = 2.09t$, a TPT occurs for spin-up, the gap closes at $k = \pm\pi$, and for $\mu > 2.09t$ the gap defines a trivial band insulator and MZMs with spin-up are not available anymore. These well-localized probability densities describing wave functions centered at the opposite ends of the superconducting p-SiNRs, associated with zero-energy edge states, indicate the emergence of MZMs in the same way previously found for the spinless system.

Fig. 4.8 represents the same situation as Fig. 4.7 but with the magnetic field pointing in the opposite direction. The net effect on the p-SiNRs is to change the MZMs, for all μ values, in spin up to down and vice versa. Therefore, it is possible to select the spin polarization of the MZMs by changing the chemical potential μ or the magnetic field.

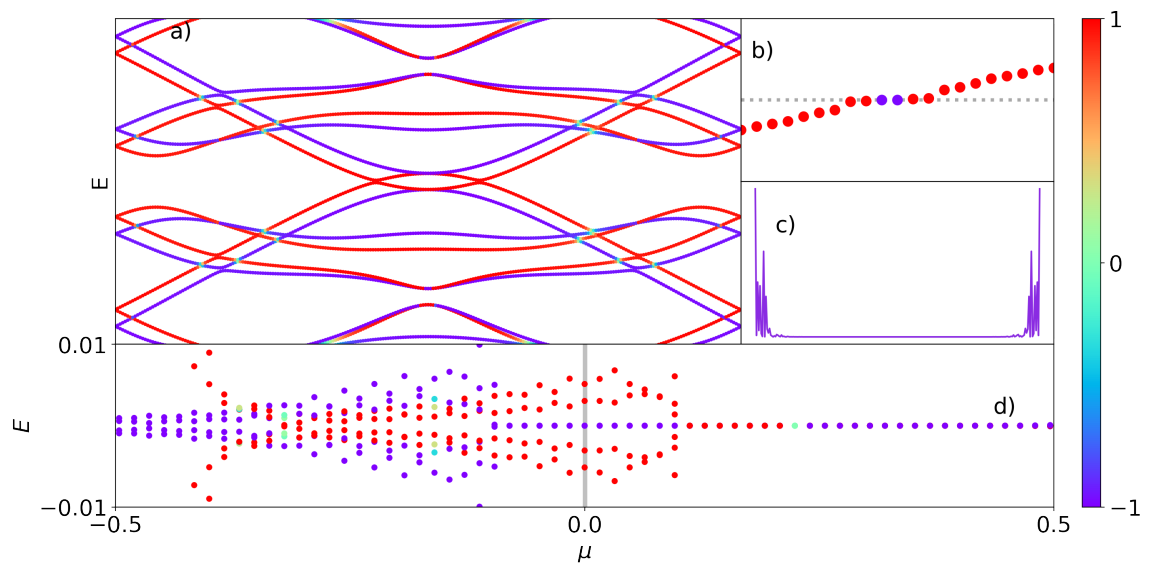


Figure 4.9: (Color online) Analysis in detail of the $\mu = 0$ case of Fig. 4.7 with the magnetic field pointing in the up direction.

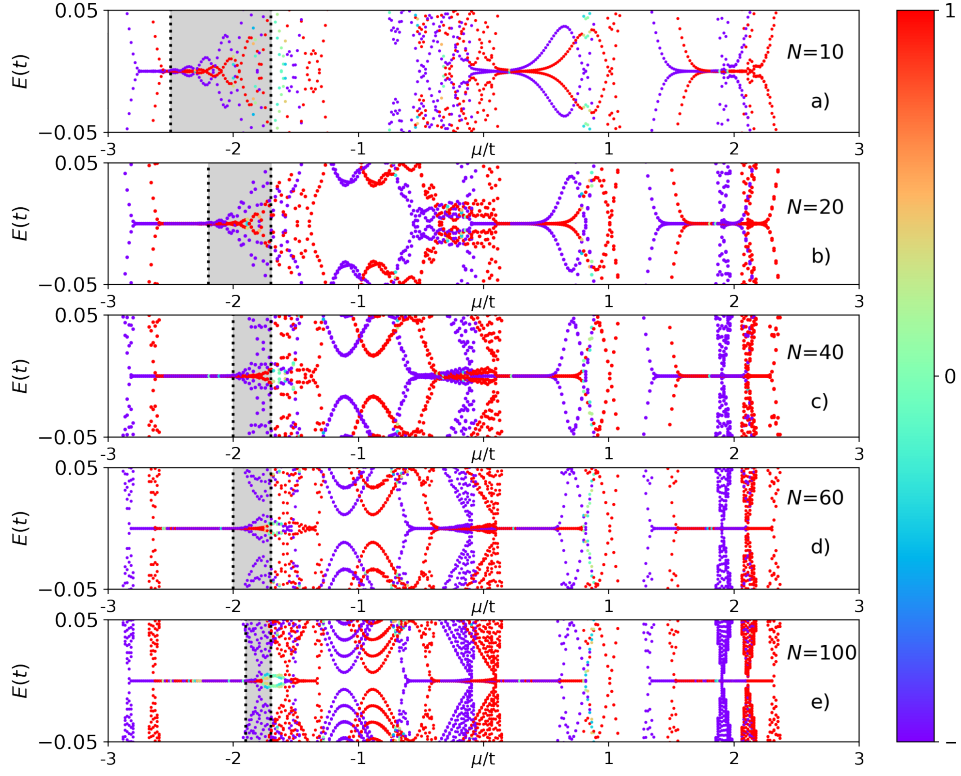


Figure 4.10: (Color online) Energy spectrum as a function of the chemical potential μ , for distinct lengths of superconducting p-SiNRs N , namely, for $N = 10$ (a), $N = 20$ (b), $N = 40$ (c), $N = 60$ (d) and $N = 100$ (e).

In Fig. 4.9, we mainly analyze the dispersion relation, energy spectrum, and nature of the zero-modes at $\mu = 0$ of Fig. 4.7, with the magnetic field pointing in the up direction. Fig. 4.9(a) depicts $E(k)$ as a function of k_x , showing that there is a finite topological superconducting gap only for the spin-down orientation (blue line), while the spin-up (red line) remains gapless. This behavior suggests a spin-polarized TPT at zero chemical potential, implying that only the system spin-down component is within the topological regime. At the same time, the spin-up belongs to a metallic phase. Fig. 4.9(b),(c) represent two MZMs of spin-down with its correspondent nonoverlapped wave function, respectively, and Fig. 4.9(d), shows detail at around $\mu = 0$ region.

We also investigate how the energy spectrum as a function of μ is affected by the length of the p-SiNRs. Fig. 4.10 exhibits the energy spectrum of the superconducting p-SiNRs for increasing values of nanoribbon length N . From the smallest system considered [$N = 10$, Fig. 4.10(a)] to the largest one [$N = 100$, Fig. 4.10(e)], it can be noticed a decrease of the amplitude of os-

cillations at around the real axis ($E = 0$), and at the same time the definition of the MZMs on the real axis improves as N increases, and for $N = 100$ the MZMs are well defined in all the real axis. It should be mentioned that these oscillations around zero energy are expected for short Majorana nanowires due to the overlap between Majorana wavefunctions of opposite ends. Therefore, such oscillations are expected to decrease as the system becomes larger. The same behavior was verified in our previous work (17).

4.9 Conclusions and Perspectives

In this work, we demonstrate the emergence of topologically protected MZMs at opposite ends of both spinless and spinful p-SiNRs with p -wave superconducting pairing. These MZMs exhibit spin discrimination, and their polarization can be controlled by adjusting the nanoribbon chemical potential or applied magnetic field. To implement our findings experimentally, we propose a material engineering of p-SiNRs grown over a Ag(110) surface [cf. Fig. 4.1(a)], with a thin Pb film deposited on top (105, 117). In this device, the proximity effect will enable the penetration of Cooper pairs from the Pb s -wave superconductor into the p-SiNRs (11), and in combination with an external magnetic field and the inherent strong RSOC of Pb, it will induce p -wave pairing in the buckled atoms of the double p-SiNRs structure [cf. Fig. 4.1(d)]. In the end, the underlying mechanism driving p -wave induced pairing is similar to that reported in one-dimensional chains of magnetic atoms on the surface of a superconductor, through the formation of Shiba states (40, 118).

We should highlight the potential applications driven by the spin-polarized MZMs presented in this work, particularly demonstrated in Figs. 4.7 and 4.8. When two MZMs appear at opposite ends of the p-SiNR with either a spin up or down orientation, the reverse spin component exhibits metallic behavior. In other words, one spin component (e.g., up) is associated with MZMs, while the opposite component (down) displays metallic features, resulting in a half-metallic behavior for the system (63, 65). This property harnessed to design a kind of single Majorana transistor (SMT), built up from a quantum dot (QD) sandwiched by a finite proximitized p-SiNR leads. This setup bears resemblance to the conventional single electron transistor (SET) (107) [**Please, also insert some Ref regarding to SET, with leads made by graphene nanoribbons, for instance**]. The SMT can serve as a valuable tool for discerning between MZMs and trivial Andreev bound states (38, 42). Particularly, the leakage of MZMs through the QD (124), along with both local and crossed Andreev reflections induced by a specific spin orientation within the p-SiNR-QD-p-SiNR SMT structure, is expected to generate distinct electronic transport signatures, enabling the identification of MZMs.

In addition to the spin-polarization of MZMs, our proposal also features the emergence of four MZMs at the ends of the p-SiNR, as illustrated in Figs. 4.7(h,k) and 4.8(h,k). Two MZMs are located at opposite ends of the top chain, while another two are situated at the bottom chain. These MZMs can exhibit either the same or opposite spin orientations, depending on the chemical potential and applied magnetic field orientation. Having four MZMs, at least, is crucial for implementing quantum computing operations between two qubits, as it requires the presence of two fermionic sites, i.e., four MZMs (101, 103). Therefore, our proposal naturally lends itself as a promising candidate for realizing hybrid quantum computing operations (72, 73) between conventional qubits and spin-polarized Majorana-based qubits. This paves the way for defining quantum computing operations using Majorana spintronics (125).

Capítulo 5

CONCLUSION

In conclusion, this thesis focused on the exploration of quasi-two-dimensional materials, investigating their theoretical and experimental aspects with a particular focus on topological properties.

The first model presented was the Su-Schrieffer-Heeger (SSH), followed by the Rice-Mele model and the Kitaev chain. These models allowed us to study topological phases, electronic properties, localized zero-energy states, and Majorana zero-energy states.

The application of external magnetic fields to break spin degeneracy brought a new dimension to the study, changing energy levels and leading to the emergence of spin-polarized Majorana fermions in zigzag honeycomb-shaped nanoribbons. The link between topological transitions and the appearance of these zero-energy modes was one of the main aspects studied in Chapter 3.

Furthermore, our research achieved zero Majorana modes with spin degeneracy breaking in zigzag double honeycomb nanoribbons (KzHNRs), as shown in Chapter 3 we obtained the modes in the energy spectrum and hints of the phase transitions in the band structure, as well as the topological indices of the system were calculated in several parameters.

The next topic covered was silicene-based structures, such as penta-silicene nanoribbons, offered a unique platform for the study of fermions and Majorana topological states. We have shown that, besides being a different structure from the honeycomb, it does not have certain symmetries in real space, thus having new effects not foreseen in previous work.

In the context of quantum computing, silicon nanowires with topological properties have potential, albeit with continued challenges in demonstrating topologically protected MZMs. The quest to experimentally manifest the Kitaev model on a silicon-based platform continues.

In the chapters of this thesis, we studied fundamental topological models to nanoribbon models, each contributing new approaches to the field. As we synthesize our findings, we

recognize the transformative potential of zero modes and topological Majorana phases, not just in quantum computing.

To conclude, this thesis highlights that there are still many other properties of quasi two-dimensional materials and topological phenomena. We hope that our work inspires further research, innovation and experimentation in this field.

The main results of this thesis appeared in two publications:

- 1) Spin-polarized Majorana zero-modes in double zigzag honeycomb nanoribbons (17).
- 2) Spin-polarized Majorana zero modes in proximitized superconducting penta-silicene nanoribbons (126).

Apendice A

STEP-BY-STEP EXPLANATION OF THE CHIRAL MATRIX CALCULATION

In this chapter, we will provide a detailed explanation of how to calculate the topological invariant shown in Chapter 3. The first step is to represent the matrix in the k-space in its matrix form

The Hamiltonian $H(k)$ for this system has been formulated as an 8x8 matrix, which reads as

$$H(k) = \begin{pmatrix} -2\mu & \Delta_k & -\varepsilon & 0 & 0 & 0 & 0 & 0 \\ \Delta_k^* & +2\mu & 0 & \varepsilon & 0 & 0 & 0 & 0 \\ -\varepsilon & 0 & -2\mu & \Delta_k & -t & 0 & 0 & 0 \\ 0 & \varepsilon & \Delta_k^* & +2\mu & 0 & t & 0 & 0 \\ 0 & 0 & -t & 0 & -2\mu & \Delta_k & -\varepsilon & 0 \\ 0 & 0 & 0 & t & \Delta_k^* & +2\mu & 0 & \varepsilon \\ 0 & 0 & 0 & 0 & -\varepsilon & 0 & -2\mu & \Delta_k \\ 0 & 0 & 0 & 0 & 0 & \varepsilon & \Delta_k^* & +2\mu \end{pmatrix}. \quad (\text{A.1})$$

Its basis is written in the following order:

$$\Psi \equiv \left(a_1, a_1^\dagger, b_1, b_1^\dagger, a_2, a_2^\dagger, b_2, b_2^\dagger \right)$$

Now we will present the main properties of symmetries and their characteristics. The first matrix we will introduce is the time-reversal symmetry, which has the following properties: A Hamiltonian with time-reversal symmetry satisfies

$$TH(k)T^{-1} = H(-k), \quad (\text{A.2})$$

And T is a unitary matrix

$$T^2 = \pm \mathbb{1} \quad (\text{A.3})$$

Next is the particle-hole symmetry matrix, which has the following properties:

It anti-commutes with the matrix $H(k)$ if $H(k)$ satisfies particle-hole symmetry as follows:

$$CH(k)C^{-1} = -H(-k), \quad (\text{A.4})$$

And C is a unitary matrix

$$C^2 = \pm \mathbb{1} \quad (\text{A.5})$$

Finally, we have the chiral matrix, which, if the matrix $H(k)$ possesses this symmetry, anti-commutes as follows.

$$KH(k)K^{-1} = -H(k), \quad (\text{A.6})$$

And K is a unitary matrix

$$K^2 = \mathbb{1} \quad (\text{A.7})$$

If we have two of these three symmetries present, then the third is also present, due to the relation $K=TC$

To proceed with this calculation, we will start by trying to find the K matrix because, by construction, the $H(k)$ matrix is built with the particle-hole symmetry matrix, so we already know that it is satisfied.

Since we do not know the form of the K matrix, we'll rewrite the equation in a different way, like this:

$$KH(k)K^{-1} = -H(k), \quad (\text{A.8})$$

$$KH(k)K^{-1}K = -H(k)K, \quad (\text{A.9})$$

$$(\text{A.10})$$

Using $K^2 = \mathbb{1} = K^{-1}K = \mathbb{1}$

$$\{H, K\} = HK(k) + KH(k) = 0, \quad (\text{A.11})$$

Now, with this form, we can see that we need both the H(k) matrix and the K matrix to perform the calculation.

Given these conditions, when we work with a generic Hermitian matrix, we can represent the matrix K as:

$$K = \begin{pmatrix} a_1 & a_2 & a_3 & a_4 & a_5 & a_6 & a_7 & a_8 \\ \bar{a}_2 & b_1 & b_2 & b_3 & b_4 & b_5 & b_6 & b_7 \\ \bar{a}_3 & \bar{b}_2 & c_1 & c_2 & c_3 & c_4 & c_5 & c_6 \\ \bar{a}_4 & \bar{b}_3 & \bar{c}_2 & d_1 & d_2 & d_3 & d_4 & d_5 \\ \bar{a}_5 & \bar{b}_4 & \bar{c}_3 & \bar{d}_2 & e_1 & e_2 & e_3 & e_4 \\ \bar{a}_6 & \bar{b}_5 & \bar{c}_4 & \bar{d}_3 & \bar{e}_2 & f_1 & f_2 & f_3 \\ \bar{a}_7 & \bar{b}_6 & \bar{c}_5 & \bar{d}_4 & \bar{e}_3 & \bar{f}_2 & g_1 & g_2 \\ \bar{a}_8 & \bar{b}_7 & \bar{c}_6 & \bar{d}_5 & \bar{e}_4 & \bar{f}_3 & \bar{g}_2 & h_1 \end{pmatrix} \quad (\text{A.12})$$

Now, by performing this anticommutation with the generic K matrix, we can typically express this system in the form $Ax = b$, which allows us to find the resulting solution.

In this way, we have created a Python program to calculate the elements of K, which are in the form of N linear equations.

$$\begin{aligned} a_1 = 0, a_2 = g_2, a_3 = 0, a_4 = 0, a_5 = 0, a_6 = e_2 - g_2, a_7 = 0, a_8 = 0, \\ b_1 = 0, b_2 = 0, b_3 = 0, b_4 = e_2 - g_2, b_5 = 0, b_6 = 0, b_7 = 0, c_1 = 0, c_2 = e_2, c_3 = 0, \\ c_4 = 0, c_5 = 0, c_6 = e_2 - g_2, d_1 = 0, d_2 = 0, d_3 = 0, d_4 = e_2 - g_2, d_5 = 0, \\ e_1 = 0, e_3 = 0, e_4 = 0, f_1 = 0, f_2 = 0, f_3 = 0, g_1 = 0, h_1 = 0 \end{aligned} \quad (\text{A.13})$$

When substituting the given values $e_2 = g_2 = 1$, the matrix K takes the following form:

$$K = \begin{bmatrix} 0 & 1 & 0 & 0 & 0 & 0 & 0 & 0 \\ 1 & 0 & 0 & 0 & 0 & 0 & 0 & 0 \\ 0 & 0 & 0 & 1 & 0 & 0 & 0 & 0 \\ 0 & 0 & 1 & 0 & 0 & 0 & 0 & 0 \\ 0 & 0 & 0 & 0 & 0 & 1 & 0 & 0 \\ 0 & 0 & 0 & 0 & 1 & 0 & 0 & 0 \\ 0 & 0 & 0 & 0 & 0 & 0 & 0 & 1 \\ 0 & 0 & 0 & 0 & 0 & 0 & 1 & 0 \end{bmatrix} \quad (\text{A.14})$$

This matrix K also satisfies the condition:

$$K^2 = \begin{bmatrix} 1 & 0 & 0 & 0 & 0 & 0 & 0 & 0 \\ 0 & 1 & 0 & 0 & 0 & 0 & 0 & 0 \\ 0 & 0 & 1 & 0 & 0 & 0 & 0 & 0 \\ 0 & 0 & 0 & 1 & 0 & 0 & 0 & 0 \\ 0 & 0 & 0 & 0 & 1 & 0 & 0 & 0 \\ 0 & 0 & 0 & 0 & 0 & 1 & 0 & 0 \\ 0 & 0 & 0 & 0 & 0 & 0 & 1 & 0 \\ 0 & 0 & 0 & 0 & 0 & 0 & 0 & 1 \end{bmatrix} = \mathbb{1} \quad (\text{A.15})$$

Now that we have this matrix, our next objective is to find its eigenvectors. Identifying the eigenvectors will be crucial for building the change of basis matrix U . From this point on, all calculations were performed using Python.

$$\lambda = \left(\begin{array}{c} \begin{bmatrix} -1 \\ 1 \\ 0 \\ 0 \\ 0 \\ 0 \\ 0 \\ 0 \end{bmatrix}, \begin{bmatrix} 0 \\ 0 \\ -1 \\ 1 \\ 0 \\ 0 \\ 0 \\ 0 \end{bmatrix}, \begin{bmatrix} 0 \\ 0 \\ 0 \\ 0 \\ -1 \\ 1 \\ 0 \\ 0 \end{bmatrix}, \begin{bmatrix} 0 \\ 0 \\ 0 \\ 0 \\ 0 \\ -1 \\ 1 \\ 0 \end{bmatrix}, \\ \begin{bmatrix} 1 \\ 1 \\ 0 \\ 0 \\ 0 \\ 0 \\ 0 \\ 0 \end{bmatrix}, \begin{bmatrix} 0 \\ 0 \\ 1 \\ 1 \\ 0 \\ 0 \\ 0 \\ 0 \end{bmatrix}, \begin{bmatrix} 0 \\ 0 \\ 0 \\ 0 \\ 1 \\ 1 \\ 0 \\ 0 \end{bmatrix}, \begin{bmatrix} 0 \\ 0 \\ 0 \\ 0 \\ 0 \\ 0 \\ 1 \\ 1 \end{bmatrix} \end{array} \right) \quad (\text{A.16})$$

Each eigenvector λ is a column of the matrix U , hence U is given by:

$$U = \begin{bmatrix} -1 & 0 & 0 & 0 & 1 & 0 & 0 & 0 \\ 1 & 0 & 0 & 0 & 1 & 0 & 0 & 0 \\ 0 & -1 & 0 & 0 & 0 & 1 & 0 & 0 \\ 0 & 1 & 0 & 0 & 0 & 1 & 0 & 0 \\ 0 & 0 & -1 & 0 & 0 & 0 & 1 & 0 \\ 0 & 0 & 1 & 0 & 0 & 0 & 1 & 0 \\ 0 & 0 & 0 & -1 & 0 & 0 & 0 & 1 \\ 0 & 0 & 0 & 1 & 0 & 0 & 0 & 1 \end{bmatrix} \quad (\text{A.17})$$

To obtain the matrix $H(k)$ in the new basis $\tilde{H}(k)$:

$$\tilde{H}(k) = U^\dagger H(k) U \quad (\text{A.18})$$

$$\tilde{H}(K) = \begin{bmatrix} 0 & A(k) \\ A(k)^* & 0 \end{bmatrix} \quad (\text{A.19})$$

where

$$A(k) = \begin{bmatrix} -4i\Delta \sin(k) + 4\mu & -4t \cos\left(\frac{k}{2}\right) & 0 & 0 \\ -4t \cos\left(\frac{k}{2}\right) & -4i\Delta \sin(k) + 4\mu & 2t & 0 \\ 0 & 2t & -4i\Delta \sin(k) + 4\mu & -4t \cos\left(\frac{k}{2}\right) \\ 0 & 0 & -4t \cos\left(\frac{k}{2}\right) & -4i\Delta \sin(k) + 4\mu \end{bmatrix} \quad (\text{A.20})$$

$$\Delta_k = i2\Delta \sin(k_x), \quad (\text{A.21})$$

$$\varepsilon = -2t \cos(k_x/2), \quad (\text{A.22})$$

and $A(k)$ is the 4x4 matrix: The Chern number invariant can be calculated by the integration:

$$W = \text{Tr} \int_{-\pi}^{\pi} \frac{dk}{2\pi i} A_k^{-1} \partial_k A_k \quad (\text{A.23})$$

$$= - \int_{-\pi}^{\pi} \frac{dk}{2\pi i} \partial_k \ln(\text{Det}(A_k)) \quad (\text{A.24})$$

$$= - \int_{-\pi}^{\pi} \frac{dk}{2\pi i} \partial_k \ln(\lambda(\text{Det}(A_K))) \quad (\text{A.25})$$

$$= - \int_{-\pi}^{\pi} \frac{dk}{2\pi i} (\partial_k \ln(\lambda) + \partial_k \ln(\text{Det}(A_K))) \quad (\text{A.26})$$

REFERÊNCIAS

- 1 SHENG, S. et al. The pentagonal nature of self-assembled silicon chains and magic clusters on ag(110). *Nano Lett.*, v. 18, p. 2937, 2018.
- 2 CERDÁ, J. I. et al. Unveiling the pentagonal nature of perfectly aligned single-and double-strand si nano-ribbons on ag(110). *Nature Communications*, v. 7, p. 13076, 2016.
- 3 KITAEV, A. Y. Unpaired majorana fermions in quantum wires. *Physics-Uspekhi*, v. 44, n. 10S, p. 131, 2001. Disponível em: <http://stacks.iop.org/1063-7869/44/i=10S/a=S29>.
- 4 BATRA, N.; SHEET, G. Physics with coffee and doughnuts: Understanding the physics behind topological insulators through su-schrieffer-heeger model. *Resonance*, Springer, v. 25, p. 765–786, 2020.
- 5 PRZYSIKEZNA, A.; DUTTA, O.; ZAKRZEWSKI, J. Rice–mele model with topological solitons in an optical lattice. *New Journal of Physics*, IOP Publishing, v. 17, n. 1, p. 013018, 2015.
- 6 LIMA, A. et al. Thermoelectric properties of topological chains coupled to a quantum dot. *Scientific Reports*, Nature Publishing Group UK London, v. 13, n. 1, p. 1508, 2023.
- 7 OREG, Y.; REFAEL, G.; OPPEN, F. von. Helical liquids and majorana bound states in quantum wires. *Phys. Rev. Lett.*, American Physical Society, v. 105, p. 177002, Oct 2010. Disponível em: <https://link.aps.org/doi/10.1103/PhysRevLett.105.177002>.
- 8 LUTCHYN, R. M.; SAU, J. D.; SARMA, S. D. Majorana fermions and a topological phase transition in semiconductor-superconductor heterostructures. *Phys. Rev. Lett.*, American Physical Society, v. 105, p. 077001, Aug 2010. Disponível em: <https://link.aps.org/doi/10.1103/PhysRevLett.105.077001>.
- 9 MOURIK, V. et al. Signatures of majorana fermions in hybrid superconductor-semiconductor nanowire devices. *Science*, American Association for the Advancement of Science, v. 336, n. 6084, p. 1003–1007, 2012.
- 10 GÜL, Ö. et al. Ballistic majorana nanowire devices. *Nature Nanotechnology*, v. 13, n. 3, p. 192–197, Mar 2018. ISSN 1748-3395. Disponível em: <https://doi.org/10.1038/s41565-017-0032-8>.
- 11 AGUADO, R. Majorana quasiparticles in condensed matter. *Riv Nuovo Cimento*, Società Italiana di Fisica, v. 40, n. 11, p. 523, 2017. Disponível em: <https://www.sif.it/riviste/sif/ncr/econtents/2017/040/11/article/0>.
- 12 KROGSTRUP, P. et al. Epitaxy of semiconductor–superconductor nanowires. *Nature Materials*, v. 14, n. 4, p. 400–406, Apr 2015. ISSN 1476-4660. Disponível em: <https://doi.org/10.1038/nmat4176>.

- 13 NADJ-PERGE, S. et al. Observation of majorana fermions in ferromagnetic atomic chains on a superconductor. *Science*, American Association for the Advancement of Science, v. 346, n. 6209, p. 602–607, 2014.
- 14 JEON, S. et al. Distinguishing a majorana zero mode using spin-resolved measurements. *Science*, American Association for the Advancement of Science, v. 358, n. 6364, p. 772–776, 2017. ISSN 0036-8075.
- 15 OREG, Y.; REFAEL, G.; OPPEN, F. von. Helical liquids and majorana bound states in quantum wires. *Phys. Rev. Lett.*, American Physical Society, v. 105, p. 177002, Oct 2010. Disponível em: [⟨https://link.aps.org/doi/10.1103/PhysRevLett.105.177002⟩](https://link.aps.org/doi/10.1103/PhysRevLett.105.177002).
- 16 BEENAKKER, C. Search for majorana fermions in superconductors. *Annual Review of Condensed Matter Physics*, v. 4, n. 1, p. 113–136, 2013.
- 17 RIBEIRO, R. C. B. et al. Spin-polarized majorana zero modes in double zigzag honeycomb nanoribbons. *Phys. Rev. B*, American Physical Society, v. 105, p. 205115, May 2022. Disponível em: [⟨https://link.aps.org/doi/10.1103/PhysRevB.105.205115⟩](https://link.aps.org/doi/10.1103/PhysRevB.105.205115).
- 18 VOGT, P. et al. Silicene: Compelling experimental evidence for graphene like two-dimensional silicon. *Physical Review Letters*, APS, v. 108, p. 155501, 2012.
- 19 FLEURENCE, A. et al. Experimental Evidence for Epitaxial Silicene on Diboride Thin Films. *Physical Review Letters*, v. 108, n. 24, p. 245501, jun. 2012. ISSN 0031-9007, 1079-7114. Disponível em: [⟨https://link.aps.org/doi/10.1103/PhysRevLett.108.245501⟩](https://link.aps.org/doi/10.1103/PhysRevLett.108.245501).
- 20 FENG, B. et al. Evidence of silicene in honeycomb structures of silicon on ag(111). *Nano Letters*, v. 12, n. 7, p. 3507–3511, 2012. PMID: 22658061. Disponível em: [⟨https://doi.org/10.1021/nl301047g⟩](https://doi.org/10.1021/nl301047g).
- 21 RANČIĆ, M. J. Exactly solving the kitaev chain and generating majorana-zero-modes out of noisy qubits. *Scientific Reports*, v. 12, p. 19882, 2022.
- 22 FLENSBERG, K.; OPPEN, F. von; STERN, A. Engineered platforms for topological superconductivity and majorana zero modes. *Nature Reviews Materials*, Jul 2021. ISSN 2058-8437. Disponível em: [⟨https://doi.org/10.1038/s41578-021-00336-6⟩](https://doi.org/10.1038/s41578-021-00336-6).
- 23 LEANDRI, C. et al. Self-aligned silicon quantum wires on ag (1 1 0). *Surface science*, Elsevier, v. 574, n. 1, p. L9–L15, 2005.
- 24 FROLOV, S. M. et al. Quantum computing based on semiconductor nanowires. *MRS Bulletin*, v. 38, p. 809, 2013.
- 25 RICE, M.; MELE, E. Elementary excitations of a linearly conjugated diatomic polymer. *Physical Review Letters*, APS, v. 49, n. 19, p. 1455, 1982.
- 26 KAR, S. Edge state behavior in a su-schrieffer-heeger like model with periodically modulated hopping. *arXiv preprint arXiv:2307.06829*, 2023.
- 27 YU, X.-L. et al. Topological phase transitions, majorana modes, and quantum simulation of the su–schrieffer–heeger model with nearest-neighbor interactions. *Physical Review B*, APS, v. 101, n. 4, p. 045422, 2020.

- 28 READ, N.; GREEN, D. Paired states of fermions in two dimensions with breaking of parity and time-reversal symmetries and the fractional quantum hall effect. *Phys. Rev. B*, American Physical Society, v. 61, p. 10267–10297, Apr 2000. Disponível em: [⟨https://link.aps.org/doi/10.1103/PhysRevB.61.10267⟩](https://link.aps.org/doi/10.1103/PhysRevB.61.10267).
- 29 LEIJNSE, M.; FLENSBERG, K. Introduction to topological superconductivity and majorana fermions. *Semiconductor Science and Technology*, IOP Publishing, v. 27, n. 12, p. 124003, 2012.
- 30 SARMA, S. D.; NAYAK, C.; TEWARI, S. Proposal to stabilize and detect half-quantum vortices in strontium ruthenate thin films: Non-abelian braiding statistics of vortices in a $p_x + i p_y$ superconductor. *Physical Review B*, APS, v. 73, n. 22, p. 220502, 2006.
- 31 NADJ-PERGE, S. et al. Observation of majorana fermions in ferromagnetic atomic chains on a superconductor. *Science*, American Association for the Advancement of Science, v. 346, n. 6209, p. 602–607, 2014.
- 32 SILVA, J. F.; SILVA, L. G. V. da; VERNEK, E. Robustness of the kondo effect in a quantum dot coupled to majorana zero modes. *Phys. Rev. B*, American Physical Society, v. 101, p. 075428, Feb 2020. Disponível em: [⟨https://link.aps.org/doi/10.1103/PhysRevB.101.075428⟩](https://link.aps.org/doi/10.1103/PhysRevB.101.075428).
- 33 DENG, M.-T. et al. Nonlocality of majorana modes in hybrid nanowires. *Phys. Rev. B*, American Physical Society, v. 98, p. 085125, Aug 2018. Disponível em: [⟨https://link.aps.org/doi/10.1103/PhysRevB.98.085125⟩](https://link.aps.org/doi/10.1103/PhysRevB.98.085125).
- 34 SCHURAY, A.; RAMMLER, M.; RECHER, P. Signatures of the majorana spin in electrical transport through a majorana nanowire. *Phys. Rev. B*, American Physical Society, v. 102, p. 045303, Jul 2020. Disponível em: [⟨https://link.aps.org/doi/10.1103/PhysRevB.102.045303⟩](https://link.aps.org/doi/10.1103/PhysRevB.102.045303).
- 35 CLARKE, D. J. Experimentally accessible topological quality factor for wires with zero energy modes. *Phys. Rev. B*, American Physical Society, v. 96, p. 201109(R), Nov 2017. Disponível em: [⟨https://link.aps.org/doi/10.1103/PhysRevB.96.201109⟩](https://link.aps.org/doi/10.1103/PhysRevB.96.201109).
- 36 SCHURAY, A.; WEITHOFER, L.; RECHER, P. Fano resonances in majorana bound states–quantum dot hybrid systems. *Phys. Rev. B*, American Physical Society, v. 96, p. 085417, Aug 2017. Disponível em: [⟨https://link.aps.org/doi/10.1103/PhysRevB.96.085417⟩](https://link.aps.org/doi/10.1103/PhysRevB.96.085417).
- 37 PRADA, E.; AGUADO, R.; SAN-JOSE, P. Measuring majorana nonlocality and spin structure with a quantum dot. *Phys. Rev. B*, American Physical Society, v. 96, p. 085418, Aug 2017. Disponível em: [⟨https://link.aps.org/doi/10.1103/PhysRevB.96.085418⟩](https://link.aps.org/doi/10.1103/PhysRevB.96.085418).
- 38 RICCO, L. S. et al. Spin-dependent zero-bias peak in a hybrid nanowire-quantum dot system: Distinguishing isolated majorana fermions from andreev bound states. *Phys. Rev. B*, American Physical Society, v. 99, p. 155159, Apr 2019. Disponível em: [⟨https://link.aps.org/doi/10.1103/PhysRevB.99.155159⟩](https://link.aps.org/doi/10.1103/PhysRevB.99.155159).
- 39 DENG, M. T. et al. Majorana bound state in a coupled quantum-dot hybrid-nanowire system. *Science*, American Association for the Advancement of Science, v. 354, n. 6319, p. 1557–1562, 2016.
- 40 BERTHOLD, J.; YONGLONG, X.; YAZDANI, A. Detecting and distinguishing majorana zero modes with the scanning tunnelling microscope. *Nat Rev Phys*, Nature Group, 2021. Disponível em: [⟨https://doi.org/10.1038/s42254-021-00328-z⟩](https://doi.org/10.1038/s42254-021-00328-z).

- 41 ZHANG, H. et al. Next steps of quantum transport in majorana nanowire devices. *Nat Commun*, v. 10, p. 5128, Nov 2019. Disponível em: [〈https://doi.org/10.1038/s41467-019-13133-1〉](https://doi.org/10.1038/s41467-019-13133-1).
- 42 PRADA, E. et al. From andreev to majorana bound states in hybrid superconductor-semiconductor nanowires. *Nat Rev Phys*, v. 2, p. 575–594, 2020. Disponível em: [〈https://doi.org/10.1038/s42254-020-0228-y〉](https://doi.org/10.1038/s42254-020-0228-y).
- 43 YU, P. et al. Non-Majorana states yield nearly quantized conductance in superconductor-semiconductor nanowire devices. *Nat. Phys.*, Springer Nature, v. 17, p. 482–488, 2021. Disponível em: [〈https://doi.org/10.1038/s41567-020-01107-w〉](https://doi.org/10.1038/s41567-020-01107-w).
- 44 YU, P. et al. *Delocalized states in three-terminal superconductor-semiconductor nanowire devices*. 2021.
- 45 PENDHARKAR, M. et al. Parity-preserving and magnetic field-resilient superconductivity in insb nanowires with sn shells. *Science*, v. 372, n. 6541, p. 508–511, 2021. Disponível em: [〈https://www.science.org/doi/abs/10.1126/science.aba5211〉](https://www.science.org/doi/abs/10.1126/science.aba5211).
- 46 PAN, H.; SARMA, S. D. Physical mechanisms for zero-bias conductance peaks in majorana nanowires. *Phys. Rev. Research*, American Physical Society, v. 2, p. 013377, Mar 2020. Disponível em: [〈https://link.aps.org/doi/10.1103/PhysRevResearch.2.013377〉](https://link.aps.org/doi/10.1103/PhysRevResearch.2.013377).
- 47 PAN, H. et al. Generic quantized zero-bias conductance peaks in superconductor-semiconductor hybrid structures. *Phys. Rev. B*, American Physical Society, v. 101, p. 024506, Jan 2020. Disponível em: [〈https://link.aps.org/doi/10.1103/PhysRevB.101.024506〉](https://link.aps.org/doi/10.1103/PhysRevB.101.024506).
- 48 PAN, H. et al. Quantized and unquantized zero-bias tunneling conductance peaks in majorana nanowires: Conductance below and above $2e^2/h$. *Phys. Rev. B*, American Physical Society, v. 103, p. 214502, Jun 2021. Disponível em: [〈https://link.aps.org/doi/10.1103/PhysRevB.103.214502〉](https://link.aps.org/doi/10.1103/PhysRevB.103.214502).
- 49 KLINOVAJA, J.; FERREIRA, G. J.; LOSS, D. Helical states in curved bilayer graphene. *Phys. Rev. B*, American Physical Society, v. 86, p. 235416, Dec 2012. Disponível em: [〈https://link.aps.org/doi/10.1103/PhysRevB.86.235416〉](https://link.aps.org/doi/10.1103/PhysRevB.86.235416).
- 50 KLINOVAJA, J.; LOSS, D. Giant spin-orbit interaction due to rotating magnetic fields in graphene nanoribbons. *Phys. Rev. X*, American Physical Society, v. 3, p. 011008, Jan 2013. Disponível em: [〈https://link.aps.org/doi/10.1103/PhysRevX.3.011008〉](https://link.aps.org/doi/10.1103/PhysRevX.3.011008).
- 51 ZHAOA, A.; WANG, B. Two-dimensional graphene-like xenes as potential topological materials. *APL Materials*, AIP Publishing, v. 8, p. 030701, 2020. Disponível em: [〈https://doi.org/10.1063/1.51359846〉](https://doi.org/10.1063/1.51359846).
- 52 DUTREIX, C. et al. Majorana fermions in honeycomb lattices. *The European Physical Journal B*, v. 87, n. 12, p. 296, Dec 2014. ISSN 1434-6036. Disponível em: [〈https://doi.org/10.1140/epjb/e2014-50243-9〉](https://doi.org/10.1140/epjb/e2014-50243-9).
- 53 MA, T. et al. Triplet p-wave pairing correlation in low-doped zigzag graphene nanoribbons. *Scientific Reports*, The Author(s) SN -, v. 7, p. 42262 EP –, Feb 2017. Article. Disponível em: [〈https://doi.org/10.1038/srep42262〉](https://doi.org/10.1038/srep42262).

- 54 KOPCIUSZYŃSKI, M. et al. Pb nanoribbons on the si (553) surface. *Physical Review B*, APS, v. 88, n. 15, p. 155431, 2013.
- 55 KOPCIUSZYŃSKI, M. et al. Purely one-dimensional bands with a giant spin-orbit splitting: Pb nanoribbons on si(553) surface. *Scientific Reports*, v. 7, n. 1, p. 46215, Apr 2017. ISSN 2045-2322. Disponível em: [⟨https://doi.org/10.1038/srep46215⟩](https://doi.org/10.1038/srep46215).
- 56 BRAND, C. et al. Spin-resolved band structure of a densely packed pb monolayer on si(111). *Phys. Rev. B*, American Physical Society, v. 96, p. 035432, Jul 2017. Disponível em: [⟨https://link.aps.org/doi/10.1103/PhysRevB.96.035432⟩](https://link.aps.org/doi/10.1103/PhysRevB.96.035432).
- 57 LALMI, B. et al. Epitaxial growth of a silicene sheet. *Applied Physics Letters*, v. 97, n. 22, p. 223109, 2010.
- 58 AUFRAY, B. et al. Graphene-like silicon nanoribbons on ag(110): A possible formation of silicene. *Applied Physics Letters*, v. 96, n. 18, p. 183102, 2010.
- 59 LIU, C.-C.; JIANG, H.; YAO, Y. Low-energy effective hamiltonian involving spin-orbit coupling in silicene and two-dimensional germanium and tin. *Phys. Rev. B*, American Physical Society, v. 84, p. 195430, Nov 2011. Disponível em: [⟨https://link.aps.org/doi/10.1103/PhysRevB.84.195430⟩](https://link.aps.org/doi/10.1103/PhysRevB.84.195430).
- 60 EZAWA, M. Valley-polarized metals and quantum anomalous hall effect in silicene. *Phys. Rev. Lett.*, American Physical Society, v. 109, p. 055502, Aug 2012. Disponível em: [⟨https://link.aps.org/doi/10.1103/PhysRevLett.109.055502⟩](https://link.aps.org/doi/10.1103/PhysRevLett.109.055502).
- 61 DRUMMOND, N. D.; ZÓLYOMI, V.; FAL'KO, V. I. Electrically tunable band gap in silicene. *Phys. Rev. B*, American Physical Society, v. 85, p. 075423, Feb 2012. Disponível em: [⟨https://link.aps.org/doi/10.1103/PhysRevB.85.075423⟩](https://link.aps.org/doi/10.1103/PhysRevB.85.075423).
- 62 JIAO, Z.; YAO, Q.; ZANDVLIET, H. Tailoring and probing the quantum states of matter of 2d dirac materials with a buckled honeycomb structure. *Physica E: Low-dimensional Systems and Nanostructures*, v. 121, p. 114113, 2020. Disponível em: [⟨https://doi.org/10.1016/j.physe.2020.114113⟩](https://doi.org/10.1016/j.physe.2020.114113).
- 63 TSAI, W.-F. et al. Gated silicene as a tunable source of nearly 100% spin-polarized electrons. *Nature Communications*, v. 4, n. 1, p. 1500, Feb 2013. ISSN 2041-1723. Disponível em: [⟨https://doi.org/10.1038/ncomms2525⟩](https://doi.org/10.1038/ncomms2525).
- 64 CHICO, L.; LATGÉ, A.; BREY, L. Symmetries of quantum transport with rashba spin-orbit: graphene spintronics. *Phys. Chem. Chem. Phys.*, The Royal Society of Chemistry, v. 17, p. 16469–16475, 2015. Disponível em: [⟨http://dx.doi.org/10.1039/C5CP01637A⟩](http://dx.doi.org/10.1039/C5CP01637A).
- 65 JIANG, P. et al. Robust generation of half-metallic transport and pure spin current with photogalvanic effect in zigzag silicene nanoribbons. *Journal of Physics: Condensed Matter*, IOP Publishing, v. 31, n. 49, p. 495701, sep 2019. Disponível em: [⟨https://doi.org/10.1088/1361-648x/ab3dd6⟩](https://doi.org/10.1088/1361-648x/ab3dd6).
- 66 WANG, T.-C. et al. Tunable magnetic states on the zigzag edges of hydrogenated and halogenated group-iv nanoribbons. *Sci. Rep.*, v. 6, p. 39083, 2016. Disponível em: [⟨https://doi.org/10.1038/srep39083⟩](https://doi.org/10.1038/srep39083).

- 67 FU, L.; KANE, C. L. Superconducting proximity effect and majorana fermions at the surface of a topological insulator. *Phys. Rev. Lett.*, American Physical Society, v. 100, p. 096407, Mar 2008. Disponível em: <https://link.aps.org/doi/10.1103/PhysRevLett.100.096407>.
- 68 NAGAI, Y.; NAKAMURA, H.; MACHIDA, M. Spin-polarized majorana bound states inside a vortex core in topological superconductors. *Journal of the Physical Society of Japan*, v. 83, n. 6, p. 064703, 2014. Disponível em: <https://doi.org/10.7566/JPSJ.83.064703>.
- 69 XU, J.-P. et al. Experimental detection of a majorana mode in the core of a magnetic vortex inside a topological insulator-superconductor $\text{Bi}_2\text{Te}_3/\text{NbSe}_2$ heterostructure. *Phys. Rev. Lett.*, American Physical Society, v. 114, p. 017001, Jan 2015. Disponível em: <https://link.aps.org/doi/10.1103/PhysRevLett.114.017001>.
- 70 SMITH, E. D. B.; TANAKA, K.; NAGAI, Y. Manifestation of chirality in the vortex lattice in a two-dimensional topological superconductor. *Phys. Rev. B*, American Physical Society, v. 94, p. 064515, Aug 2016. Disponível em: <https://link.aps.org/doi/10.1103/PhysRevB.94.064515>.
- 71 TANAKA, K. K.; ICHIOKA, M.; ONARI, S. Spin-polarized local density of states in the vortex state of helical p -wave superconductors. *Phys. Rev. B*, American Physical Society, v. 95, p. 134502, Apr 2017. Disponível em: <https://link.aps.org/doi/10.1103/PhysRevB.95.134502>.
- 72 LEIJNSE, M.; FLENSBERG, K. Quantum information transfer between topological and spin qubit systems. *Phys. Rev. Lett.*, American Physical Society, v. 107, p. 210502, Nov 2011. Disponível em: <https://link.aps.org/doi/10.1103/PhysRevLett.107.210502>.
- 73 LEIJNSE, M.; FLENSBERG, K. Hybrid topological-spin qubit systems for two-qubit-spin gates. *Phys. Rev. B*, American Physical Society, v. 86, p. 104511, Sep 2012. Disponível em: <https://link.aps.org/doi/10.1103/PhysRevB.86.104511>.
- 74 HOFFMAN, S. et al. Universal quantum computation with hybrid spin-majorana qubits. *Phys. Rev. B*, American Physical Society, v. 94, p. 045316, Jul 2016. Disponível em: <https://link.aps.org/doi/10.1103/PhysRevB.94.045316>.
- 75 ZHOU, B.-Z.; XU, D.-H.; ZHOU, B. Majorana zero modes in a ladder of density-modulated kitaev superconductor chains. *Physics Letters A*, v. 381, n. 30, p. 2426 – 2431, 2017. ISSN 0375-9601. Disponível em: <http://www.sciencedirect.com/science/article/pii/S0375960117304887>.
- 76 MAIELLARO, A.; ROMEO, F.; CITRO, R. Topological phase diagram of a kitaev ladder. *The European Physical Journal Special Topics*, v. 227, n. 12, p. 1397–1404, Dec 2018. ISSN 1951-6401. Disponível em: <https://doi.org/10.1140/epjst/e2018-800090-y>.
- 77 CHIU, C.-K. et al. Classification of topological quantum matter with symmetries. *Rev. Mod. Phys.*, American Physical Society, v. 88, p. 035005, Aug 2016. Disponível em: <https://link.aps.org/doi/10.1103/RevModPhys.88.035005>.
- 78 WAKATSUKI, R.; EZAWA, M.; NAGAOSA, N. Majorana fermions and multiple topological phase transition in kitaev ladder topological superconductors. *Physical Review B*, APS, v. 89, n. 17, p. 174514, 2014.

- 79 BERNEVIG, B. A.; HUGHES, T. L. *Topological Insulators and Topological Superconductors*. STU - Student edition. Princeton University Press, 2013. ISBN 9780691151755. Disponível em: <http://www.jstor.org/stable/j.ctt19cc2gc>).
- 80 ALASE, A. *Boundary Physics and Bulk-Boundary Correspondence in Topological Phases of Matter*. 1. ed. Springer Nature Switzerland AG: Springer Theses, 2019.
- 81 MIN, H. et al. Intrinsic and rashba spin-orbit interactions in graphene sheets. *Phys. Rev. B*, American Physical Society, v. 74, p. 165310, Oct 2006. Disponível em: <https://link.aps.org/doi/10.1103/PhysRevB.74.165310>).
- 82 ZAREA, M.; SANDLER, N. Rashba spin-orbit interaction in graphene and zigzag nanoribbons. *Phys. Rev. B*, American Physical Society, v. 79, p. 165442, Apr 2009. Disponível em: <https://link.aps.org/doi/10.1103/PhysRevB.79.165442>).
- 83 DINIZ, G. S.; GUASSI, M. R.; QU, F. Controllable spin-charge transport in strained graphene nanoribbon devices. *Journal of Applied Physics*, v. 116, n. 11, p. 113705, 2014. Disponível em: <http://dx.doi.org/10.1063/1.4896251>).
- 84 TSE, W.-K. et al. Quantum anomalous hall effect in single-layer and bilayer graphene. *Phys. Rev. B*, American Physical Society, v. 83, p. 155447, Apr 2011. Disponível em: <https://link.aps.org/doi/10.1103/PhysRevB.83.155447>).
- 85 JEON, S. et al. Distinguishing a majorana zero mode using spin-resolved measurements. *Science*, American Association for the Advancement of Science, v. 358, n. 6364, p. 772–776, 2017. ISSN 0036-8075. Disponível em: <https://science.sciencemag.org/content/358/6364/772>).
- 86 KHOEINI, F.; SHAKOURI, K.; PEETERS, F. M. Peculiar half-metallic state in zigzag nanoribbons of mos₂: Spin filtering. *Phys. Rev. B*, American Physical Society, v. 94, p. 125412, Sep 2016. Disponível em: <https://link.aps.org/doi/10.1103/PhysRevB.94.125412>).
- 87 XU, R. et al. Half-metallicity in co-doped wse₂ nanoribbons. *ACS Applied Materials & Interfaces*, American Chemical Society, v. 9, n. 44, p. 38796–38801, Nov 2017. ISSN 1944-8244. Disponível em: <https://doi.org/10.1021/acsami.7b12196>).
- 88 PODSIADŁY-PASZKOWSKA, A.; KRAWIEC, M. Dirac fermions in silicene on pb(111) surface. *Phys. Chem. Chem. Phys.*, The Royal Society of Chemistry, v. 17, p. 2246–2251, 2015. Disponível em: <http://dx.doi.org/10.1039/C4CP05104A>).
- 89 STEPNIAK-DYBALA JALOCZOWSKI, M.; KRAWIEC, M. Silicene nanoribbons on pb-reconstructed si(111) surface. *Condens. Matter*, v. 1, n. 1, 2016. Disponível em: <https://www.mdpi.com/2410-3896/1/1/8#cite>).
- 90 STEPNIAK-DYBALA, A.; KRAWIEC, M. Formation of silicene on ultrathin pb(111) films. *The Journal of Physical Chemistry C*, American Chemical Society, v. 123, n. 27, p. 17019–17025, Jul 2019. ISSN 1932-7447. Disponível em: <https://doi.org/10.1021/acs.jpcc.9b04343>).
- 91 OWCZAREK, S.; MARKOWSKI, L. The role of surfactant in two-components structures formation on si(111) surface. *Surface Science*, v. 693, p. 121552, 2020. ISSN 0039-6028. Disponível em: <https://www.sciencedirect.com/science/article/pii/S0039602819306909>).

- 92 STEPNIAK-DYBALA A.; KRAWIEC, M. Structural model of silicene-like nanoribbons on a pb-reconstructed si(111) surface. *Beilstein J. Nanotechnol.*, v. 8, p. 1836, 2017.
- 93 Suggestion of Prof. Mariuz Krawiec in a private correspondence.
- 94 NAKADA, K. et al. Edge state in graphene ribbons: Nanometer size effect and edge shape dependence. *Phys. Rev. B*, American Physical Society, v. 54, p. 17954–17961, Dec 1996. Disponível em: <https://link.aps.org/doi/10.1103/PhysRevB.54.17954>.
- 95 WAKABAYASHI, K. et al. Electronic states of graphene nanoribbons and analytical solutions. *Science and Technology of Advanced Materials*, Taylor and Francis, v. 11, n. 5, p. 054504, 2010. Disponível em: <http://dx.doi.org/10.1088/1468-6996/11/5/054504>.
- 96 FU, B.; ABID, M.; LIU, C.-C. Systematic study on stanene bulk states and the edge states of its zigzag nanoribbon. *New Journal of Physics*, IOP Publishing, v. 19, n. 10, p. 103040, nov 2017. Disponível em: <https://doi.org/10.1088/1367-2630/aa8c46>.
- 97 CORREA, J. H.; PEZO, A.; FIGUEIRA, M. S. Braiding of edge states in narrow zigzag graphene nanoribbons: Effects of third-neighbor hopping on transport and magnetic properties. *Phys. Rev. B*, American Physical Society, v. 98, p. 045419, Jul 2018. Disponível em: <https://link.aps.org/doi/10.1103/PhysRevB.98.045419>.
- 98 ZHU, X.; GUO, H.; FENG, S. Quantum magnetism of topologically-designed graphene nanoribbons. *Journal of Physics: Condensed Matter*, IOP Publishing, v. 31, n. 50, p. 505601, sep 2019. Disponível em: <https://doi.org/10.1088/1361-648x/ab3f81>.
- 99 XU, C. et al. Giant magnetoresistance in silicene nanoribbons. *Nanoscale*, The Royal Society of Chemistry, v. 4, p. 3111–3117, 2012. Disponível em: <http://dx.doi.org/10.1039/C2NR00037G>.
- 100 Lü, X. L.; XIE, Y.; XIE, H. Topological and magnetic phase transition in silicene-like zigzag nanoribbons. *New Journal of Physics*, IOP Publishing, v. 20, n. 4, p. 043054, apr 2018. Disponível em: <https://doi.org/10.1088/1367-2630/aabc6e>.
- 101 KARZIG, T. et al. Scalable designs for quasiparticle-poisoning-protected topological quantum computation with majorana zero modes. *Phys. Rev. B*, American Physical Society, v. 95, p. 235305, Jun 2017. Disponível em: <https://link.aps.org/doi/10.1103/PhysRevB.95.235305>.
- 102 NAYAK, C. et al. Non-abelian anyons and topological quantum computation. *Rev. Mod. Phys.*, American Physical Society, v. 80, p. 1083–1159, Sep 2008. Disponível em: <https://link.aps.org/doi/10.1103/RevModPhys.80.1083>.
- 103 STEINER, J. F.; OPPEN, F. von. Readout of majorana qubits. *Phys. Rev. Research*, American Physical Society, v. 2, p. 033255, Aug 2020. Disponível em: <https://link.aps.org/doi/10.1103/PhysRevResearch.2.033255>.
- 104 AASEN, D. et al. Milestones toward majorana-based quantum computing. *Phys. Rev. X*, American Physical Society, v. 6, p. 031016, Aug 2016. Disponível em: <https://link.aps.org/doi/10.1103/PhysRevX.6.031016>.
- 105 DÁVILA, M.; LAY, G. L. Silicene: Genesis, remarkable discoveries, and legacy. *Materials Today Advances*, v. 16, p. 100312, 2022.

- 106 TAO, L. et al. Silicene field-effect transistors operating at room temperature. *Nature Nanotechnology*, v. 10, p. 227–231, 2015.
- 107 LAY, G. L. Silicene transistors. *Nature Nanotechnology*, v. 10, p. 202, 2015.
- 108 DAS, A. et al. Zero-bias peaks and splitting in an al-inas nanowire topological superconductor as a signature of majorana fermions. *Nature Physics*, Nature Publishing Group SN -, v. 8, p. 887 EP –, Nov 2012. Article. Disponível em: <http://dx.doi.org/10.1038/nphys2479>.
- 109 LUTCHYN, R. M. et al. Majorana zero modes in superconductor–semiconductor heterostructures. *Nature Reviews Materials*, Nature Group, v. 3, p. 52–68, May 2018. Disponível em: <https://doi.org/10.1038/s41578-018-0003-1>.
- 110 KIM, H. et al. Toward tailoring majorana bound states in artificially constructed magnetic atom chains on elemental superconductors. *Science Advances*, v. 4, n. 5, p. eaar5251, 2018. Disponível em: <https://www.science.org/doi/abs/10.1126/sciadv.aar5251>.
- 111 JÄCK, B.; XIE, Y.; YAZDANI, A. B. and xie, y. and yazdani. *Nature Reviews Physics*, v. 3, p. 541, 2021.
- 112 GRAZIANETTI, C.; MARTELLA, C. The rise of the xenes: From the synthesis to the integration processes for electronics and photonics. *Materials (Basel)*, Switzerland, v. 14, n. 15, jul. 2021.
- 113 YUE, S. et al. S. yue and h. zhou and y. feng and y. wang and z. *Nano Lett.*, v. 22, p. 695, 2022.
- 114 PADOVA, P. D. et al. Evidence of graphene-like electronic signature in silicene nanoribbons. *Applied Physics Letters*, v. 96, n. 26, jun. 2010. ISSN 0003-6951. Disponível em: <https://doi.org/10.1063/1.3459143>.
- 115 PADOVA, P. D. et al. 1d graphene-like silicon systems: silicene nano-ribbons. *Journal of Physics: Condensed Matter*, IOP Publishing, v. 24, n. 22, p. 223001, may 2012.
- 116 PAWLAK, R. et al. Quantitative determination of atomic buckling of silicene by atomic force microscopy. *Proceedings of the National Academy of Sciences*, National Acad Sciences, v. 117, n. 1, p. 228–237, 2020.
- 117 TSUD, N. et al. Interfacial reconstruction in the system pb/ag(110). *Surface Science*, v. 542, n. 1, p. 112–119, 2003. ISSN 0039-6028. Disponível em: <https://www.sciencedirect.com/science/article/pii/S0039602803009774>.
- 118 JÄCK, B.; XIE, Y.; YAZDANI, A. Detecting and distinguishing majorana zero modes with the scanning tunnelling microscope. *Nature Reviews Physics*, v. 3, n. 8, p. 541–554, Aug 2021. ISSN 2522-5820. Disponível em: <https://doi.org/10.1038/s42254-021-00328-z>.
- 119 STANESCU, T. D. *Introduction to Topological Quantum Matter & Quantum Computation*. 1st edition. ed. [S.l.]: CRC Press, 2016. ISBN 1482245930.
- 120 ZAK, J. Berry's phase for energy bands in solids. *Phys. Rev. Lett.*, American Physical Society, v. 62, p. 2747–2750, Jun 1989. Disponível em: <https://link.aps.org/doi/10.1103/PhysRevLett.62.2747>.

- 121 ZHANG, Q. et al. Large spin-valley polarization in monolayer MoS_2 on top of $\text{Cu}(111)$. *Advanced Materials*, Wiley Online Library, v. 28, n. 5, p. 959–966, 2016.
- 122 HUERTAS-HERNANDO, D.; GUINEA, F.; BRATAAS, A. Spin-orbit coupling in curved graphene, fullerenes, nanotubes, and nanotube caps. *Physical Review B*, APS, v. 74, n. 15, p. 155426, 2006.
- 123 LEE, K.; YUN, W. S.; LEE, J. Giant rashba-type splitting in molybdenum-driven bands of $\text{MoS}_2/\text{Bi}(111)$ heterostructure. *Physical Review B*, APS, v. 91, n. 12, p. 125420, 2015.
- 124 VERNEK, E. et al. Subtle leakage of a majorana mode into a quantum dot. *Phys. Rev. B*, American Physical Society, v. 89, p. 165314, Apr 2014. Disponível em: <https://link.aps.org/doi/10.1103/PhysRevB.89.165314>.
- 125 LIU, X. et al. Majorana spintronics. *Phys. Rev. B*, American Physical Society, v. 94, p. 014511, Jul 2016. Disponível em: <https://link.aps.org/doi/10.1103/PhysRevB.94.014511>.
- 126 RIBEIRO, R. B. et al. Spin-polarized majorana zero modes in proximitized superconducting penta-silicene nanoribbons. *Scientific Reports*, Nature Publishing Group UK London, v. 13, n. 1, p. 17965, 2023.